Inkjet Etching of Micro-Via Holes in Thin Polymer Layers

By Yan Zhang

A Doctoral Thesis
Submitted in Partial Fulfilment of the Requirements
for the Award of Doctor of Philosophy
of
Loughborough University

ABSTRACT

Facilitated by the development of various direct-write techniques and functional polymeric materials including polymer based conductors and semiconductors, printed electronics are flourishing both commercially and as a research topic. This is not only because of their simpler manufacturing routes and lower cost, but also as a result of lower processing temperatures and better compatibility with flexible substrates, compared with conventional electronics. The development of conventional electronics has been guided by Moore's Law, the driver for which lies in the demand for electronic devices with better performance and portability at lower prices. Therefore, one can expect a similar trend for printed electronics to guide its development. Multi-layered printing can be adopted in printed electronics to achieve higher density integration, so that this development trend can be maintained. In such circumstances, creation of electrical connections between multiple layers emerges as an important issue for printed electronics. Inkjet-etched via holes are one potential solution to providing such electrical interconnections, and which can provide good integration with other inkjet-printed features simply by switching nozzles. This thesis aims to elicit a better understanding of the physics involved in inkjet etching and investigate the capability of the inkjet etching technique.

In the thesis, the factors that can affect the size of via holes produced by inkjet etching are evaluated, which is significant for evaluating the capability of this technique to deliver industrially relevant features. Identified factors include droplet ejection frequency, droplet diameter, solvent properties and substrate temperature. Droplet ejection frequency, *i.e.* the reciprocal of the time interval between drops, determines the extent of evaporation of the solvent between two consecutive drop impacts. Droplet diameter determines the radius of the wetted area after the droplet

impacts on the surface and spreads into a sessile drop. Solvents with different evaporation properties result in different size evolution with the number of drops dispensed, as does droplet ejection frequency. Higher substrate temperatures can reduce the drop diameter during flight and decrease the evaporation time on polymer surfaces, which can shrink the size of via holes.

Another important issue is achieving complete polymer penetration as residual polymer creates an electrical conduction barrier after such holes are subsequently filled with conductive materials or act as a barrier to filling by electroplating. Experiments have been carried out to test the effect of outer diameter and polymer thickness on polymer penetration. Electroplating is utilised to test the completeness of via hole penetration. A mechanism using the Marangoni effect to explain the protrusion drying pattern other than a hole in the polymer layer is proposed.

Key words: Inkjet etching; Polymer etching; Via holes; Printed electronics; Coffee ring effect; Polymer patterning

ACKNOWLEDGEMENTS

This work was funded by the EPSRC 3D Mintegration project and the Wolfson School of Mechanical and Manufacturing, Loughborough University. I would like to express my sincere gratitude to the funding bodies for their financial support in this work. I would like to give special thanks to my supervisors, Professor Changqing Liu and Mr. David C. Whalley, for their continuous help, patient guidance and the generosity of allowing freedom and flexibility throughout this work.

I would certainly like to thank the following people and bodies for their kind help and support during this work. I would like to express my appreciation of Dr John Chappell for his thorough inkjet printer training. I would like to thank Mr Andy Sandaver, Mr Jagpal Singh and Dr Keith Yendall for their characterisation method training and analysis help throughout this work. I would like to thank Dr George W Weaver and Dr Ben Buckley in the Department of Chemistry, Loughborough University for their support in helping me with finding solvents for dissolving polymers and providing various solvents for trying out. Special thanks are given to Dr Xiaoyun Cui and Dr Yi Qin for their generous and kind help with various problems during my work. Special thanks to Mr Daniel J. Beardsall for his work in proofreading.

The author would also like to thank the EPSRC Engineering Instrument Pool for their generous free loan of the high speed camera system.

Special thanks to all my friends who are there when I need them to be. Last but not least, I would like to give special thanks to my parents for their understanding of my degree pursuing and the compromises they have made.

Table of Contents

List of Figures

List of Tables

Glossary

AFM	Atomic force microscope
CAD	Computer aided design
CLA	Chromatic lateral aberration
CMOS	Complementary metal-oxide-semiconductor
CPU	Central processing unit
CSV	Comma separated values
CVD	Chemical vapour deposition
DoD	Drop-on-demand
DPN	Dip pen nanolithography
DW	Direct write
E-DPN	Electrochemical dip pen nanolithography
EFS	Electric field sensor
FIB	Focused ion beam
IC	Integrated circuit
IPA	Isopropyl alcohol
LCVD	Laser chemical vapour deposition
LDW	Laser direct writing
LIFT	Laser-induced forward transfer
MAPLE	Matrix-assisted pulsed laser evaporation
MCM	Multi-chip module

MEMS	Micro-electro-mechanical systems
MHA	16-mercaptohexadecanoic acid
NFP	Nanofountain probe
OLED	Organic light emitting diode
PCB	Printed circuit board
PEMA	Polyethylmethacrylate
PMMA	Polymethylmethacrylate
PPL	Polymer pen lithography
PR	Photoresist
PVP	Poly(4-vinyl phenol)
RFID	Radio frequency identification
ROI	Region of interest
SIP	System in package
SOC	System on chip
SOP	System-on-package
tDPN	Thermal dip pen nanolithography
TTM	Time to market
UV	Ultraviolet
WLI	White light interferometry

1 Introduction

The phenomenon of the coffee ring pattern remaining after evaporation of the liquid from a particle-laden solution on a surface was first investigated by Deegan, *et al.* [1,2,3]. The coffee ring effect refers to the fact that particles suspended in the solution are transferred outwards to the periphery of the sessile drop and accumulate at the border, resulting in a pattern with a ridge-like border and a valley in the centre. The coffee ring effect is believed to be caused by the capillary flow from the centre to the contact line resulting from liquid replenishment to the edge, due to the non-uniform solvent evaporation across the liquid surface and a pinned contact line.

Using inkjets as an etching tool for producing via holes was pioneered by Kawase, *et al.* [4,5,6] for manufacturing all-polymer thin film transistors. Before this the coffee ring effect had preferably been eliminated, due to the inhomogeneity in deposition thickness it caused. Kawase, *et al.* have successfully demonstrated all-polymer thin film transistor circuits, with via holes used for the vertical interconnection structures made by inkjet etching utilising the coffee ring effect. Their experiments showed that the diameter of the via hole produced using inkjet etching could be controlled by the droplet volume and was independent of the number of solvent drops. The flow velocity as a function of its distance from the contact line was also given quantitatively. Using a similar technique, de Gans, *et al.* [7,8] generated structures such as arrays of holes and grooves in polystyrene and polybenzylmethacrylate layers. Isopropyl acetate and *n*-butyl acetate were used as the etchants in their study. Both hole radius and groove width were found to be in a power law relationship with the number of drops. The generated structures can be manipulated by the distance between individual droplets. Grimaldi, *et al.* [9] studied the cavity depth and edge height as functions of the number of drops dispensed in

polystyrene layers and the data obtained indicated a linear relationship. Li, *et al.* [10] studied the influence of molar mass of polyethylmethacrylate (PEMA) and polystyrene on the generated structures with various drop numbers, providing the hole profiles with drop numbers for different molar masses. The relationship between hole depth, hole radius and molar mass was schematically demonstrated for PEMA. Bonaccurso, *et al.* [11] and Pericet-Camara, *et al.* [12] used inkjet techniques to fabricate microvessels and microlenses. Xia, *et al.* [13,14] and Lu, *et al.* [15] demonstrated using inkjet techniques to create cavities for display applications.

Lennon, *et al.* [16] also used inkjet printing as the etching method to create openings in inorganic SiO_2 layers for solar cell applications. The typical hole diameter achieved in 300nm SiO_2 layers ranged from 40µm to 50µm. A process of using a single resist layer for multiple patterning steps was also reported [17]. Both applications used dissolution of a polymer layer to form an intermediate patterning mask rather than the final product. Yang, *et al.* [18,19] used inkjet printing to dispense a silver-based ink onto a polymethylmethacrylate (PMMA) surface so that silver particles were embedded into the dielectric layer as a result of polymer swelling and dissolution to create an electrically conductive path between layers.

Even though it has been ten years since inkjet etching was first used to dissolve via holes for application in electronics, this technique is still underdeveloped and more investigations are needed for its evaluation before it can ultimately find suitable applications in mass production. This work aims to evaluate the inkjet-etching technique for via hole fabrication in organic dielectric materials.

1.1 Structure of the Thesis

In this thesis, Chapter 1 provides a brief introduction to the context of the inkjet-etching process, a review of the work that has been done by other researchers, and an overview of the thesis structure. Chapter 2 discusses printed electronics in comparison with traditional Si-based electronics fabrication. The context of this via hole study, *i.e.* how Moore's Law guides the miniaturisation of electronics, is included. The most widely used via hole drilling techniques, mechanical drilling and laser ablation, are also introduced. Chapter 3 comprehensively reviews existing direct-write techniques

that can be used in printed electronics, including inkjet printing. The initial experimental setup, and the preparation and the characterisation methods used in this work, are covered in chapter 4. Chapter 5 presents the results obtained to understand the factors that can influence the size of the via holes produced by inkjet etching. Chapter 6 presents results from penetration of inkjet-etched via holes tests, using samples with pre-deposited seed layers followed by electroplating, and the factors that affect penetration are discussed based on these experiments. Chapter 7 discusses the effect of thermal Marangoni flows on the pattern formation. Chapter 8 summarises by presenting the main findings and the recommendations for future work. Figure 1-1 schematically illustrates the structure of this thesis.

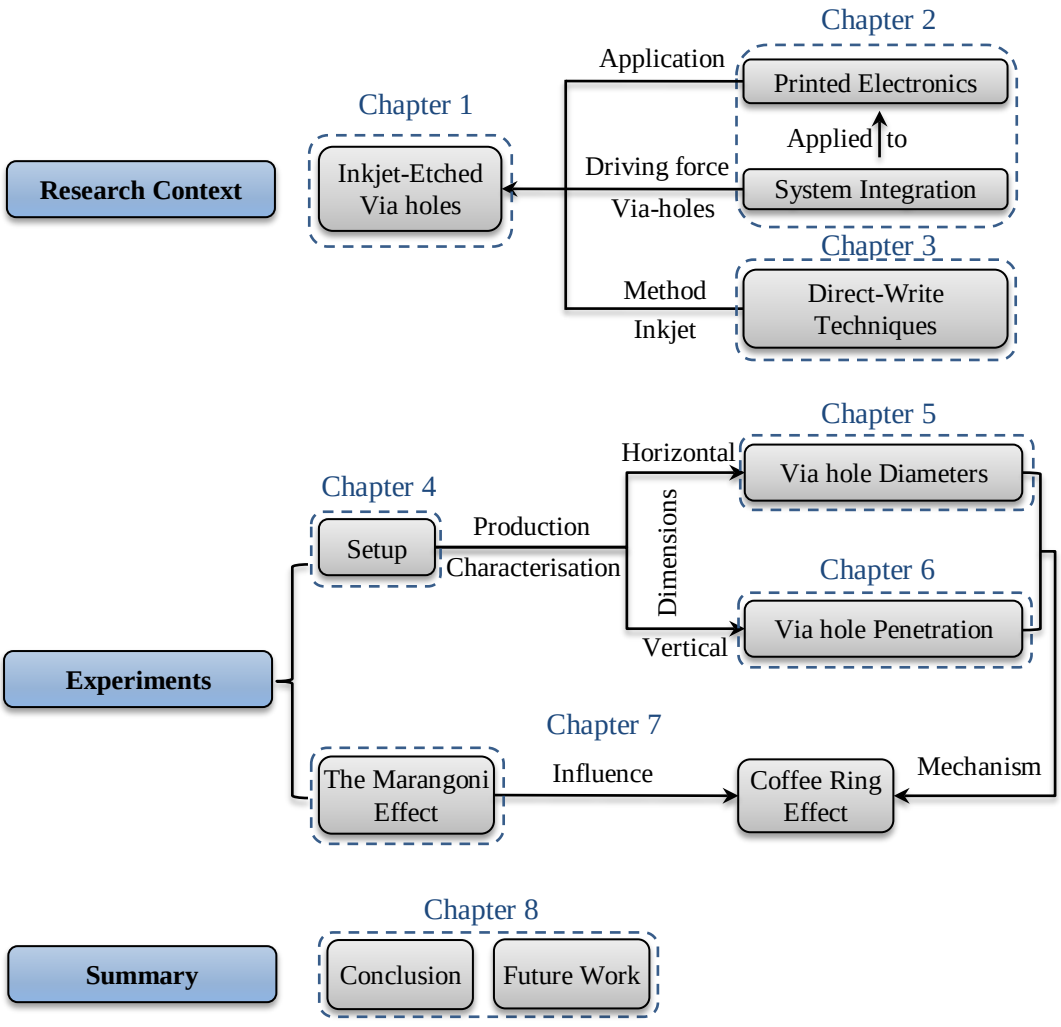

Figure 1-1 Structure of the thesis

1.2 Publications Arising from the Thesis Work

Three journal papers have been published based on the work in this thesis. The effect of droplet ejection frequency on the size development of inkjet etched via holes with the number of solvent drops (section 5.1) is published in Journal of Physics D: Applied Physics, while the impact of substrate temperature on the via hole size (section 5.4) and the penetration limit of using inkjet to etch via holes (chapter 6) are published in Applied Physics Letters.

Journal Paper

Yan Zhang, Changqing Liu and David C Whalley, *The impact of substrate temperature on the size and aspect ratio of inkjet-dissolved via holes in thin poly(4-vinyl phenol) dielectric layers*. **Applied Physics Letters**, 102 (10) 2013 pp. 103303.

Yan Zhang, Changqing Liu and David C Whalley, *The penetration limit of poly(4-vinyl phenol) thin films for etching via holes by inkjet printing*. **Applied Physics Letters**, 101 (25) 2012 pp. 253302.

Yan Zhang, Changqing Liu and David C Whalley. *The effect of droplet ejection frequency on the dimensions of inkjet-etched micro-via holes in poly4(-vinyl phenol) thin films*. **Journal of Physics D: Applied Physics**, 45 (12) 2012 pp. 125303.

Conference Paper

Yan Zhang, Changqing Liu and David C Whalley. *Factors influencing the size evolution of inkjet-etched micro-via holes in thin polymer layers*. Large-area, Organic & Printed Electronics Convention (**LOPE-C**), 19-21 Jun 2012, Munich, Germany.

Yan Zhang, Changqing Liu and David C Whalley. *The effect of droplet ejection frequency on inkjet-etched micro via holes*. 12th Electronics Packaging Technology Conference (**EPTC**), 8-10 Dec 2010, Singapore, pp. 236-239.

Yan Zhang, Changqing Liu and David C Whalley. *Direct-write techniques for maskless production of microelectronics: A review of current state-of-the-art technologies*. International Conference on Electronic Packaging Technology & High Density Packaging (**ICEPT-HDP**), 10-13 Aug 2009, Beijing, China, pp. 497-503.

2 Printed Electronics and System Integration

This chapter provides the context of electronics system integration through conventional silicon-based electronics fabrication and the newly emerging printed electronics technologies. Traditional electronic device development follows Moore's Law, which has required new package designs, such as system on chip (SOC), system in package (SIP) and system on package (SOP), to achieve the required continuous performance improvement. It is under such circumstances that via holes become a critical functional structure. It can be foreseen that the same trend will be seen in printed electronics for performance improvement in the near future.

2.1 Conventional Silicon-Based Electronics

The success of modern electronics has been ascribed to the invention of transistors by John Bardeen, Walter Brattain and William Shockley in the 1940s [20]. The core technology today is based primarily on silicon as the semiconductor material. A schematic sketch of the semiconductor fabrication process is shown in Figure 2-1. The entire manufacturing process starts with the growth of highly pure, low defect single silicon crystals. The prepared silicon ingot is then sawed into individual silicon wafers, followed by patterning on each wafer according to the circuit design. Subsequently, wafers are cut into the smallest functional units called dies. Packaging is needed afterwards to protect the die and to achieve electrical interconnection with other components of the system. Due to the demanding requirements of processing and handling silicon, production environments such as vacuum or protective gases are usually needed to prevent contamination or for protection. The utilisation of metals

and other inorganic materials with high melting points also poses challenges in the processing.

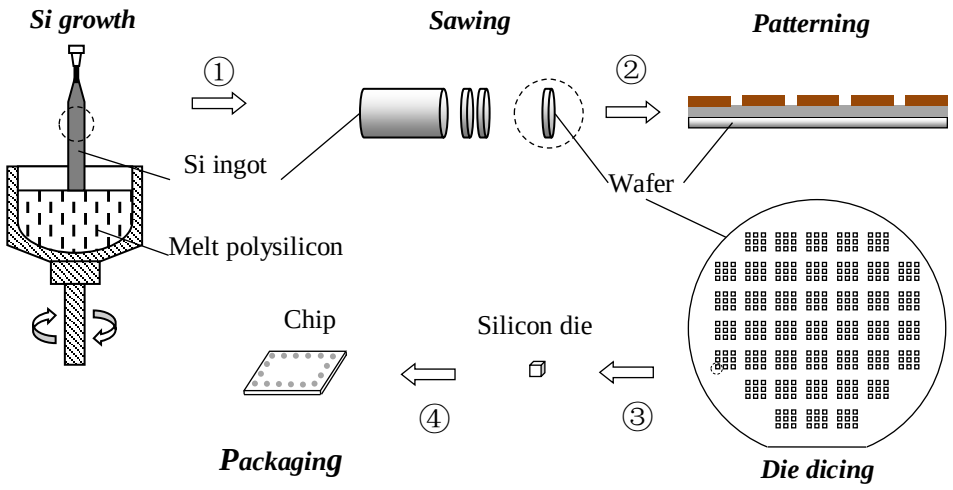

Figure 2-1 An illustration of the semiconductor fabrication process

Figure 2-1 merely illustrates the main procedures of semiconductor manufacturing. Each individual process within this is extremely complex. For example, Figure 2-2 shows the process of producing functional structural patterns on a wafer. A conductive layer, such as Cu, is first deposited on top of a silicon wafer by means of film deposition techniques such as physical vapour deposition (PVD), followed by a layer of photoresist. A premade mask is placed above the photoresist layer, then an ultraviolet (UV) light is used to illuminate the photoresist through the mask. The photoresist layer in the areas where the UV light is received changes its solubility in a developer. The photoresist, where it does not interact with the UV light, retains its original chemical properties. The mask pattern is thereby reproduced in the photoresist after immersing the substrate into the developer solution. The patterned photoresist left after development then functions as a mask for the underlying Cu to be etched and is subsequently removed after the designed pattern is transferred onto the Cu layer. After this, a dielectric material is deposited as an insulating layer in which the Cu pattern is embedded. The process starts over again for multi-layered deposition, but via holes must be created first and then filled with a conductive material so that the Cu patterns in different layers can be electrically interconnected in

the vertical direction. Semiconductor fabrication to produce integrated circuits (ICs) is a high cost industry because of all the expensive materials and equipment used for doping, photolithography and etching in a highly clean environment where temperature, humidity and dust level must be precisely controlled and monitored. It is estimated that over US$3 billion has to be invested to build a sub-micron 300mm semiconductor fabrication plant, commonly known as a fab [21].

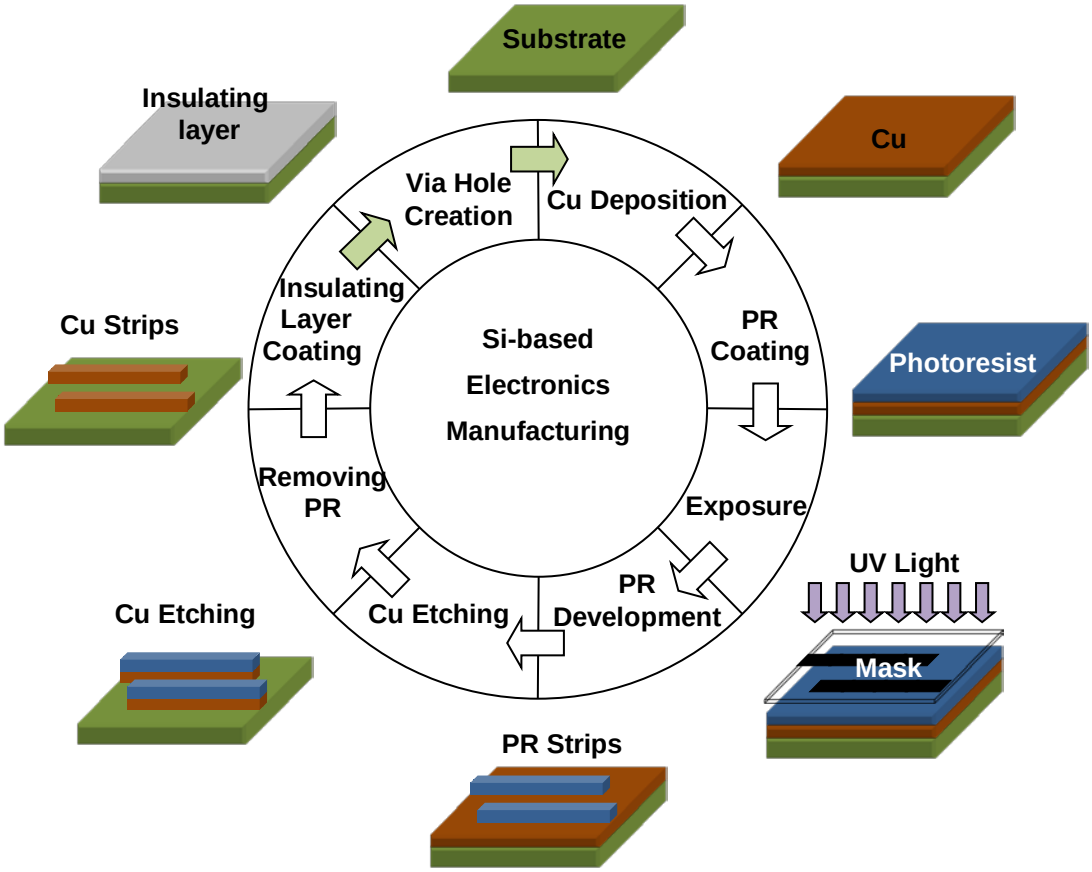

Figure 2-2 An illustration of the Cu patterning process

2.2 Printed Electronics

Printed electronics was initiated due to the discovery and development of conductive polymer, for which the researchers, Alan J. Heeger, Alan G. MacDiarmid and Hideki Shirakawa, were jointly awarded the 2000 Nobel Prize in Chemistry [22,23,24]. Polymers are usually considered to be, and have been widely used as electrically

insulating materials for decades. For a polymer to become electrically conductive, the property of allowing electrons to move freely, in a similar manner to metals, is a prerequisite. Heeger, MacDiarmid and Shirakawa demonstrated the possibility of conduction in polymers by doping polyacetylene with iodine vapour, which boosts the electrical conductivity a billion times. Conductive inks containing metal particles have been commercially available for many years; however, the availability of functional polymers such as conductive and semi-conductive materials has facilitated the boom of printed electronics, due to their ease of processing. This indicates that lightweight and low-cost electronics, smart sensors, flexible displays, batteries and photovoltaic cells can be manufactured through combining cheap polymeric materials with less time-consuming and more cost-effective fabrication processes. Products such as electronic books, flexible batteries, smart sensors, organic solar cells, organic light emitting diode (OLED) lighting, radio frequency identification (RFID) tags and many others have either been demonstrated technically or entered the market, such as the paper phone prototype demonstrated by Queen's University and Arizona State University. [25] Some examples of these products are shown in Figure 2-3.

Figure 2-3 Printed electronic prototypes [i] (a) The system-on-a-sheet demonstrator developed by Linköping University and the Acreo Institute in Sweden [26] [ii] (b) Thinfilm's first scalable printed CMOS (complementary metal-oxide-semiconductor) memory [27]

[i] Reprinted with permission

[ii] Reprinted with permission from Thinfilm Technology

The global market for printed electronics continues to grow and many products are expected to become commercially available in the near future. The global market for printed electronics is expected to increase to more than US$44 billion by 2021, as shown in Figure 2-4 [28].

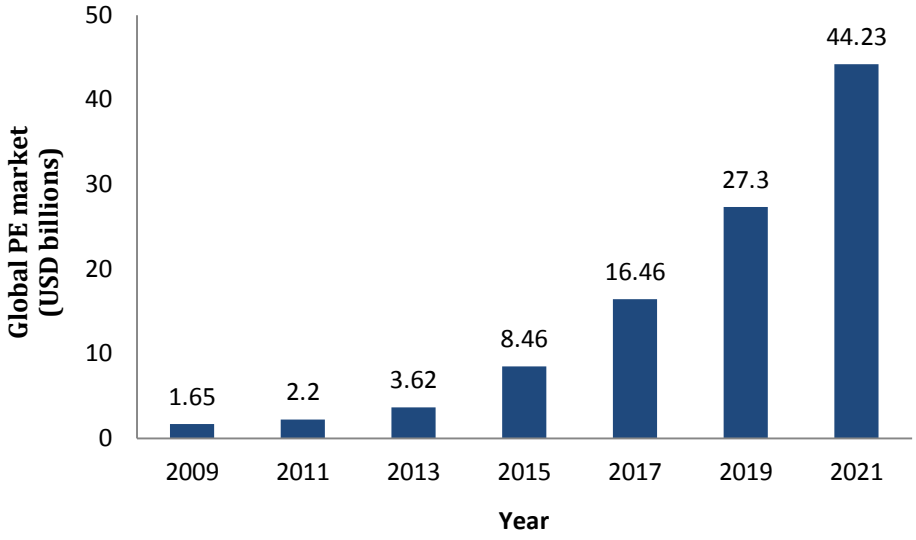

Figure 2-4 Global market growth forecast for printed electronics (USD billions)

2.3 Moore's Law

For integrated circuits, the manufacturing cost per component is almost inversely proportional to the number of components that can be integrated on the circuit. On the other hand, increasing component count leads to the issue of increasing complexity and therefore decreasing yields. This results in a trade-off component count corresponding to the minimum cost at a given time in the development of microelectronics integration, as shown in Figure 2-5 [29].

In 1965, Gordon Moore predicted the increasing rate of transistor density on a single integrated circuit, known as Moore's Law, which states that the number of transistors per IC (integrated circuit) for the minimum cost will double every two years [30,31]. Moore's Law became a self-fulfilling prophecy and the driving force behind the entire semiconductor industry ever since.

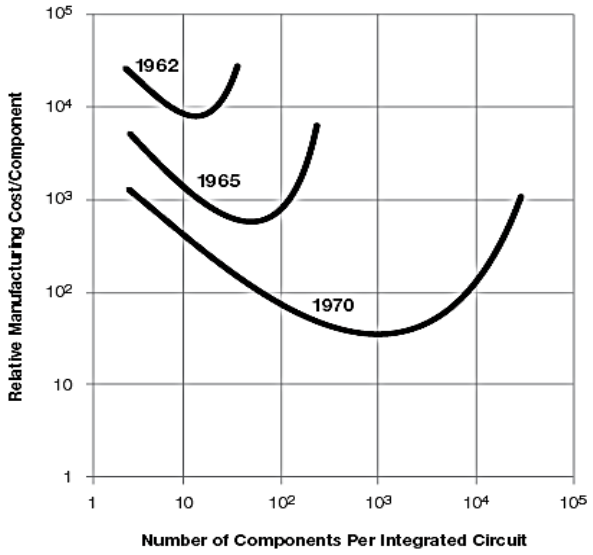

[i] Figure 2-5 The relationship between the number of components integrated on an IC and the unit cost of each component. [29]

One of the solutions for continuing miniaturisation is through geometrical scaling, which is defined as the shrinking of physical feature sizes of the components both horizontally and vertically to boost transistor density, enhance performance and improve reliability [32]. Taking Intel as an example, the first Pentium® 4 processor using a 90nm process contained 125 million transistors on a 112mm^2 die [33]. The number of transistors kept increasing and the feature size continuously shrank in the next couple of processor generations [34,35,36,37]. Intel has succeeded in further reducing the transistors' gate oxide thickness to 0.9nm and the gate length to 30nm on its recent 32nm technology [38]. Figure 2-6 [39] illustrates the continuing trend of CPU (central processing unit) transistor count and feature size. The classic transistor scaling actually ended at 130nm technology [39,40], although technological innovations, such as high-*k* metal gate and fin structures, have been adopted to keep pushing the boundaries [41]. However, further shrinking the transistor size cannot increase transistor density without sacrificing performance. The transition from 65nm technology to 32nm technology has shown that it's already difficult to further reduce the feature size

[i] Reprinted with permission

of transistors, due to the rising challenges such as increased off-state current, increased gate leakage current, etc. [42]. It can be foreseen that it is just a matter of time before gate size will reach the atomic level with the continuing trend of scaling.

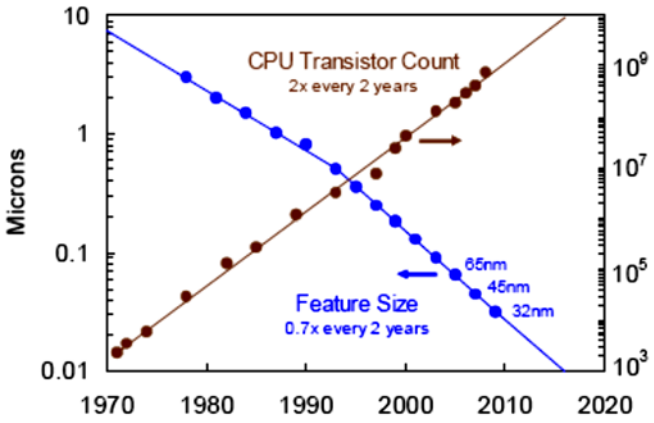

[i] Figure 2-6 The trend of CPU transistor count and dimension scaling [39]

2.4 More than Moore's Law

Since Moore's Law is approaching its physical limits, integration of functionality rather than component density needs to be more closely considered. Therefore, novel architectural designs are needed.

System on chip (SOC) refers to the integration of various functional components into a single chip. If all functional units can be integrated into a single chip and packaged, SOC can offer the most compact and light-weight packaging on the system level [43]. Nonetheless, the complexity of designing such systems and subsequent complicated fabrication processes rarely make it a cost-effective solution. For example, isolation techniques, such as special substrate material utilisation, are needed to reduce the interference between heterogeneous circuits to a minimum [44,45].

System in package (SIP), also known as multi-chip module (MCM), refers to integration of multiple chips in a single package. Each of the silicon chips can perform a specific task and all the chips enclosed in the package together can function

[i] Reprinted with permission

as a system. Even though the whole package performs as a system, there are multiple chips inside each package. Since the fabrication of each type of chip is simplified, the time to market (TTM) for SIP is shortened compared with SOC, and the design risk is lowered.

The concept of system-on-package (SOP) was proposed by Professor Tummala of Georgia Institute of Technology [46]. SOP can be treated as a hybrid of SOC and SIP. Components such as resistors, capacitors, inductors, etc., which are easy to be incorporated in the design phase and will not increase the cost during fabrication, are imbedded in the substrate as thin films instead of being added as traditional bulky components. Other functional modules can be assembled as packages onto the substrate. The packaging efficiency of SOP can be as high as 80% with a component density up to 10,000 per square centimetre, compared with traditional printed circuit board (PCB) assembly techniques, which have a typical area utilisation efficiency of 5%-10% [47] and a typical component density of 50-100 up to 2,500 per square centimetre [48]. The design time and complexity are reduced due to the utilisation of separate chips for multi-functions.

For all of these architectures, especially SOP, via holes are essential for their implementation to provide the vertical interconnection structure between different layers.

2.5 Micro-Via Hole Fabrication Techniques

As discussed above, conventional silicon-based electronics has been driven by Moore's law to continuously achieve smaller feature sizes, higher density and cost-effective production. The micro-via hole structure therefore emerges as an enabling technique to facilitate finer pitch and line width. Micro-via holes are defined by IPC as holes of diameter 150μm or smaller [49]. Via holes can be categorised into blind, buried and through via holes depending on their location in the substrate and their span. A blind via hole is an opening in the outer layer of either side of the PCB connecting the inner layer without going through the entire laminated substrate, as shown in Figure 2-7 ①. A buried via hole is located within the PCB without direct access to the surface on either side, as illustrated in Figure 2-7 ②, and is used for

interlayer connection within the substrate. A through via hole is drilled through the entire board thickness from one side of the substrate to the other, as shown in Figure 2-7 ③, allowing it to connect all layers of the PCB. This type of via hole is used particularly for mounting components onto the PCB. A brief introduction to the two main techniques used for via hole drilling in PCBs - mechanical drilling and laser ablation - will be given in the following discussion.

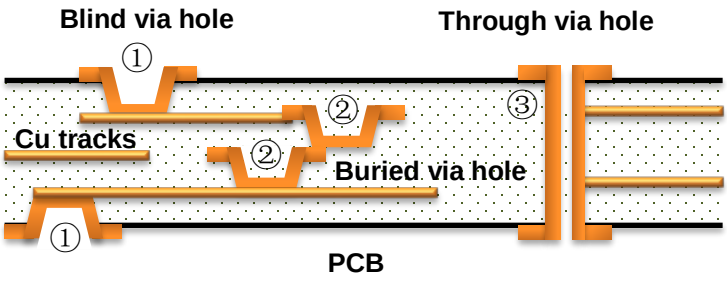

Figure 2-7 Classification of via holes in a laminated PCB

2.5.1 Mechanical Drilling

Mechanical drilling is the most widely used method for creating holes on PCBs, with the hole diameter typically being over 200µm. This technique is efficient for drilling the large through-holes in PCBs required for mounting through-hole components. Drill time can be easily controlled for the process and less thermal induced deformation can be found compared to other high energy drilling techniques. Additionally mechanical drilling can fabricate deeper holes with better straightness, roundness and surface finish [50]. However, using this method for drilling micro-via holes with a diameter below 150µm, or blind via holes where the dielectric layer is thinner than 50µm, presents technical, cost and productivity issues. Brittle materials are difficult to drill, even using a diamond bit [51]. Forming small holes with miniature drill bits can cause breakage when tools clog with the drill material due to their low strength [52]. Additionally, raised edges and small material debris, also known as burrs, pose difficulty in removal [53]. Nonetheless, the transition from conventional mechanical drilling to micro-via hole drilling is still underway. Researchers have been investigating the factors that can affect the formation of burrs, including the exit

surface angle, feed, drill design, etc. so as to minimise it [54,55,56,57,58]. Okasha, *et al.* have demonstrated a hybrid technique of laser and mechanical micro-drilling, which enhances the life of microdrills and alleviates some issues of each individual technique [59]. With the new electric field sensor (EFS) technology, the depth accuracy for blind vias can be reduced from ±50μm to ±5μm [60].

2.5.2 Laser Ablation

Laser ablation employs a laser to remove material from the substrate. Laser ablation has two mechanisms: photothermal ablation and photochemical ablation. In photothermal ablation, a laser source with a wavelength between 500nm and 10.6μm is utilised. The substrate material heats up by absorbing the laser energy and vaporises into the surroundings leaving a hole in the substrate. Photochemical ablation uses laser sources with much shorter wavelengths in the UV spectrum, so that chemical bonds can be broken up at the molecular level. The resulting debris expands in volume and is forced to eject from the affected area as powder, leaving a via hole locally. Due to the heat-affected and carbonised sidewalls of via holes produced by photothermal ablation, cleaning is usually required before subsequent plating. Photochemical ablation, however, does not always require cleaning. The cleaning agent for holes produced by photochemical ablation, if necessary, is also milder compared with that used in photothermal ablation.

Laser ablation can be an excellent alternative to mechanical drilling tool, especially for brittle materials or hole diameters less than 250μm which are difficult to achieve with conventional mechanical drilling [61]. The finest feature size that can be achieved with laser ablation is confined to the spot size of the focused laser beam, which with current practices allows for fabrication of via holes with diameters less than 70μm [62]. The advantages of laser ablation over mechanical drilling are that it is free of tool wear, breakage and clogging problems. But the heat-affected zone around the created holes poses problems for subsequent plating, and further treatment complicates the process and increases the cost [63].

2.6 Summary

This chapter has mainly discussed the basic concepts behind this research, providing the background information and context for inkjet-printed via hole investigation. Printed electronics has many advantages over traditional Si-based electronics, such as low cost, light weight and digital production. It is expected to demonstrate its suitability in arenas such as flexible displays and smart packaging where reliability demands are not high, rather than a substitution of Si-based electronics. As the traditional electronics industry is driven by Moore's law, which manifests itself in reduced size of electronic devices, enhanced performance and cheaper prices, such development can be applied to printed electronics as well. As the printed electronics industry advances to multilayer structures for more compact integration and greater functionality, vias will be very important in accomplishing system integration so that the performance of printed electronics keeps improving. The main difference for via creation between conventional and printed electronics is the aspect ratio, due to its flexibility. With organic thin film structures, it can be expected that the required aspect ratio will be much less than required in conventional electronics. Inkjet printing, therefore, emerges as a promising candidate for via creation, due to the elimination of alignment issue and its good process integration for all-printed electronics.

3 Direct-Write Techniques for Printed Electronics

For the last decade, there has been growing interest in direct-write methods for the manufacturing of microelectronic products. The entire electronics industry has always aimed to achieve low cost, rapid manufacturing and shorter time-to-market, and more recently, reduced environmental impacts. Direct-write technology can offer contributions toward all these goals.

This chapter intends to give a comprehensive introduction to direct-write technology by reviewing the main direct-write techniques, most of which have been invented or seen significant development during the last decade. These techniques primarily include the following four categories: droplet-based direct writing, filament-based direct writing, tip-based direct writing, and energy beam direct writing. Within each category, specific techniques are presented as examples of the classification by discussing their working principles, capabilities and possible applications.

3.1 Definition of Direct Writing

Various definitions of direct writing have been given by different researchers [64,65,66,67]. In this chapter, by considering these existing definitions, direct writing is defined as a technology that enables the deposition of various materials only where it is necessary, including both functional and structural components, directly following a pre-set layout in a data-driven way without utilizing masks or subsequent multiple subtractive processes. After material deposition onto the substrate is completed, a further post-treatment process is often needed and is activated through the input of

heat or other radiation, in order for the deposited material to fully achieve its functional properties.

3.2 Drivers and Advantages

The current manufacturing of microelectronic products generally involves intricate photolithography procedures, as schematically depicted in Figure 2-2. Masks are required to transfer the designed patterns. Using such masks requires additional intricate fabrication processes, resulting in additional overall manufacturing cost and time [68,69]. Besides, in such manufacturing, film deposition within a vacuum environment is usually necessary. However, much of these layers are removed subsequently. Such processes are often highly material- and energy-consuming, such that a 2g microchip has been estimated to consume 1.7kg of non-renewable resources [70].

Direct writing is, therefore, emerging as a potential alternative approach to the fabrication of microelectronic devices. Direct-write techniques promise added value in that they can interface directly with the output from computer aided design (CAD) software to generate circuit patterns. They are agile as any changes made within the CAD system can be immediately implemented without the delays associated with the fabrication of revised masks. Therefore, they enable the rapid prototyping of a new product, in comparison with traditional costly and time-consuming mask fabrication and photolithography processes. In addition, direct-write techniques can minimize the usage of materials and potentially reduce energy consumption, thereby reducing the large environmental burdens traditionally associated with electronics manufacture [71].

3.3 Classification of Direct-Write Technologies

A variety of direct-write methods have been invented and developed over recent years. Most of the existing direct-write techniques can be classified into one of these four categories: (1) droplet-based direct writing; (2) filament-based direct writing, which is sometimes referred to as a continuous approach or flow-based technique; (3) tip-based direct writing; and (4) energy beam direct writing. The following subsections will discuss each of these in turn.

3.3.1 Droplet-Based Direct Writing

3.3.1.1 Inkjet Printing

Inkjet printing has demonstrated its power over the last two decades in areas such as home and small office printing applications. However, the fundamental physical principle utilised has long been known and can be dated back to the 19th century when Plateau discovered the phenomenon that a liquid jet with an imposed disturbance can split into individual droplets and Rayleigh further contributed seminal work from a mathematical perspective [64,72]. Recently, applications in flat panel displays, printed electronics, MEMS (micro-electro-mechanical systems), wireless communication, etc. have become the driving force behind the adaptation of inkjet printing [64].

There are two main types of inkjet technologies: continuous jetting and drop-on-demand (DoD). For the DoD inkjet printer, ink droplets are ejected from the orifice only when there are pulse signals to trigger this process. No ink droplets will be formed without such pulses, as the name drop-on-demand implies.

For DoD systems there are two main types of actuation method used in commercial inkjet printers: piezoelectric inkjet nozzles and thermal inkjet nozzles. In a piezo-type inkjet head, the actuation method relies on the deformation of a piezo-electric material to create the pressure to eject a droplet from the nozzle, as illustrated in Figure 3-1. Piezoelectric materials are capable of transforming external mechanical deformation into electrical signals, and vice versa. When an electrical voltage is applied to the piezo-material, it deforms in response to the signal input. Material expansion caused by the applied voltage propels an ink droplet from the orifice and more ink is then drawn from the reservoir to refill the cavity in compensation for the pressure discrepancy when the voltage disappears and the piezo-material returns to its previous steady state dimensions.

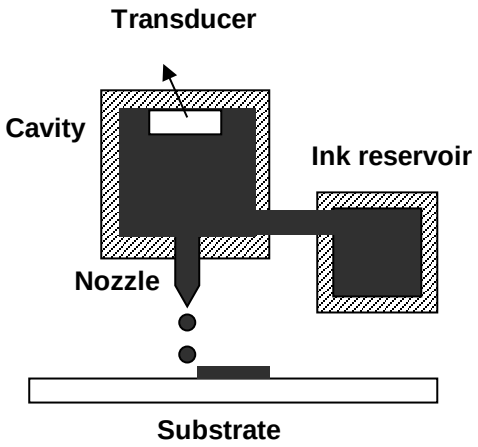

Figure 3-1 The configuration for a drop-on-demand inkjet printer

In a thermal inkjet nozzle, when printing is required, an electrical pulse is applied to a small ohmic heater in the nozzle, and the generated heat vaporises a small quantity of the volatile ink so as to form a bubble. When this happens it creates a pressure difference between the interior and exterior of the nozzle, resulting in a droplet being ejected from the orifice and propelled towards the printing substrate. As the heater cools down, the bubble collapses and a pressure difference between the interior and exterior of the ink cavity again occurs. Therefore, ink is replenished into the cavity from the reservoir to restore the pressure balance. The range of materials that can be jetted using a thermal inkjet nozzle is more limited since it requires inks that possess the capability of being vaporised.

In a continuous inkjet printer, as shown in Figure 3-2, a transducer, made from piezoelectric material for example, is used to generate high frequency pressure waves in the ink cavity in response to the application of electrical signals. A continuous stream of ink fluid in the ink cavity goes through the nozzle and issues from the orifice, due to the presence of pressure, and breaks up into individual uniform droplets in response to the waveform. Ink droplets are jetted from the orifice continuously at high frequencies and travel through a pair of charging plates. Subsequently, they are selectively directed to the specific intended location by a deflection electric field. Those not needed will be collected into a gutter and may be recycled for later reuse.

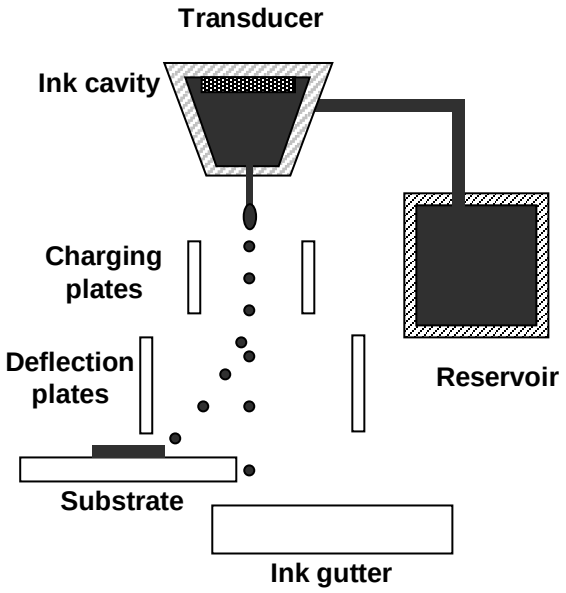

Figure 3-2 The configuration of a continuous inkjet printer

Compared with continuous printing, ink droplets only form when triggered by a pulse signal in the DoD mode. Therefore, there will not be any ink collection issues in DoD printers. Both types of systems are available from a range of vendors, as either a print head or a full printing system. The diameter of the orifice is the main determinant of the droplet volume and consequently the feature resolution that can be achieved. The resolution also depends on several other factors such as wettability of the ink onto the substrate, ink curing speed, and so on. For DoD systems, the droplet size is approximately the diameter of the nozzle and the achievable droplet diameter ranges from 15μm to 100μm [73]. The droplet generation rate can be up to several thousand hertz. In continuous mode inkjet printing systems, the generated droplets are usually twice as large as the nozzle diameter. Droplets as small as 20μm or as large as 1mm have been observed, with 150μm being the typical feature size for continuous mode inkjet printing systems. Droplet generation rates for commercially available continuous mode inkjet printing systems range from 80 kHz to 100 kHz [64].

Although inkjet printing is a non-contact, high resolution digital printing process, it encounters a major problem of its own: inkjet formulation, which can determine the droplet behaviour during the drop formation process and the quality of the printed

pattern. Most commercially available inkjet printers require a material viscosity range between 10cP and 20cP. Therefore, the materials need to be formulated into inks within this viscosity range to be successfully jetted. Challenges such as particle dispersion and precipitation, and achievable ink conductivity need to be resolved before it can enjoy a broader popularity in industrial printed electronics applications.

3.3.1.2 Aerosol Jet

Aerosol Jet is another additive droplet-based process, which was initially developed to study the feasibility of elimination of solder from electronics for military applications. The Aerosol Jet system has two main components: the atomizer and the deposition head, marked as ① and ② in Figure 3-3 respectively. The raw material to be deposited must be in a liquid form and is first placed into an either ultrasonic or pneumatic atomizer, which is utilised to generate a dense aerosol of material droplets. Then, the generated aerosol is transferred into a tightly confined jet within the deposition head by a gas flow running through the atomizer and out into the deposition head. The aerosol stream brought into the deposition head is further focused by a second gas flow introduced into the jet. The aerosol stream and the newly introduced sheath gas flow interact with each other and form a co-axial annular flow, which then leaves the deposition head through a nozzle attached to it and lands on the substrate. A laser module can be integrated into the system to locally complete any required thermal post-processing of the deposited material.

The Aerosol Jet system provides a non-contact method of printing which, like inkjet printing, makes it compatible with processes where contamination of the substrate must be avoided, *i.e.* printing on silicon substrates. Researchers have demonstrated printing on untextured silicon wafers using the Aerosol Jet printing system [74]. The stand-off distance between the deposition head and substrates can be adjusted between 1mm to 5mm.

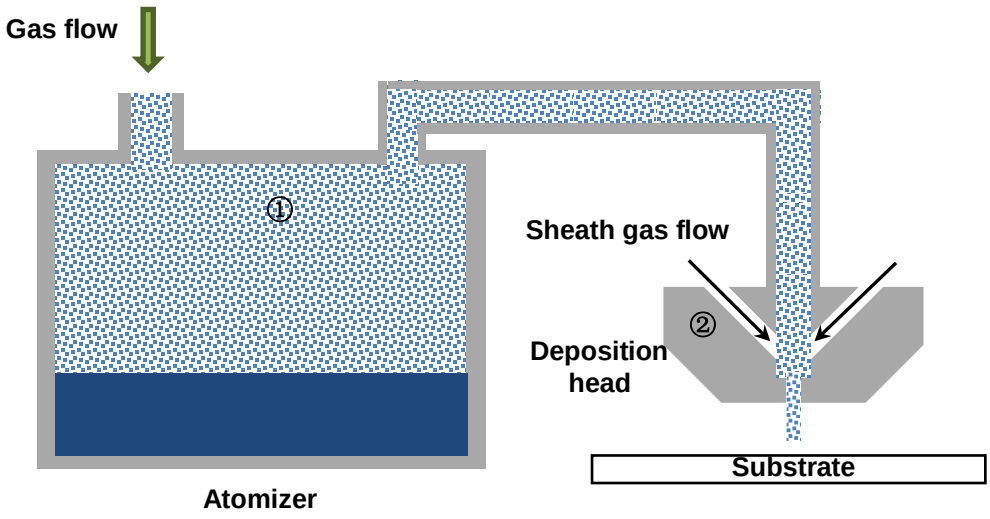

Figure 3-3 Illustration of the Aerosol Jet operating principle

The Aerosol Jet system can create lines as fine as 10 microns with a minimum pitch of 20 microns, or as wide as 150 microns. The viscosity of the materials that can be jetted using an Aerosol Jet system ranges between 1cP and 2500cP, which enables the deposition of a wide selection of materials[75].

3.3.2 Filament-Based Direct Writing

3.3.2.1 MicroPen Writing

MicroPen writing was developed by MicroPen Technologies Corporation. The working principle of MicroPen writing can be described as follows: the material to be deposited is first loaded into a syringe, which is connected with the writing head, referred to as a "block" by the system vendor. The material is squeezed out of the syringe into the writing head by compressing the plunger of the syringe using a pneumatic ram. The material transferred into the "block" is then pressurized up to almost 14MPa (2,000 psi), from where it flows into a micro-capillary writing tip, which deposits the material onto the substrate. A schematic configuration of the MicroPen writing system is presented in Figure 3-4[76].

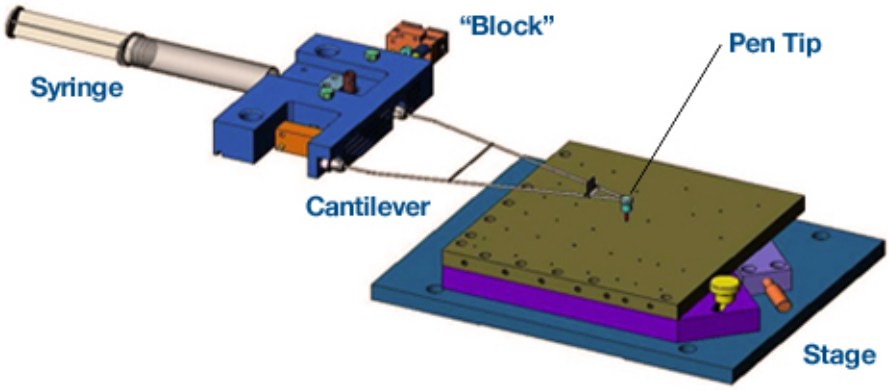

[i] **Figure 3-4 Configuration of the MicroPen writing system** [76]

MicroPen direct writing can deposit potentially any liquid material in the viscosity range between 0.005 and 500 Pa·s (5 to 500,000 centipoises). The resolution of MicroPen writing relies on pen-tip size, the rheological properties of the material to be dispensed and the writing process parameters such as the extrusive gas pressure, the stand-off distance between the dispensing tip and substrate, and the tip writing velocity on the substrate. The appropriate stand-off distance between the pen tip and substrates to ensure continuous and smooth material dispensing has been found to be 1 to 2μm more than the thickness of the film being deposited [77].

3.3.2.2 nScrypt Direct Printing Dispensing Tool

nScrypt's Smart Pump™ is able to dispense materials with a viscosity up to 1,000 Pa·s (1,000,000 cps) through the use of accurately controlled air pressure, valve opening and dispensing height [78].

[i] Reprinted with permission from Micropen Technologies

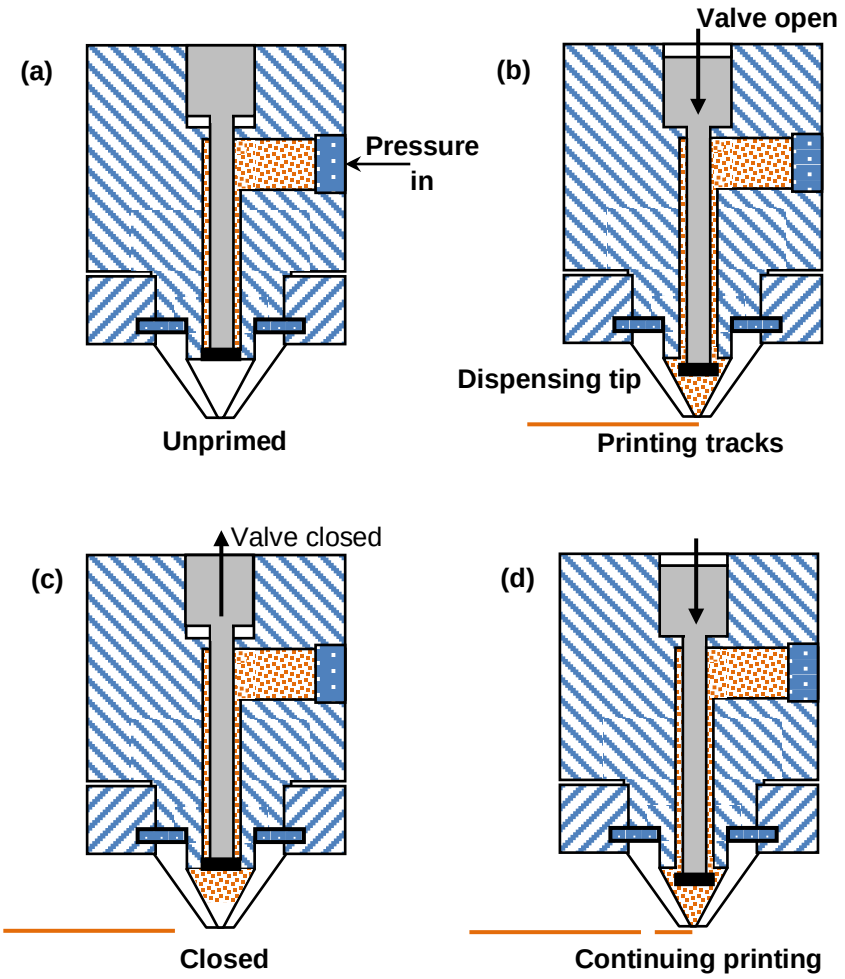

Figure 3-5 The Smart Pump™ dispensing process

The dispensing process is illustrated in Figure 3-5. When dispensing is initiated, a computer-controlled needle valve opens so as to allow the material to flow through the dispensing tip onto the substrate, as illustrated in Figure 3-5 (b). Once dispensing stops, the valve closes to block material from leaking. One advantage of the smart pump is that it sucks back excess material into the dispensing nozzle when deposition is terminated. A negative pressure is maintained in the dispensing tip chamber to induce sucking back of this material when deposition ceases. This feature allows the orifice to be left clean and clear without any agglomeration of material or the possibility of nozzle clogging, and delivers a consistent start every time dispensing commences. Consequently, line printing can be precisely controlled and the width of the dispensed material can remain consistent without bulges of materials at the start of

dispensing. The Smart Pump™ is available in two models for different applications. Their technical specifications are listed in Table 3-1 [79].

Table 3-1 Technical specifications of Smart Pump™ models

	Smart Pump ™ 20	Smart Pump ™ 100
Size	25.4mm×25.4mm×152.4mm	25.4mm×38.1mm×152.4mm
Air Pressure	0-100 psi available	
Tip	nScrypt patterned ceramic tip, standard tip from 12.5μm to 200μm; up to 3mm tips available; Luer lock tip	
Volumetric Control	20picolitres	100picolitres
Operating Frequency	20Hz (material dependent)	2Hz (material dependent)
Fluid Viscosity	0.001-1,000Pa·s (1-1,000,000 cp)	

3.3.3 Scanning Probe Microscope-Based Direct Writing

Scanning probe microscope-based direct writing, also known as tip-based direct writing, usually utilises the tip of an atomic force microscope (AFM) as the writing tool for fabrication of patterns.

3.3.3.1 Dip Pen Nanolithography

Piner, *et al.* discovered this technique while investigating a phenomenon: condensed water can either be transported from the substrate to the AFM tip, or vice versa, depending on the relative humidity and substrate wetting properties [80]. The DPN technique is analogous to a quill pen on a nanoscale, delivering molecules from the dispensing AFM tip onto substrates, and is especially useful in nanoscale applications. Due to the capillary effect, the AFM tip is capable of dispensing ink adhering to it, from previous dipping, onto substrates which have an affinity for the ink, as shown in Figure 3-6. An ink meniscus occurring between the AFM tip and the substrate helps transporting ink from the pen tip to the substrate. Scalability has been demonstrated using arrays of up to 55,000 tips [81].

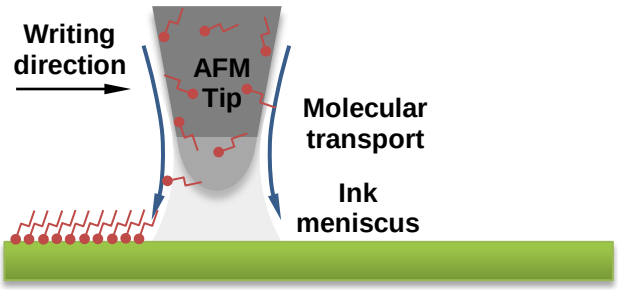

Figure 3-6 A schematic illustration of dip pen nanolithography

Jang, *et al.* demonstrated using DPN to write letters on a gold surface with 16-mercaptohexadecanoic acid and the obtained line width was about 15nm [82]. However, the finest resolution that this process can achieve is still uncertain [64]. Researchers have shown that conventional DPN also works for high melting point compounds, such as octadecylphosphonic acid (melting point 100°C), as long as they have some solubility in the ink meniscus [83].

3.3.3.2 Thermal Dip Pen Nanolithography

Traditional DPN requires that the ink to be dispensed is in the liquid state under ambient conditions. Therefore it poses two limitations: first, the ink deposition rate can only be adjusted by altering the ambient humidity or temperature; second, ink deposition during DPN is difficult to turn off due to the mobility of ink under ambient conditions, which may cause smearing [84]. Thermal dip pen nanolithography (tDPN) is a modified version of DPN, as illustrated in Figure 3-7. A heater is integrated internally with the cantilever. The coated material on the pen tip melts upon being heated and flows over the pen tip onto the substrate. Ink dispensing ceases when heating terminates and the ink becomes solid.

It is claimed that using meltable inks has many advantages. Writing can be switched on and off readily and the ink flow rate can be varied easily by controlling the tip temperature. Complex 3D structures can be generated through writing layer by layer, with the previously deposited layer being solid. It is compatible with other traditional semiconductor manufacturing methods, since thermal dip pen

nanolithography can be performed in vacuum [85]. tDPN can be useful for transferring metallic and certain other materials that are not only solids at room temperature, but also have no appreciable solubility in a carrier solvent [83]. Researchers have successfully demonstrated that continuous indium tracks as fine as 80nm can be written onto glass or silicon substrates [85]. Chung, *et al.* reported writing 16-mercaptohexadecanoic acid (MHA) lines onto gold substrates and achieved a feature size smaller than 100nm [86].

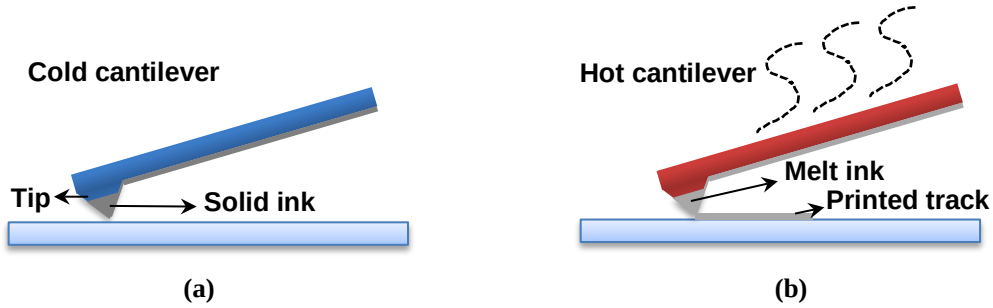

Figure 3-7 The tDPN working principle

3.3.3.3 Nanofountain Probe

The fact that ink needs to be replenished during DPN printing makes the dispensing speed slow and the throughput limited. The inevitable realignment required after ink replenishment also complicates the process. The nanofountain probe (NFP) was, therefore, developed to address these issues. Figure 3-8 illustrates the NFP working principle: NFP is composed of a volcano tip, integrated microchannels and an on-chip reservoir. The reservoir is supplied with an ink solution, which is driven by capillary action to the volcano tip continuously through the microchannel to form a liquid-air interface at the annular aperture of the volcano tip, as illustrated in Figure 3-8(a). Ink molecules are then transferred from the liquid-air interface to a substrate via an ink meniscus between the core tip and the substrate through capillary action, as illustrated in Figure 3-8(b). The capabilities of the NFP have been demonstrated by successfully writing lines as fine as 40nm. A new generation NFP device with two on-chip ink reservoirs feeding a linear array of 12 microfluidic cantilever probes has been developed by researchers, demonstrating its scalability [87].

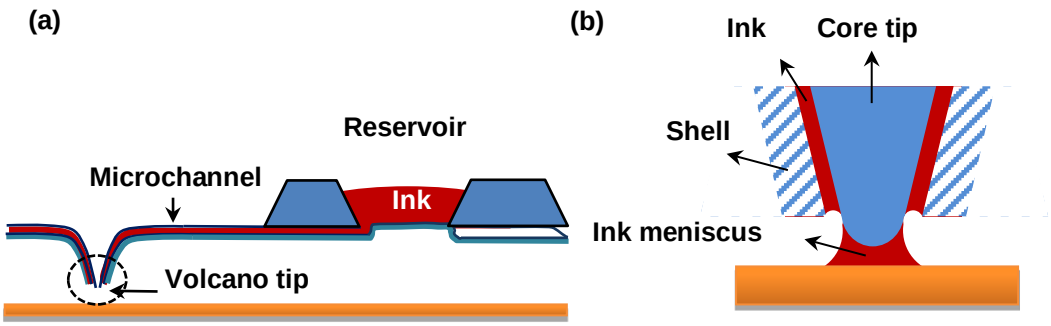

Figure 3-8 The working principle of NFP printing (a) the configuration of NFP (b) the configuration of the volcano tip

3.3.3.4 Electrochemical Dip-Pen Nanolithography

Electrochemical dip-pen nanolithography (E-DPN) enormously expands the range of materials that can be deposited using tip-based methods. Figure 3-9 is an illustration of the E-DPN configuration. In an E-DPN process, the ink meniscus formed between the tip and substrate serves as not only the ink transfer medium, but also an electrochemical cell. Metal salts can be dissolved into the ink meniscus, reduced into pure metals electrochemically, and deposited on the substrate surface.

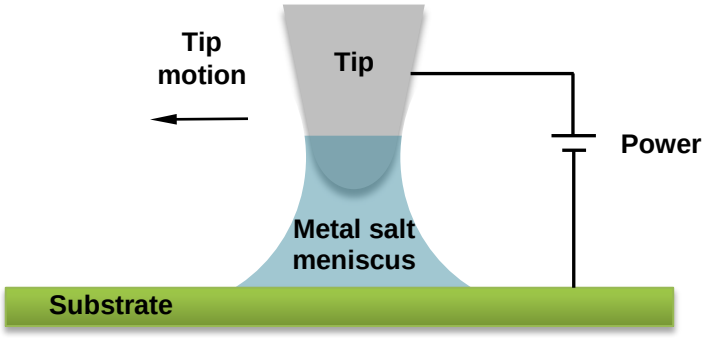

Figure 3-9 A schematic illustration of E-DPN. The meniscus is composed of metal salt working as electrolyte solution.

It has been observed that the feature size which can be achieved by the E-DPN technique depends on factors such as the humidity, writing speed, and the voltage bias. The deposition of several metals and semiconductors on silicon substrates has been

investigated and, for example, platinum lines with a width of 30nm and thickness of 0.4nm have been successfully demonstrated [88].

3.3.3.5 Polymer Pen Lithography

Polymer pen lithography (PPL) is a high-throughput and low-cost tip-based direct writing method for large-area contact printing. It uses soft elastomeric polymer tip arrays instead of AFM tips. Theoretically thousands, or even millions, of these pyramid-shaped polymer pens could be fabricated together into a polymer pen array. Much larger features can be rapidly accomplished through dispensing materials onto the substrate by all pen tips simultaneously. The PPL array is allowed to absorb ink for some time before patterning [89]. When the tips of the polymer pen array contact the substrate, their coating of ink is delivered onto the substrate. Spot feature size ranging from 90nm to hundreds of microns can be achieved by altering ink delivery time and force [90].

3.3.4 Energy Beam Direct Writing

3.3.4.1 Laser Direct Writing (LDW)

Lasers are energy sources capable of delivering highly focused energy, which have resulted in applications in material removal and heating, e.g. cutting, drilling and welding. Applications of lasers in direct writing technology started with the development and growth of laser micromachining [64] as a subtractive process, but then quickly started thriving in additive manufacturing.

3.3.4.1.1 Laser Chemical Vapour Deposition (LCVD)

Laser chemical vapour deposition (LCVD) is similar to traditional chemical vapour deposition (CVD), but has a localised spot heat source instead of a global heat source as in a CVD furnace. A chamber is filled with a gaseous precursor which contains the elements to be deposited. The laser beam scans over the substrate and heat transfers to the gaseous precursor from the spot heat source provided by the laser. This leads to thermal decomposition of the reagent molecules locally and a thin layer of the material to be deposited precipitates onto the substrate. The growth of the

deposition layer is confined to only where the laser beam scans. Repeated scanning of the substrate by the laser can build up multi-layered deposits.

Bondi, *et al.* [91] have demonstrated using LCVD to grow carbon nanotubes and achieved 170μm wide nanotube lines. Foulon and Stuke [92] reported aluminium lines 0.7μm thick and 7μm wide from a single scan. Researchers have also demonstrated the potential of LCVD in three dimensional applications. Wanke, *et al.* [93] created Ø40μm Al_2O_3 rods with a length of 3mm and Williams, *et al.* [94] successfully demonstrated growing Ø14μm carbon micro-coils.

3.3.4.1.2 Laser Assisted Plating

Laser assisted plating was first reported by von Gutfeld, *et al.* [95,96,97]. The substrate was submerged into a salt bath which contained the metal to be deposited. A laser was used to irradiate the substrate leading to a temperature rise locally where the laser passed through. The increased local temperature was high enough to decompose the bath to reduce metal ions back to their metallic state and a layer of metal was deposited on the substrate.

Chen, *et al.* [98] have demonstrated copper track fabrication from copper formate ($Cu(HCOO)_2$) on Si substrates by laser enhanced electroless plating. Line widths of 2-12μm and thicknesses of 0.25-1.2μm were obtained. Wee, *et al.* [99] also used laser assisted electroplating to fabricate Cu tracks. The widths of the Cu tracks obtained at different scanning speeds ranged between 450μm and 660μm. They also showed that normally the widths of the tracks are wider than the laser spot diameter owing to heat diffusion.

3.3.4.1.3 Laser-Induced Forward Transfer (LIFT)

Laser-induce forward transfer (LIFT) was introduced by Bohandy, *et al.* [100]. Figure 3-10 is a schematic description of the apparatus used by Bohandy. A pulsed excimer laser was employed. The wavelength and the pulse duration were 193nm and 15ns respectively. This technique was used to deposit Cu lines onto a silicon substrate. Materials to be deposited are first deposited on a laser-transparent support as a thin film layer. The support with the thin film on it is brought close to the targeted

substrate. The laser used is focused by a lens through the laser-transparent support at the interface between the transparent support and the thin film source layer, where it induces some of the target material to vaporise and propel the rest of the material onto the receiving substrate. This method utilises a solid state precursor and thus eliminates the gaseous precursors which are necessary in a LCVD process, thereby eliminating any contamination problems presented by the precursors. It has been shown that decreasing the pulsed laser energy reduces the line width, while thicker films require higher laser power.

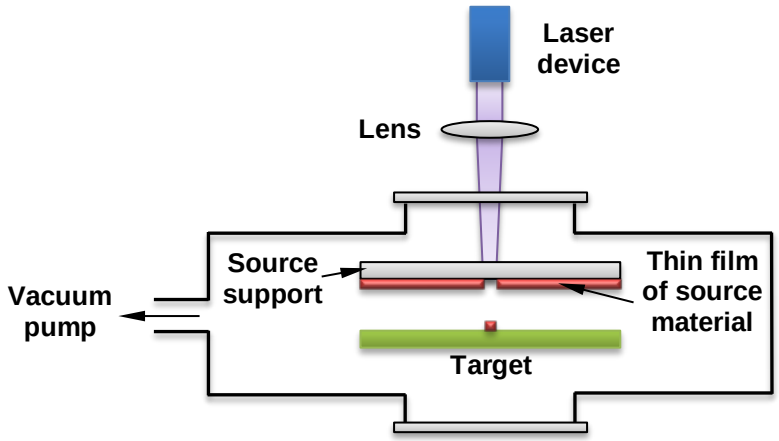

Figure 3-10 The configuration of a LIFT apparatus

Claeyssens, *et al.* [101] demonstrated the use of LIFT to create a patterned Zn layer on a Si substrate as a precursor for later ZnO nanostructure growth. The achieved line widths were 10µm and 30µm respectively for the in-vacuum and in-air patterns. Zn lines deposited in vacuum showed superior resolution and adhesion. Currently the writing resolution for the LIFT technique is in the order of 10µm.

3.3.4.1.4 Matrix Assisted Pulsed Laser Evaporation (MAPLE)

Figure 3-11 is an illustration of the MAPLE dispensing principle. A laser transparent quartz ribbon, coated with the material to be deposited and an organic binder (together known as the matrix), is used. The matrix adhered to the ribbon is brought into close proximity (5 to 100µm) with the substrate. When the laser is focused onto the interface between the ribbon and the matrix, it vaporises a portion of

the organic binder, and the vapour at the interface repels the remainder onto the substrate. The laser does not vaporise the material to be transferred, since its power is tuned below the threshold for ablating it. When the process is optimised, the evaporating organic binder can gently desorb the source material to leave it intact and transfer it onto the substrate.

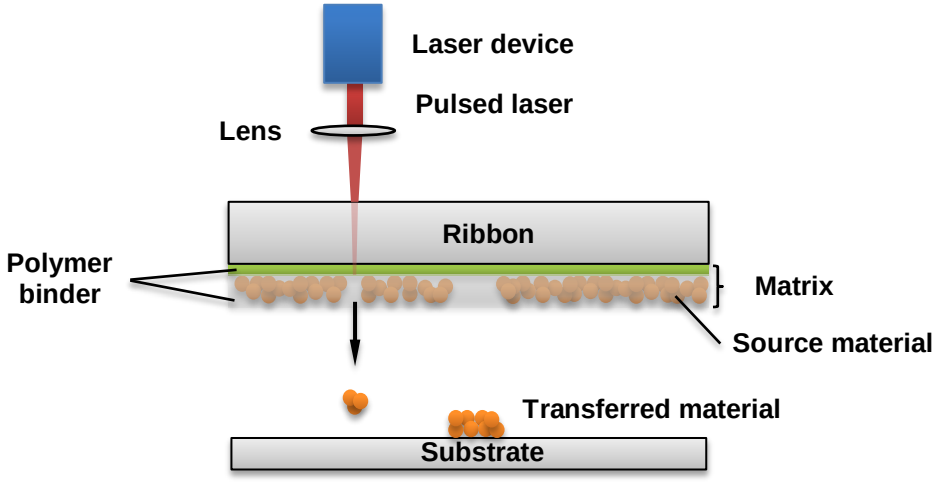

Figure 3-11 The dispensing principle of the MAPLE

MAPLE direct writing was originally proposed by Piqué, *et al.* for electronics and sensor production [102,103]. Table 3-2 lists the experimental parameters used by Piqué, *et al.* and the feature thickness of each device. The widths of the features were not mentioned explicitly, but it can be inferred that it ranged from tens to a hundred microns.

Table 3-2 Experimental parameters and feature size of devices fabricated by MAPLE DW [102]

Device	Material	Spot size (μm)	Fluence (mJ/cm^2)	Number of Passes	Thickness (μm)
Lines	Ag	100	500	10	10
Parallel-plate capacitors	BTO ($BaTiO_3$)	25	500	25	20-25
Interdigitated capacitors	STO ($SrTiO_3$)	25	500	20	5-20
Flat inductors	YIG ($Y_3Fe_5O_{12}$)	25	550	25	20
Chemoresistors	PECH (polyepichlorohydrin) /graphite	25	250	40	N/A

3.3.4.2 Focused Ion Beam (FIB) Direct Writing

Focused ion beams (FIBs) have been widely used in nanofabrication for microelectronics. FIBs can be used to pattern materials with nanometre dimensions by ion implantation, lithography, ion milling, gas-assisted etching, etc. [104]. FIB-induced deposition is similar to LCVD, except that an ion beam is used as a substitute for photons. A local ambient of precursor containing the target material is maintained on the surface of the substrate through a gas nozzle. A FIB passes across the surface and decomposes the precursor where ions are incident. The desorbed volatile products are removed from the chamber and the desired pattern of deposited material remains on the surface as a thin film. A schematic illustration of the FIB induced deposition principle is shown in Figure 3-12.

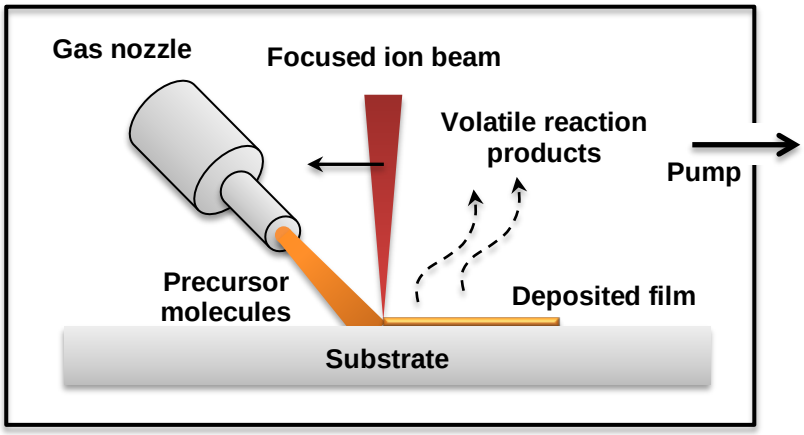

Figure 3-12 A schematic illustration of the FIB induced deposition principle

One issue in laser patterning is that the laser-induced deposition usually generates transition regions as large as 2-4μm. However, a FIB can create features as fine as the beam diameter, which can be focused to as small as 20nm, and therefore promises potentially very high resolution deposition. Additionally, the thermal effects of the incident ion beam are less significant [104].

Reyntjens, *et al.* [105] have explored FIB applications in microsystems technology, and successfully fabricated three dimensional structures. A rectangular deposition of SiO_2 walls with an aspect ratio as high as 7.5 (height (μm) : width (μm)=3.0:0.4) have been fabricated. Li, *et al.* [106] demonstrated using low-current FIB-induced deposition

of three-dimensional nanoscale tungsten rods with a sectional diameter of 230nm. Tao, *et al.* [107,108] fabricated platinum lines as fine as 0.3μm. Della Ratta, *et al.* [109] have created copper interconnects with a width of 0.25 μm. FIB-induced deposition of other materials such as opaque carbon films, gold and aluminium have also been studied [110,111,112].

3.3.4.3 Thermal spraying

Thermal spraying is a process which uses heat as the energy source to accelerate materials to a high velocity towards a substrate to generate spray deposit. Materials to be deposited are injected into a high velocity combustion or thermal plasma flame, which transfer the thermal and kinetic energy of the flame to the particles to be deposited. The materials, upon obtaining the energy, impact on the substrate and solidify rapidly.

Thermal spraying is commonly used for large area metallic coating deposition, and has found its application in thick ceramic coating deposition as well [113]. Most thermal spray research has been focused on large area applications, such as film coating. However, the utilisation of thermal spraying as an additive method in fabrication of meso-scale (100μm-10mm) structures, such as in sensor fabrication, has been initiated [64]. Recent innovations have enabled the deposition of high-quality functional multilayers for sensors and electronics by thermal spray techniques [114,115]. Longtin, *et al.* [116] succeeded in fabricating thermocouples with a plasma spray, which respond to a temperature range between room temperature and 900°C.

3.4 Summary

In this chapter, DW methods have been reviewed and categorised into four main groups. Table 3-3 lists the DW techniques discussed and compares their features.

Even though DW technologies demonstrate great potential and advantages over traditional manufacturing in terms of material consumption, cost and simplicity, challenges and problems still stand in the way. For example, novel ink design and formulation, better modelling of ink dynamics during deposition and more powerful control systems allowing patterning in 3D at nano-scale resolution are required for the

ink-based DW techniques [65]. Significantly more research is necessary to improve the maturity of each technique before they can find their way into industrial applications.

Table 3-3 Comparison of features for different direct-write methods

DW techniques			Resolution	Viscosity ranges (Pa·s)/types	Writing speed	3D capability *
Droplet-based DW	Inkjet	Continuous	Droplet size 20μm-1mm, typically 150μm	<0.01	60mm^3/s	●●
		DoD	Droplet size 15μm - 200μm	<0.04	0.3mm^3/s	
	Aerosol Jet		Line width 10-150μm thickness 10nm-5μm	<2.5	0.25mm^3 /s single nozzle	●●●
Filament-based DW	MicroPen		50μm	<1,000	50mm/s	●●●
	nScrypt					
Tip-based DW	DPN		12nm line width and 5nm spatial resolution	Thiol molecules, macromolecules, nanoparticles	0.2-5μm/s	●
	tDPN		Line width 80nm	Those compatible with DPN and some meltable inks	–	
	NFP		Sub 50nm	Monomer, nanoparticles	0.4μm/s	
	E-DPN		30nm achieved	Soluble metal salts	10μm/s	
	PPL		90nm-hundredsof microns	Those compatible with DPN	–	
Energy Beam DW (Laser DW)	Solid precursor	LIFT	10-200μm	Metals, polymers	3-50mm/s	●●
		MAPLE	10μm-5mm, 10nm-1μm in thickness	Organic molecules	–	
	Gas precursor	LCVD	1-20μm	Metals, semiconductors and ceramics	50-200μm/s, up to 5mm/s	
	Liquid precursor	LEEP	2-12μm	Metals, ceramics	0.1-80μm/s	
		LAP	0.1-300μm	Metals	0.1-10μm/s	

* ● Poor 3D integration capability ●● Moderate 3D integration capability ●●● Good 3D integration capability

4 Experimental Setup and Characterisation Methods

This chapter presents an introduction to the Microfab Jetlab® 4 tabletop printing platform that was employed to jet solvent droplets in this project. Details of the waveform and droplet generation are given, particularly the droplet generation at low frequencies used for the inkjet via hole etching application. Other characterisation methods, including white light interferometry (WLI) microscopy and chromatic lateral aberration microscopy (CLA), which were used to measure the sizes of the via holes and polymer layer thicknesses, are also described.

4.1 The Microfab Jetlab® 4 Tabletop Printing Platform

4.1.1 Introduction to the Inkjet Printer

Jetlab® 4 belongs to Microfab's Jetlab® family and is a cost-effective research-based work station. The entire DoD printing system comprises the mechanical motion system, the computer control system, the manual control panel, and the dispensing device, as shown in Figure 4-1.

Positional control in the *x-y* plane can be achieved using a motor driven stage controlled by the supplied software, while the stand-off distance between the nozzle and the substrate in the z axis can be manipulated manually. The stage offers a printing area of 210 × 260mm and can be heated up to 250°C. A camera is incorporated into the system for visualisation of drop formation.

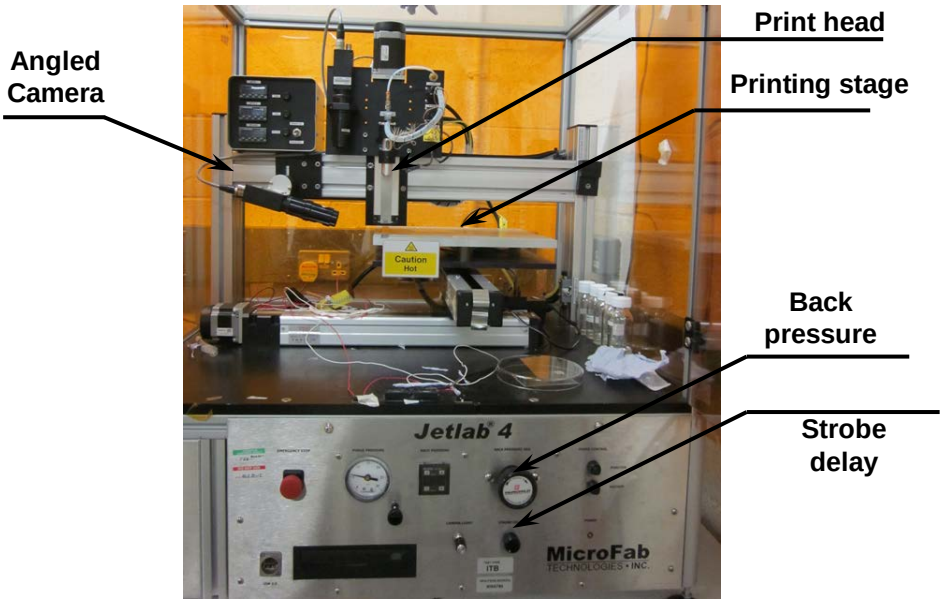

Figure 4-1 Microfab Jetlab® 4 inkjet printer

The most important component in the printing system is the print head assembly, which is used to store ink and dispense it onto a substrate. The print head assembly is composed of a print head and a micro-dispensing device. The print head is the holder for mounting the micro-dispensing device in place, which can also be detached from the printer. The micro-dispensing device comprises of a glass nozzle, a filter, electrical wires and a mechanical connection part, as shown in Figure 4-2. Both high temperature print head assemblies (e.g. PH-04a, temperature up to 240°C) and room temperature print head assemblies (e.g. PH-41H, temperature up to 50°C) are available, depending on the application requirements. High-temperature print head assemblies are useful for decreasing the viscosity of the ink to make jetting easier. The standard orifice diameter of the nozzle ranges from 20µm to 80µm with an interval of 5µm.

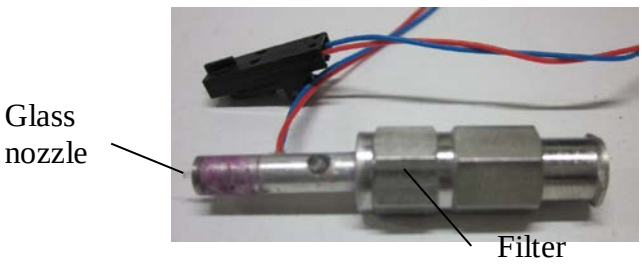

Figure 4-2 A photo of a Microfab micro-dispensing device

Patterns can be generated directly from Windows bitmap files. CAD formats such as GDS II and Gerber can also be translated into Jetlab® scripts for printing. Scripts can be written to tell the jetting device to jet dots and tracks in a pre-set pattern as well.

Table 4-1 Key parameters for the Microfab Jetlab® 4 printing platform motion system

Microfab Jetlab® 4	X stage travel	200mm
	Y stage travel	150mm
	Z stage travel	50mm
	X,Y encoder resolution	1.5µm
	Positioning accuracy	±30µm, unidirectional
	Positioning repeatability	±20µm
	X,Y stage travel speed	50mm/s
	X, Y stage acceleration	1500mm/s^2
	X, Y stage maximum payload	10kg
	Maximum print head payload	3kg

4.1.2 Script Compilation for Printing Patterns

Throughout the reported experiments in this thesis, comma-separated values (CSV) script files were compiled and loaded into the printer via the control software for firing a specific number of drops at a fixed location on the printing stage. A CSV file offers the flexibility to alter the number of drops dispensed or the location where to dispense. The first line of the script is a title line which gives a very general description of the script itself, but this line is not optional as the script will always run discarding the first line. Each line, excluding the first title line, must assume the same format as follows:

$$<x>, <y>, FLUID<i>, <drops>, <option>$$

where $<x>$, $<y>$ represent the x and y coordinates (in mm) respectively in the stage x-y plane. $FLUID<i>$ determines which fluid is dispensed if more than one type of ink is utilised for e.g. patterning different functional structures such as resistors, conductive tracks, semiconducting layers. Each ink should be designated a specific number for identification. In this experiment, only one ink is dispensed each time

through the nozzle, so the fluid identity number was always kept as 1. The <*drops*> value sets the exact number of drops jetted at each location and <*option*> is set to 0 so that the process will run continuously without suspending and asking for permission to continue before each dispensing event. The following is the script for printing a row of 23 via holes, as used in the experiments performed in section 5.1. Holes 1 to 20 are created using 1 to 20 drops respectively, while the remaining three holes are produced with 30, 40 and 50 drops. Printing in such a pattern allows detailed evaluation of the development of diameter versus the number of drops dispensed during the initial stages, while avoiding unnecessary repetition for larger numbers of drops.

Hole evolution
10,8,FLUID 1,1,0
11,8,FLUID 1,2,0
12,8,FLUID 1,3,0
13,8,FLUID 1,4,0
14,8,FLUID 1,5,0
15,8,FLUID 1,6,0
16,8,FLUID 1,7,0
17,8,FLUID 1,8,0
18,8,FLUID 1,9,0
19,8,FLUID 1,10,0
20,8,FLUID 1,11,0
21,8,FLUID 1,12,0
22,8,FLUID 1,13,0
23,8,FLUID 1,14,0
24,8,FLUID 1,15,0
25,8,FLUID 1,16,0
26,8,FLUID 1,17,0
27,8,FLUID 1,18,0
28,8,FLUID 1,19,0
29,8,FLUID 1,20,0
30,8,FLUID 1,30,0

31,8,FLUID 1,40,0

32,8,FLUID 1,50,0

4.1.3 Drop Analysis

Each pixel in a captured snapshot was calibrated to be 5.8μm, close to the 6.5μm/pixel reported for Jetlab 4 [117], which corresponds to a distance of 69μm between two adjacent tick marks on the screen. This can be used for a rough estimation of the droplet diameter. The droplet diameter can also be estimated using the ‘‘drop analysis’’ function via the Microfab control software. It uses Aphelion (from ADCIS/Amerinex Applied Imaging, Inc) to analyse the jetted drops. A region of interest (ROI) is defined within the field of view and filters are applied to identify the outline of the droplet. Then this geometric information is reported back to the Jetlab program in terms of number of pixels and the droplet diameter is estimated using the pixel calibration information in the system file.

An experiment was performed to obtain an estimate of the error for the drop analysis using ethylene glycol. Drop analysis was performed 8 times and the values are tabulated in Table 4-2. Four significant digits are quoted in the following table, as this is the data provided directly by the drop analysis function, although it is unclear what the actual resolution of this function is.

Table 4-2 Drop analysis performed by the Jetlab 4 inkjet printer

Analysis	1	2	3	4	5	6	7	8	Average
Drop diameter (μm)	78.59	77.99	78.99	78.19	78.58	77.99	78.78	78.39	78.44

In order to measure the actual drop volume and hence diameter, a script, demonstrated as follows, was compiled to dispense 10,000 drops into a bin at an ejection frequency of 1kHz. The maximum number of drops that can be dispensed at a single jetting is 999. Hence the script was written with the repeated lines.

Drop diameter estimation

-6,-8,FLUID 1,999,0

-6,-8,FLUID 1,999,0

-6,-8,FLUID 1,999,0
-6,-8,FLUID 1,999,0
-6,-8,FLUID 1,999,0
-6,-8,FLUID 1,999,0
-6,-8,FLUID 1,999,0
-6,-8,FLUID 1,999,0
-6,-8,FLUID 1,999,0
-6,-8,FLUID 1,999,0
-6,-8,FLUID 1,10,0

The mass of the collected solvent including the bin was obtained using a KERN ABC electronic balance (ABS 220-4, resolution 0.1mg). The mass of the bins were first weighed before the solvent collection. The evaporation time for an ethylene glycol sessile drop is much longer than 500s, while each measurement including solvent collection took less than 60s. Therefore the solvent loss due to evaporation during each measurement should be less than one drop. Calculation shows that this does not affect the final result significantly and can be considered negligible. The mass of the individual droplet can be calculated from dividing the total mass of the solvent by the number of drops dispensed. The actual average drop diameter can be calculated from the relationship between the volume (V) and its diameter (D_0): $V = \frac{1}{6}\pi {D_0}^3$. The results are listed in Table 4-3. The average single drop diameter is calculated to be approximately 75μm.

Table 4-3 Experimental and calculation results for the actual drop diameter

Dispensing	1	2	3	4	5	6	7	8
Bin mass (mg)	1621.2	1635.4	1629.3	1639.5	1627.5	1638.7	1642.4	1634.6
Solvent mass (excluding the bin) (mg)	2.4	2.4	2.6	2.4	2.6	2.4	2.3	2.5
Drop volume (nl)	0.22	0.22	0.23	0.22	0.23	0.22	0.21	0.23
Drop diameter (μm)	74	74	76	74	76	74	73	76

The discrepancy between these two estimation methods is (78.44-75)/75≈4.6%.

The more trusted method for drop diameter estimation is weighing a large number of droplets. The uncertainty in this weighing method can be estimated from the resolution of the weighing scale used and is of the order of 2%. The drop analysis in Jetlab 4 therefore appears to overestimate the drop diameter by 4.6±2%. This does not significantly affect the results or conclusions from this work.

4.1.4 Inkjet Printer Setup and Waveform Generation

It is important to find the appropriate waveform for the specific ink to be dispensed to ensure good droplet formation and good quality printing at initial printer set-up. Two types of waveform are most commonly used in Jetlab® 4: the bipolar waveform and the unipolar waveform, as shown in Figure 4-3.

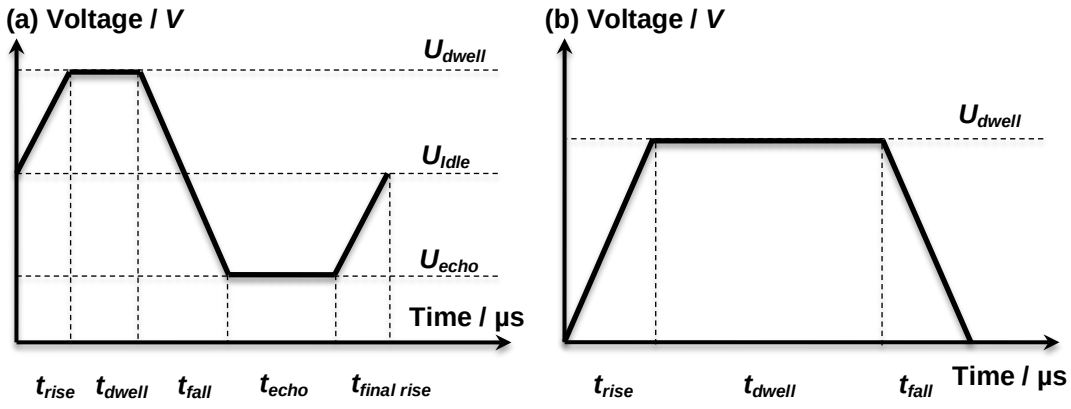

Figure 4-3 Waveforms used for droplet generation on a DoD inkjet printer (a) bipolar (b) unipolar

There are five time periods t_{rise}, t_{dwell}, t_{fall}, t_{echo}, $t_{final\ rise}$ and three voltage levels U_{dwell}, U_{idle}, U_{echo} that must be defined for a bipolar waveform, as illustrated in Figure 4-3 (a), whereas for a unipolar waveform, there are only a U_{dwell} voltage level and three time periods t_{rise}, t_{dwell}, t_{fall}, as shown in Figure 4-3 (b).

In addition to the parameters corresponding to the aforementioned waveform, the droplet ejection frequency *i.e.* the number of droplets jetted by the nozzle per second, is set through the main control software. This parameter should not affect droplet

behaviour, but only the time interval between two consecutive drops. Finally, an adjustable back pressure is applied to the ink reservoir to avoid ink dripping out between droplets and is usually kept to a negative value.

To quickly find a suitable waveform, a unipolar waveform instead of a bipolar waveform was usually applied throughout this work, which reduced the parameters requiring adjustment to t_{rise}, t_{dwell}, U_{dwell}, t_{fall}, as shown in Figure 4-3 (b). However t_{rise} and t_{fall} were usually kept to 3µs, as recommended by Microfab. Therefore the only parameters needing to be tuned are t_{dwell} and U_{dwell}. These parameters must be optimised so that the camera view shows a single solid dark spot against a light background without any satellite drops, as shown in Figure 4-4.

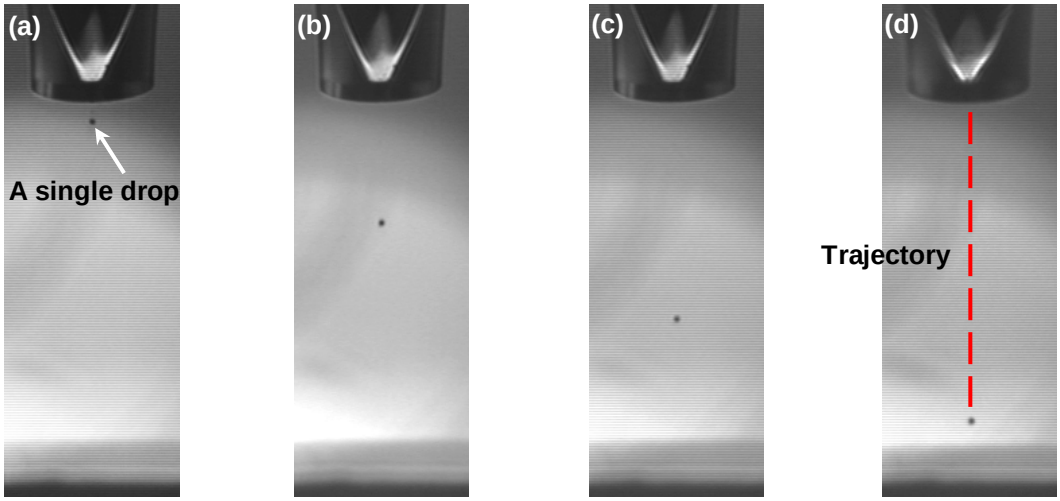

Figure 4-4 Images of ethanol droplets at different strobe delays (a) strobe delay=110µs (b) strobe delay=190µs (c) strobe delay=270µs (d) strobe delay=350µs. Ejection frequency = 500Hz, t_{dwell}=41µs and U_{dwell}=60V.

Images (a)-(d) in Figure 4-4 show an ideal ethanol droplet for the via hole etching application. The diameter and volume of the droplet were estimated to be 38µm and 29pl respectively. The trajectory of the generated droplet remains a straight line perpendicular to the substrate surface, as shown in Figure 4-4 (d). This ensures that a series of drops land at the same location on the polymer surface so that highly repeatable jetting can be achieved to ensure good quality hole formation. To further reduce the possibility of drop deviation, the nozzle should be brought as close as

possible to the substrate. Any build-up of a pendant drop on the nozzle was removed with cotton swabs to protect the principal drop from being disturbed.

4.1.5 Satellite Drops

Satellite drops are the tail behind the main drop that can occur when an excessive amount of solvent is jetted out of the inkjet nozzle during a jetting event. The tail thread can forward-merge into the main drop, or back-merge into one or several satellite drops, or become the ‘‘infinite satellites’’ which travel at the same speed as the main drop without merging [118]. It should be noted that a tail thread is acceptable during the breaking-up phase when the droplet detaches from the nozzle, as long as it is drawn back into the reservoir or merges into the main drop after the detachment, as illustrated in Figure 4-5 (b)-(c).

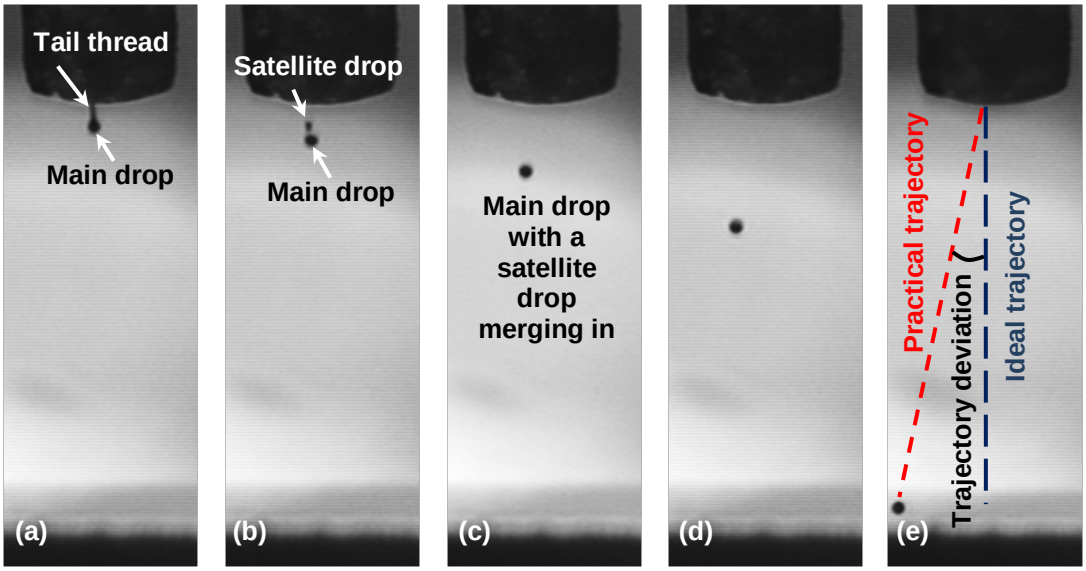

Figure 4-5 The process of a tail thread following a main drop splitting into an independent satellite drop and merging into the main drop afterwards (a) strobe delay=105 µs (b) strobe delay=136µs (c) strobe delay=207µs (d) strobe delay=332µs (e) strobe delay=1022µs. Ejection frequency = 500Hz, t_{dwell}=45µs and U_{dwell}=70V.

However, satellite drops which form in flight, as shown in Figure 4-6 (b)-(d), should be eliminated as they lead to poor via hole formation.

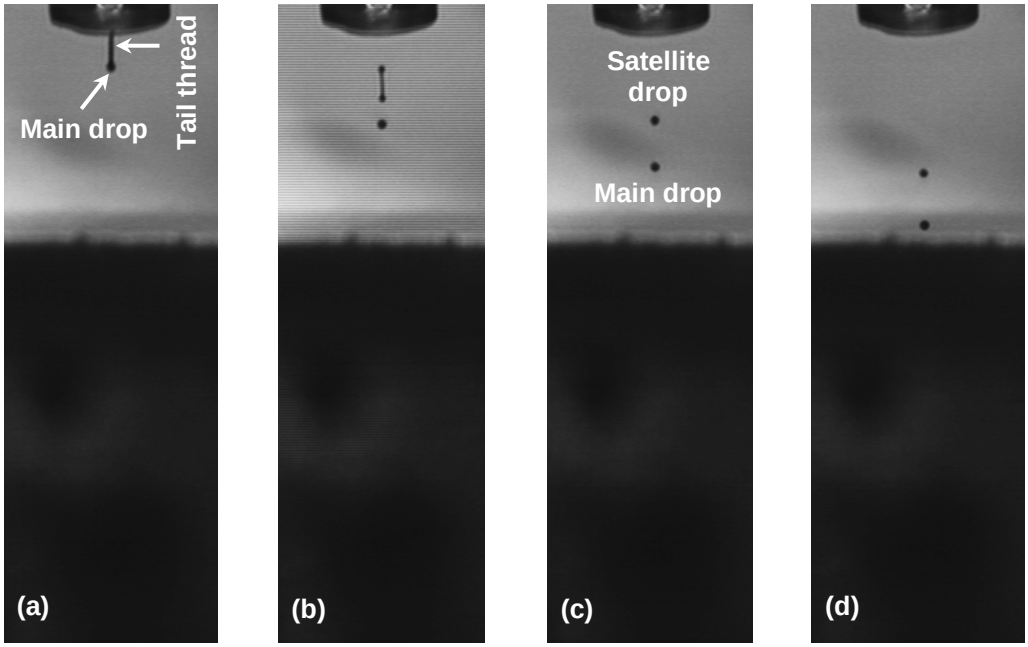

Figure 4-6 The process of a tail thread following a main drop evolving into an independent satellite drop (a) strobe delay=110μs (b) strobe delay=190μs (c) strobe delay=270μs (d) strobe delay=360μs. Ejection frequency = 500Hz, t_{dwell}=60μs and U_{dwell}=80V.

It has been suggested that the dimensionless number *Z*, the reciprocal of the Ohnesorge number (*Oh*) should be used to characterise drop formation and $Z > 2$ is required to achieve ejection without satellite drops [119]:

$$Z = \frac{1}{Oh} = \frac{Re}{\sqrt{We}} = \frac{\sqrt{\gamma \rho a}}{\eta} \qquad \textbf{(4-1)}$$

where $Re = \rho v a/\eta$, (the Reynolds number) is a dimensionless number measuring the relative importance of a fluid's inertial forces to viscous forces;

$We = \rho v^2 a/\gamma$, (the Weber number) is a dimensionless number measuring the relative importance of a fluid's inertial forces compared to its surface tension;

γ is surface tension (J/m^2);

ρ is density (kg/m^{-3});

a is the drop diameter (m);

η is the viscosity (Pa·s);

and v is the velocity (m/s).

This work has been extended further by Reis & Derby [120] and Jang [121] by giving a more confined Z range of $1<Z<10$ and $4<Z<14$ respectively. Therefore, an optimal range of $1<Z<14$ is assumed here, whereas Z is calculated to be 21-30 for a 30-60µm ethanol drop at a 0.5-2m/s impact velocity. Since the calculated Z range exceeds the reported upper limit of the optimal one, it can be expected that satellite drops would be observed rather than a single droplet due to its Newtonian behaviour [122,123]. However, stable inkjet printing beyond this Z range has been reported [124,125].

4.2 Characterisation Methods

4.2.1 White Light Interferometry (WLI)

A white light interferometry (WLI) microscope, as shown in Figure 4-7, is a non-contact surface measurement tool which provides numerical characterisation of surface structures. It uses a scanning white light source to image and measure the topography of surfaces.

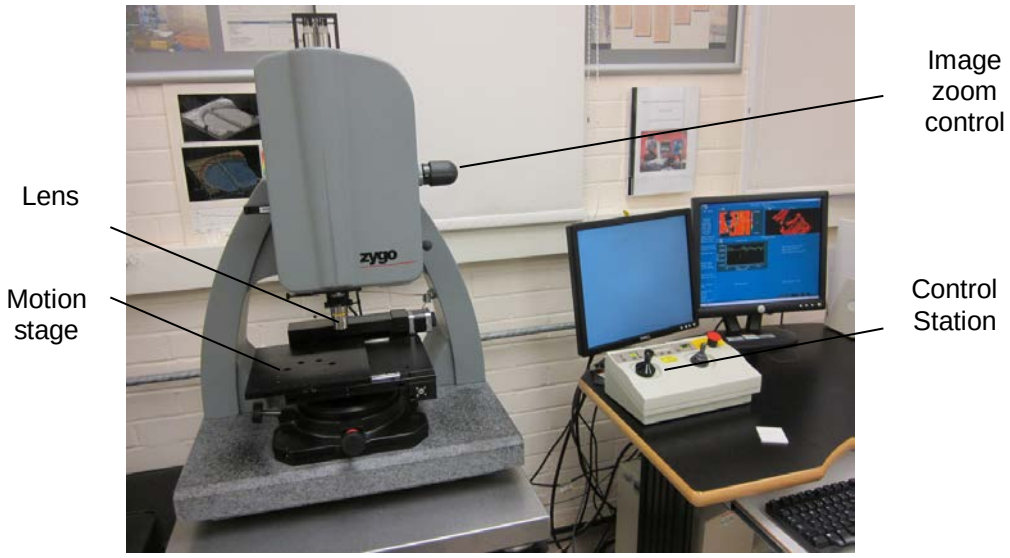

Figure 4-7 Zygo WLI scanning microscope

The light is split in the interferometric objective with one portion reflecting from the sample surface and the other reflecting from an internal reference surface in the objective, and then the light following these two paths recombines and enters a camera. These two portions of the light interfere with each other, resulting in fringes

that indicate the structure being imaged. These fringes are captured by the video system and converted into images by the incorporated software. Table 4-4 lists some of the specifications for the various objective options available.

Table 4-4 Nominal objective specifications at zoom 1× *

Objectives	System Magnification	Working Distance (mm)	Focus Depth (μm)	Lateral Resolution (μm)	Field of View (mm)	Max Slope (deg)
1×	20×	8.5	±322.5	11.8	7.0×5.3	1.41
2.5×	50×	10.3	±51.6	4.72	2.82×2.11	3.52
5×	100×	9.3	±17.2	2.72	1.41×1.06	6.08
10×	200×	7.4	±3.2	1.18	0.70×0.53	13.82
20×	400×	4.7	±1.8	0.88	0.35×0.26	18.15
50×	1000×	3.4	±1.0	0.64	0.14×0.11	24.27
100×	2000×	0.55	±0.5	0.45	0.07×0.053	33.25

*The working distance, focus depth, lateral resolution and max slope are the same at all zoom settings. Multipliers, which can be found in the manual, must be used for system magnification and field of view at other zoom settings. The 10× objective was used in this work and the FDA (frequency domain analysis) resolution is 3nm.

4.2.2 Chromatic Length Aberration (CLA)

A CLA confocal point gauge utilises the physical phenomenon known as chromatic aberration to measure the surface texture. In optics, chromatic aberration refers to the failure of a lens to focus all colours in the white light to the same convergence point and is caused by the different refractive indices of the lens for different light wavelengths.

Figure 4-8 schematically illustrates the working principle of a CLA gauge. White light indents from the light source into the lens and is converged to different points due to chromatic aberration. The height at a specific point is determined by the spectrometer integrated in the optical microscope sensing the chromatic dispersion of white light reflected from the surface. Figure 4-9 shows the Talysurf CLI 2000 equipped with a CLA 300 gauge used in this work. The resolution of the CLA gauge is 10nm.

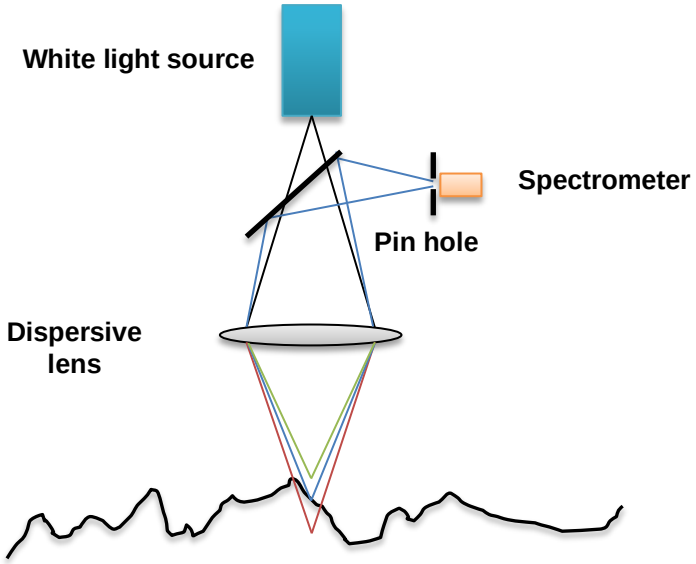

Figure 4-8 A schematic sketch of the working principle of the CLA gauge

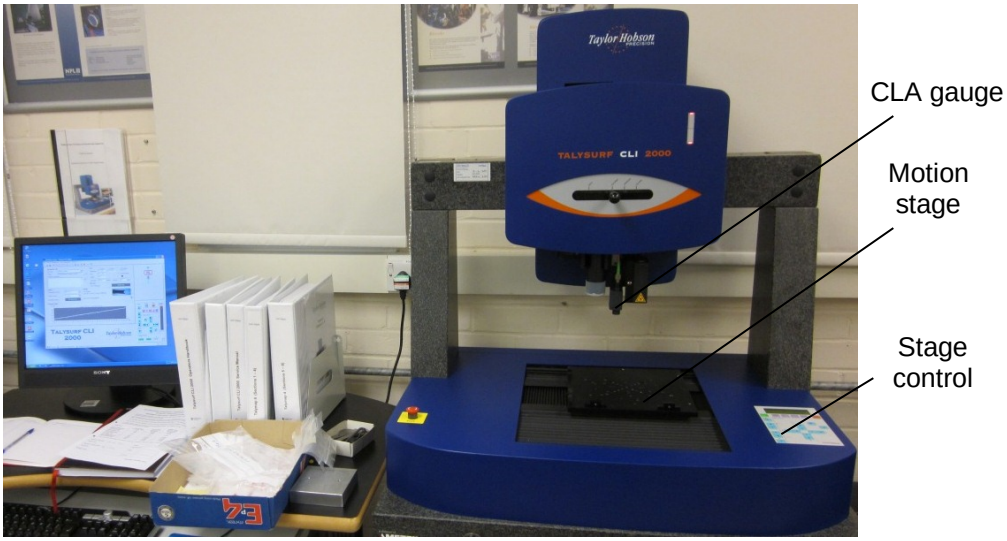

Figure 4-9 Talysurf CLI 2000 with a CLA gauge

4.3 Materials and Sample Preparation

The dielectric polymer used throughout this work was poly(4-vinyl phenol) (PVP) (molecular weight M_w=11,000, ≤0.2% *wt*.% monomer, density 1.16g/ml, glass transition temperature T_g 130-185°C, surface energy 43.9mJ/m^2, Sigma-Aldrich UK)

and its molecular structure is shown in Figure 4-10. Several solvents were used to dissolve or etch the polymer, including: ethanol (ethyl alcohol) (200 proof, anhydrous, ≥99.5%, Sigma-Aldrich UK), IPA (isopropyl alcohol) (Sigma-Aldrich UK), isobutanol (2-methyl-1-propanol) (anhydrous, 99.5%, Sigma-Aldrich UK) and ethylene glycol (Fisher BioReagents, Fisher Scientific UK). Acetone (CHROMASOLV®, for HPLC, ≥99.8%, Sigma-Aldrich UK) and Decon 90 (Fisher Scientific UK) were used for cleaning surfaces of the substrates.

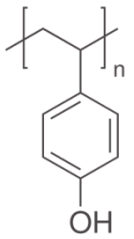

Figure 4-10 The molecular structure of poly(4-vinyl phenol)

The polymer was first dissolved into IPA (Isopropyl alcohol) in an ultrasonic bath to break up any agglomeration so that a clear yellow-coloured solution was formed. Standard 76mm×52mm glass microscopy slides were used as the substrates onto which a thin layer of the PVP solution was applied by spin coating. The glass slides were cleaned with Decon 90 detergent and acetone before spin coating. Sellotape was applied to cover 1cm of two edges of the slides before dispensing the solution on to the slide to facilitate the step measurement for characterising the film thickness. After spin coating, the tape was peeled off and the sample was left in air for 24hrs to dry up. Four profiles were taken for each sample using the Talysurf CLA gauge and the thickness of the polymer layer was calculated to be the average.

4.4 Summary

The Microfab Jetlab® 4 was briefly introduced in this chapter. Waveform generation was discussed and an example of ideal jetting was shown for the via hole etching application. Scripts used to define the printing pattern were described. Characterisation methods for the formed vias were introduced as well as their working principles.

5 Factors Determining the Dimensions of Inkjet-Etched Micro-Via Holes

The inkjet-etched via hole formation process is believed to be comprised of three sub-processes: droplet impact and spreading, polymer dissolution, and solvent evaporation. The timescale for solvent evaporation is much longer than for droplet impact and spreading and polymer dissolution, therefore solvent evaporation can have a great influence on the size of inkjet-etched via holes. This chapter mainly discusses the factors which affect the diameter of via holes produced. This includes droplet ejection frequency, droplet diameter, solvents, and substrate temperature.

5.1 The Effect of Droplet Ejection Frequency

5.1.1 Methodology

The concentration of the polymer solution used here was 11.3 *wt*.%. The spinning speed and time were 1500rpm and 30s respectively. The profiles were scanned and the polymer thickness was measured to be 1.27±0.05μm. The inkjet nozzle used hereafter had a diameter of 60μm unless specified otherwise. The jetting parameters were t_{rise}=t_{fall}=3μs, t_{dwell}=35μs and U_{dwell}=24V resulting in a droplet diameter of approximately 40μm, which equates to a droplet volume of 33pl. It is known that the droplet diameter is usually approximately the size of the nozzle diameter; however, it has been reported that jetting parameters can influence the diameter of the jetted droplet [126,127]. The smaller droplet diameter compared with the nozzle achieved here is attributed to the absence of satellite tails behind the main drop, which usually merge into the main drop and enlarge its volume. Different dispensing frequencies were used,

and 23 via holes were produced for each frequency. The printing pattern was achieved with the script as shown in section 4.1.2.

Figure 5-1 (a) schematically presents the typical profile of an inkjet-etched via hole in the polymer layer and the definition of its dimensions: outer diameter (D_{out}), inner diameter (D_{in}), ridge height (H_r) and via hole depth (H_d). Figure 5-1 (b) demonstrates the profile of a via hole with a secondary hole at the bottom. It should be noted that the aspect ratio of the hole (H_d:D_{in}) is significantly lower than implied by these sketches, typically being in the range of 0.003 to 0.032. For each via hole, four profiles are taken, as shown in Figure 5-2. Dimensions such as D_{out}, D_{in} and H_d for each via hole are calculated to be the average of the four profiles.

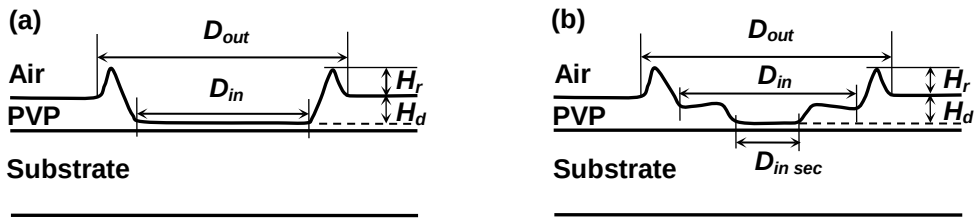

Figure 5-1 The profile of a (a) typical inkjet-etched via hole (b) via hole with a secondary hole at the bottom of the initial hole

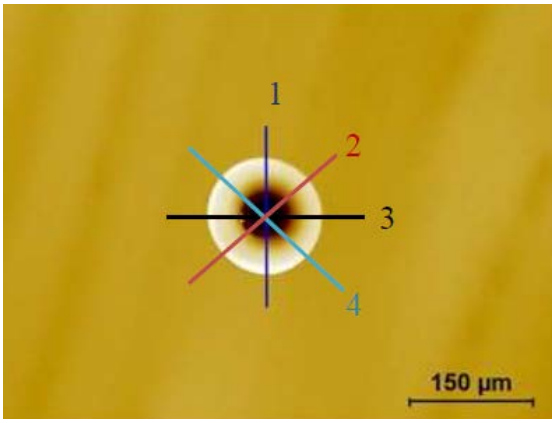

Figure 5-2 The profiles taken to calculate the average dimensions for each via hole

To estimate the uncertainty of the measurement process, a profile was taken across the via hole centre 8 times and the results were listed in Table 5-1. D_{out}, D_{in} and H_d were measured to be 107±1µm, 35.5±0.5µm, and 0.77±0.01µm respectively.

Table 5-1 D_{out}, D_{in} and H_d in different measurements

Measurement	D_{out} (μm)	D_{in} (μm)	H_d (μm)
1	106	36	0.76
2	107	35	0.77
3	106	35	0.77
4	107	36	0.78
5	108	35	0.76
6	108	36	0.77
7	107	36	0.77
8	108	35	0.77

5.1.1.1 Low Droplet Ejection Frequencies (f ≤5Hz)

Figure 5-3 presents optical microscopy images of via holes produced by different numbers of drops at a droplet ejection frequency of 1Hz. As can be observed from Figure 5-3, via holes produced by different numbers of ethanol drops are identical in size, despite some irregularity in shape. The irregularity of via holes becomes more prominent as the number of drops (N_d) increases, which is believed to be caused by the difficulty of jetting ethanol. It has already been demonstrated in section 4.1.5 that Z for ethanol is out of the optimal range for stable jetting. The formation of satellite drops and droplet trajectory deviation are believed to contribute to the deterioration of the via hole formation. It can also be observed from Figure 5-3 (b)-(f) that via holes created by dispensing multiple ethanol drops usually have more than one border ring compared with the hole created by a single drop, as shown in Figure 5-3 (a). This is thought to be caused by the first drop issue, reported by Dong [128], during which the first several drops dispensed by an inkjet nozzle vary in volume.

D_{out} and D_{in} of completed etched via holes produced at 1Hz were measured to be 123±2μm and 46±3μm respectively. H_d was measured to be 1.27±0.06μm, which is equivalent to the thickness of the polymer layer. It should be noted that D_{in} of the via hole produced by one single ethanol drop is larger than D_{in} of those produced by multiple drops. When only one ethanol drop was jetted onto the polymer layer, it only dissolved the polymer layer down to 0.34μm and the corresponding D_{in} was 63μm. A second droplet continued dissolving the hole to the depth of 0.94μm and the corresponding D_{in} shrank down to 45μm. Further removal of residual polymer at the

bottom by deeper etching with more ethanol drops induced no more prominent variation in H_d after several drops.

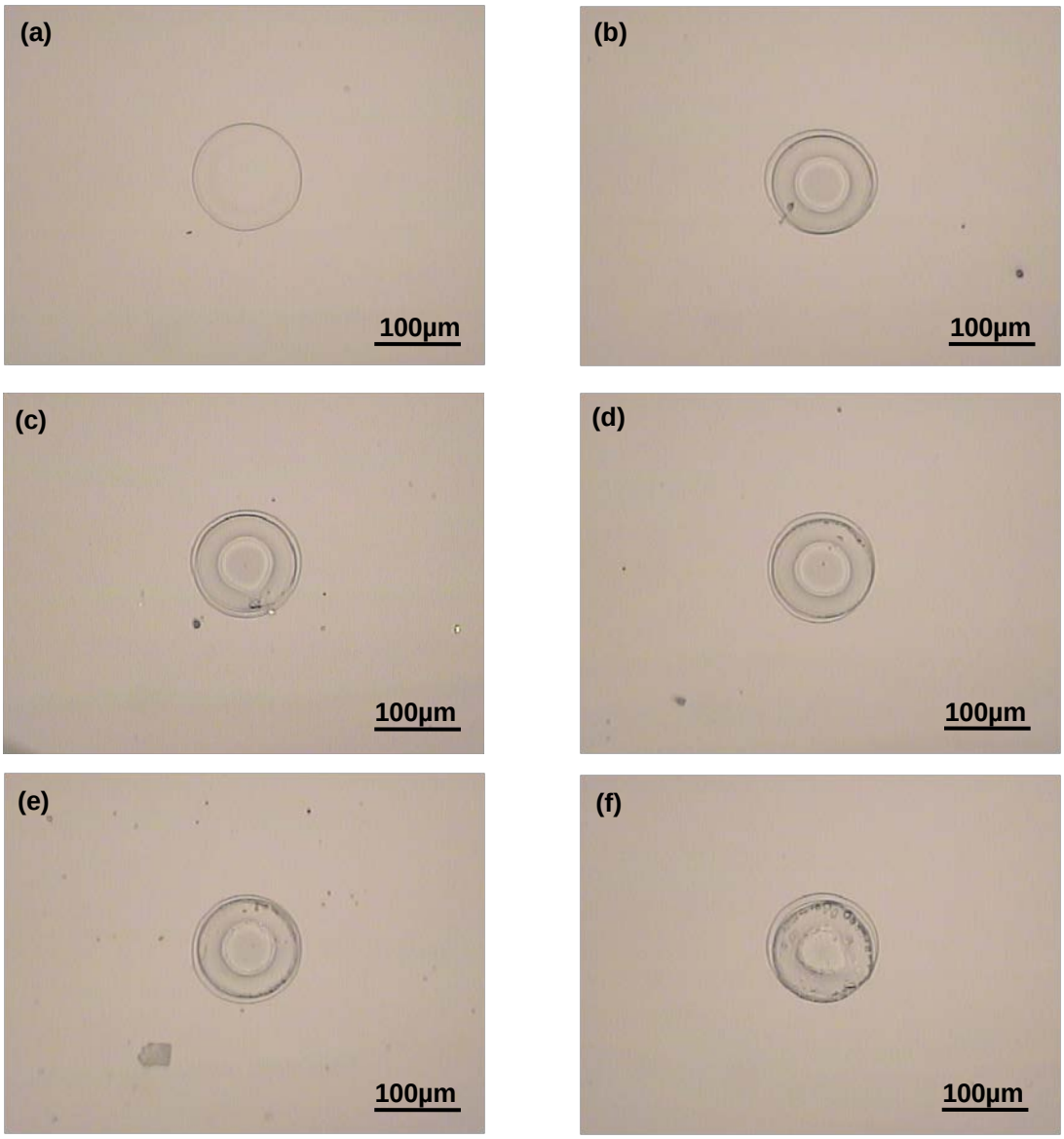

Figure 5-3 Optical microscopy images of via holes created at 1Hz by dispensing (a) 1 drop (b) 5 drops (c) 10 drops (d) 20 drops (e) 30 drops (f) 50 drops of ethanol

As for ejection frequencies of 2Hz and 5Hz, the development of D_{out}, D_{in} and H_d versus N_d, followed the same pattern as at 1Hz. D_{out} of the via holes produced at 2Hz and 5Hz were measured to be 123±2μm and 121±3μm respectively. H_d of the holes dissolved by multiple drops when residue could be considered completely removed

was 1.27±0.04μm and 1.23±0.03μm. Figure 5-4 and Figure 5-5 illustrate the evolution of D_{out}, D_{in} and H_d versus N_d at low frequencies.

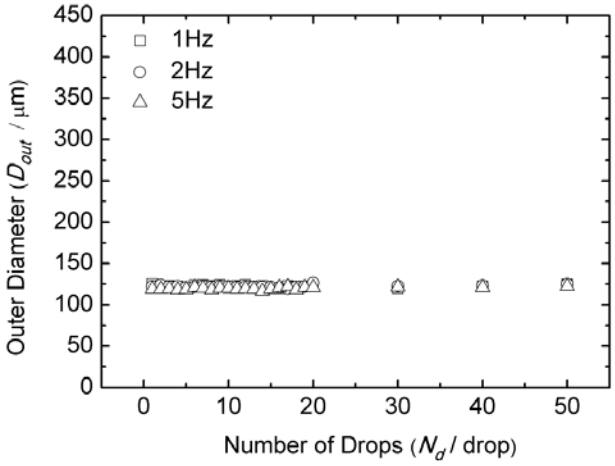

Figure 5-4 D_{out} versus N_d for via holes produced at droplet ejection frequencies of 1Hz, 2Hz and 5Hz

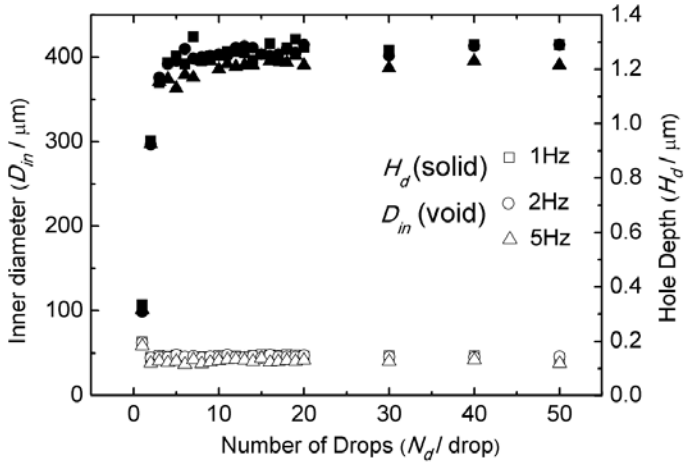

Figure 5-5 D_{in} and H_d versus N_d for via holes produced at droplet ejection frequencies of 1Hz, 2Hz and 5Hz

5.1.1.2 Medium Droplet Ejection Frequencies (*f*= 10Hz/20Hz)

Figure 5-6 presents optical microscopy images of via holes produced by various numbers of ethanol drops at an ejection frequency of 20Hz. As can be clearly seen

from these photos, instead of remaining the same, as occurred at low frequencies, the resulting via holes enlarged with increasing N_d. Figure 5-7 and Figure 5-8 illustrate the evolution of D_{out}, D_{in} and H_d versus N_d at 10Hz and 20Hz respectively.

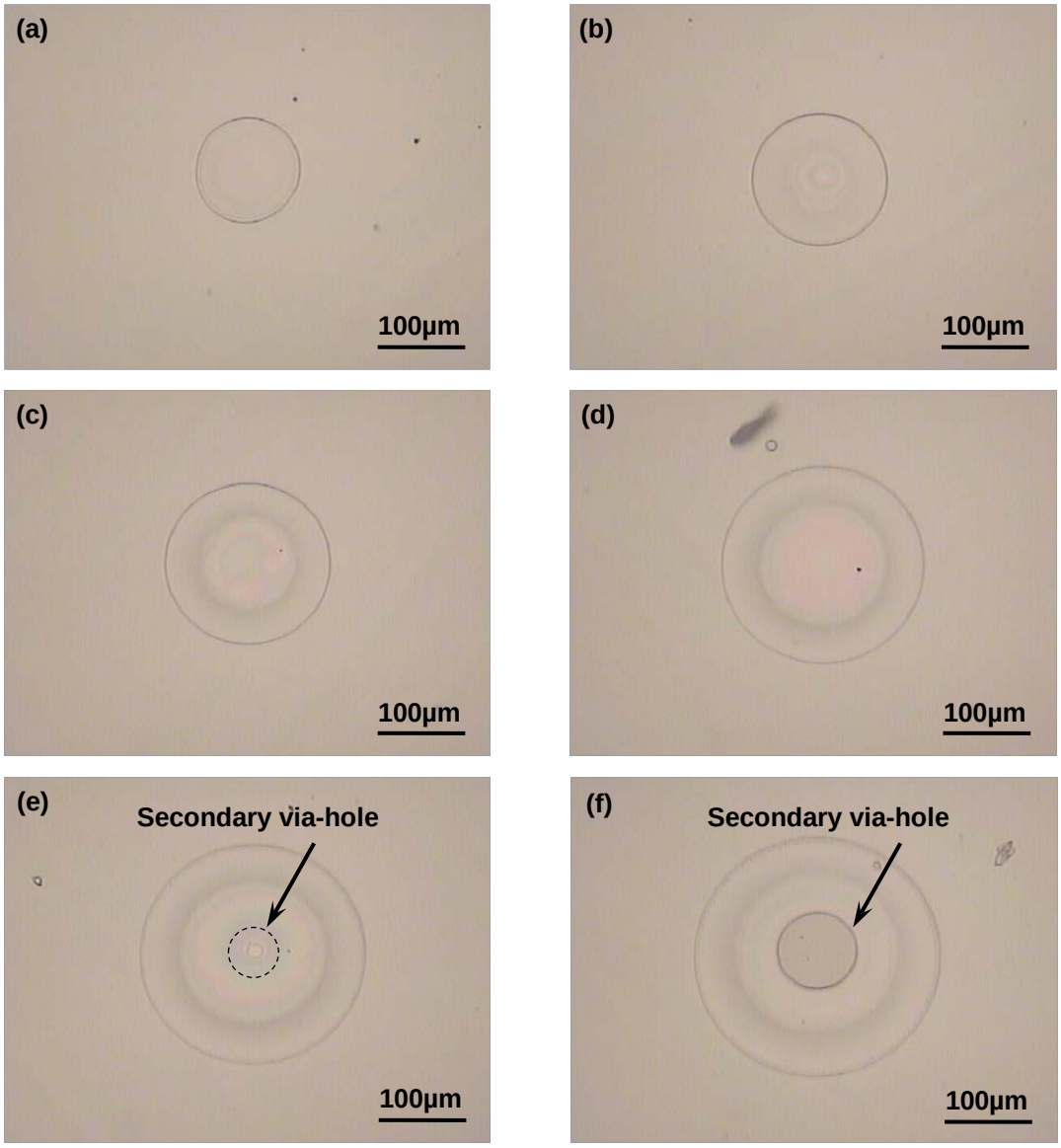

Figure 5-6 Optical microscopy images of via holes created at 20Hz by dispensing (a) 1 drop (b) 5 drops (c) 10 drops (d) 20 drops (e) 30 drops (f) 40 drops of ethanol

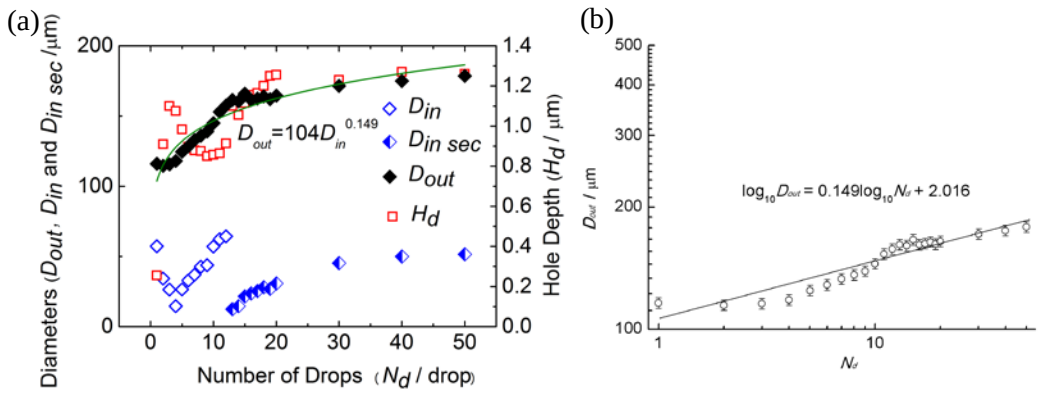

Figure 5-7 Effect of N_d for via holes produced at a droplet ejection frequency of 10Hz (a) D_{out}, D_{in}, $D_{in\ sec}$ and H_d versus N_d (b) D_{out} versus N_d on a logarithmic scale

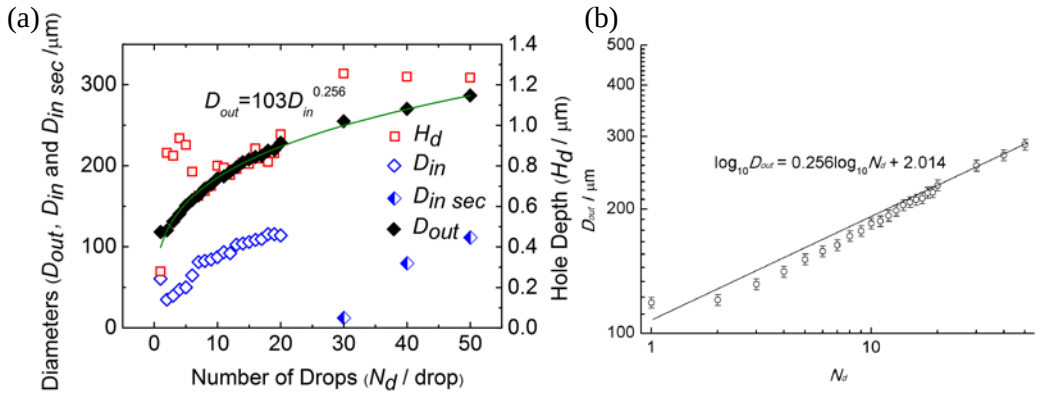

Figure 5-8 Effect of N_d for via holes produced at a droplet ejection frequency of 20Hz (a) D_{out}, D_{in}, $D_{in\ sec}$ and H_d versus N_d (b) D_{out} versus N_d on a logarithmic scale

D_{out} of the via holes formed at 10Hz and 20Hz, as shown by solid black diamonds in Figure 5-7 (a) and Figure 5-8 (a), follows a power law relationship with increasing N_d, with the exponents being 0.149 and 0.256, respectively. The reduction in drop mass during flight can be treated as negligible [129]. The volume of the sessile drop on the substrate (V_s) can be ideally treated equivalent to the sum of the volumes of the individual in-flight drops (V_0) if evaporation is neglected, which gives:

$$V_s = N_d V_0 \qquad \textbf{(5-1)}$$

The volume of the sessile drop can be estimated with that for a spherical cap, as sketched in Figure 5-9, to be [130]:

$$V_s = \frac{1}{3}\pi h^2(3R - h) = \frac{1}{6}\pi h(3a^2 + h^2) \quad \textbf{(5-2)}$$

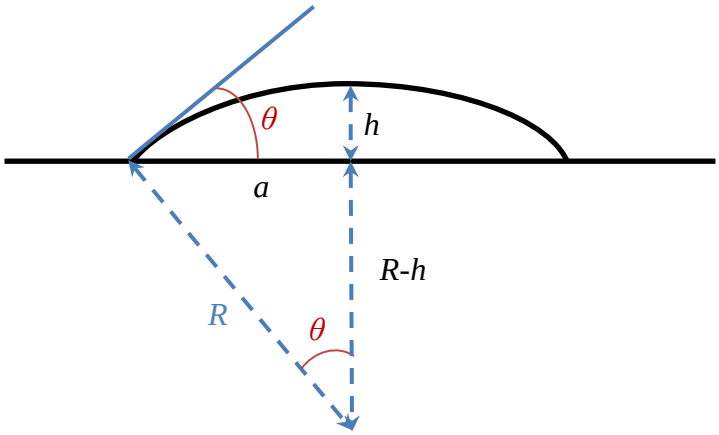

Figure 5-9 Geometry of a spherical cap and its dimensions

According to the geometry relations as sketched in Figure 5-9, the following relations can be deduced:

$$R = \frac{a}{\sin\theta}, h = R - \frac{a\cos\theta}{\sin\theta} \quad \textbf{(5-3)}$$

Substitution of the equations in (5-3) into (5-2) yields:

$$V_s = \frac{\pi a^3(1 - \cos\theta)^2(2 + \cos\theta)}{3\sin^3\theta} \quad \textbf{(5-4)}$$

Equation (5-4) can be rewritten by replacing a with $D_{out}/2$ into:

$$V_s = \frac{\pi {D_{out}}^3(1 - \cos\theta)^2(2 + \cos\theta)}{24\sin^3\theta} \quad \textbf{(5-5)}$$

Replacing the left term in (5-5) with (5-1) yields:

$$D_{out} = [\frac{24V_0\sin^3\theta}{\pi(1 - \cos\theta)^2(2 + \cos\theta)}]^{\frac{1}{3}} {N_d}^{\frac{1}{3}} \quad \textbf{(5-6)}$$

Equation (5-6) indicates that ideally D_{out} scales with N_d in a power law relationship with the exponent being 1/3, as reported by de Gans, *et al.*[8]. However, in

practice, the volume loss due to evaporation at the frequencies used in the experiments is assumed to be responsible for the deviation in these exponents from the theoretical value of 1/3. At such frequencies, D_{in} also increases with N_d, as illustrated by the unfilled diamonds in Figure 5-7 (a) and Figure 5-8 (a). A new via hole began to form at the bottom of the initial hole after several drops, which is referred to as a secondary via hole herein. The profile of a via hole with a secondary hole is shown in Figure 5-1 (b) and its development with N_d is represented by the half-filled diamonds in Figure 5-7 (a) and Figure 5-8 (b). Secondary via holes began to appear when at least 13 drops had been dispensed at 10Hz. However, at 20Hz such secondary via holes were not observed before 20 drops were dispensed, *i.e.* the appearance of secondary via holes is delayed by increasing the dispensing frequency. It can be noted from Figure 5-7 (a) and Figure 5-8 (b) that H_d is far below the thickness of the polymer before the appearance of the secondary via hole, which implies the presence of residual polymer at the bottom. With the formation of secondary via holes, H_d quickly approximates the thickness of the polymer layer.

It should be noted that during the dispensing process at medium droplet ejection frequencies, no satellite drops were observed following the main droplet. The droplet ejection frequency was adjusted back to 1Hz afterwards to fabricate via holes with different numbers of droplets. D_{out} remaining independent of N_d further confirmed that no satellite drops formed behind the main drop, which could have increased the dispensed solvent volume and enlarged the via holes produced. This is to exclude the possibility of secondary via holes being formed by satellite drops.

5.1.1.3 High Droplet Ejection Frequencies (*f*= 50Hz)

Figure 5-10 presents optical microscopy photos of via holes produced by various numbers of ethanol drops at 50Hz.

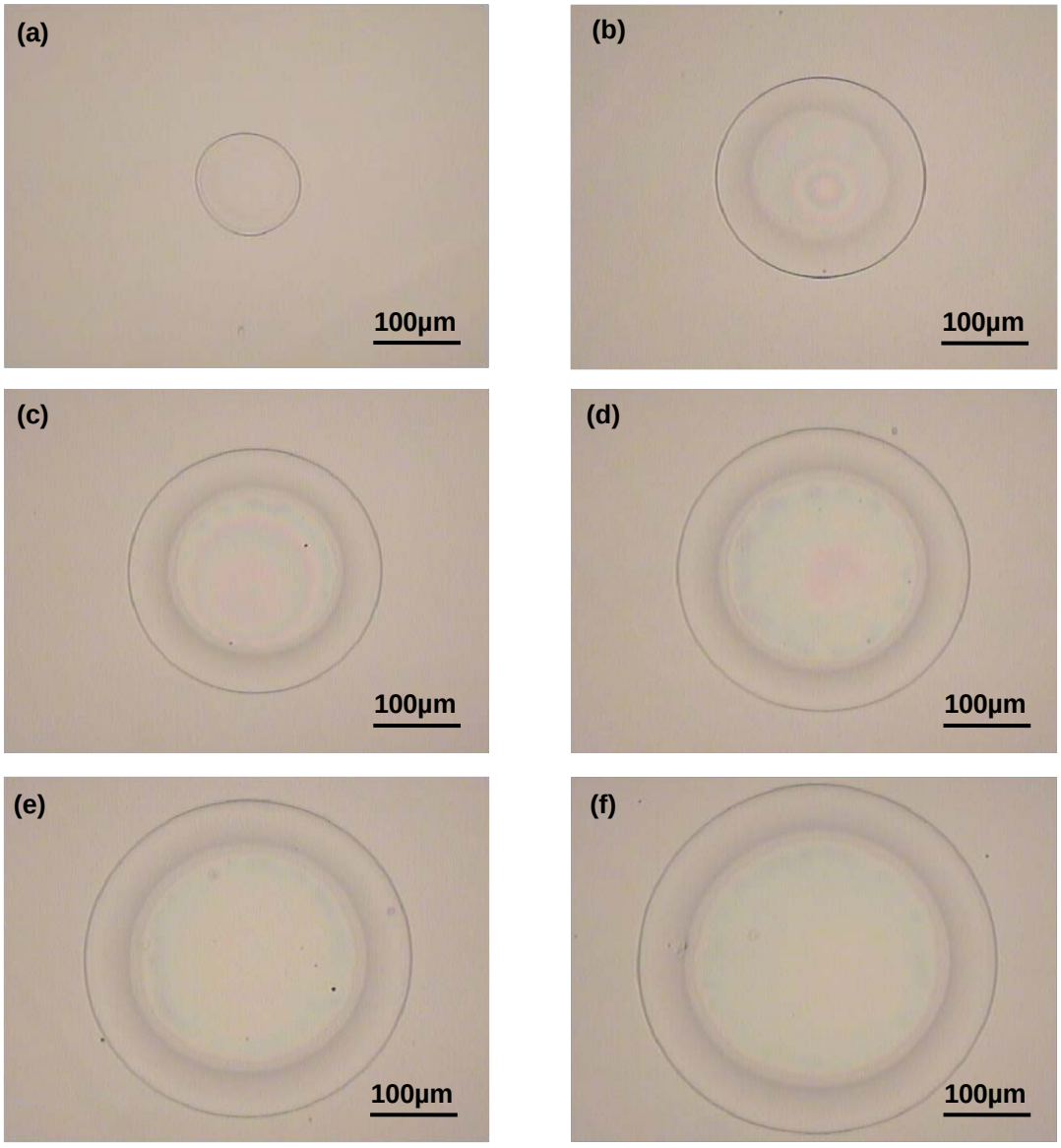

Figure 5-10 Optical microscopy images of via holes created at 50Hz by dispensing (a) 1 drop (b) 10 drops (c) 20 drops (d) 30 drops (e) 40 drops (f) 50 drops of ethanol

At a droplet ejection frequency of 50Hz, the size evolution with N_d resembles that at 10Hz and 20Hz, as shown in Figure 5-11 (a). D_{out} still follows a power law relationship with increasing N_d, with the exponent being 0.307, closer to the theoretical value of 1/3. D_{in} also increases with N_d. However, secondary holes were not found to develop within 50 drops at 50Hz. H_d is far below the thickness of the polymer, indicating incomplete penetration at this frequency.

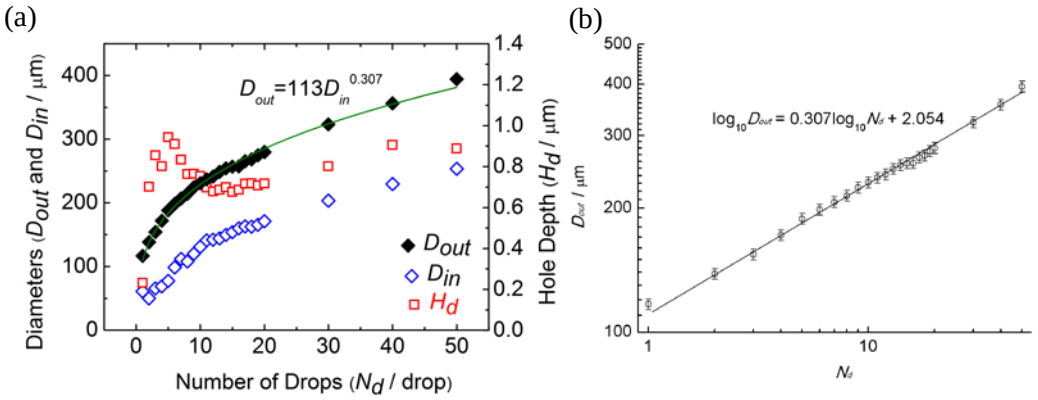

Figure 5-11 Effect of N_d for via holes produced at a droplet ejection frequency of 50Hz (a) D_{out}, D_{in}, $D_{in\,sec}$ and H_d versus N_d (b) D_{out} versus N_d on a logarithmic scale

5.1.2 Proposed Mechanism for the Effect of Drop Ejection Frequency

5.1.2.1 Coffee Stain Effect/Coffee Ring Effect

The coffee stain effect, also known as the coffee ring effect, exists as a commonly observed phenomenon, in which suspended coffee particles accumulate at the border of the sessile drop during water evaporation leaving a ring-shaped pattern eventually when the water completely evaporates into the ambient air [1,2,3]. Nonetheless, this phenomenon is not exclusive to coffee drops.

A sessile drop evaporating from a non-permeable substrate in a non-saturated gas has been investigated for many years. There are mainly two evaporating modes, known as constant contact angle mode and constant contact area mode. A constant contact angle mode is an evaporation process where the contact line recedes as the volume drops since the contact angle keeps constant, as sketched in Figure 5-12 (a). While a constant contact area mode is an evaporation process where the contact line is said to be pinned *i.e.* without movement and as the volume decreases the contact angle also decreases, as shown in Figure 5-12 (b). It has been observed by Deegan, *et al*. that the first mode is absent in coffee ring forming drops and the contact line dynamics changes due to the material dispersed in [3].

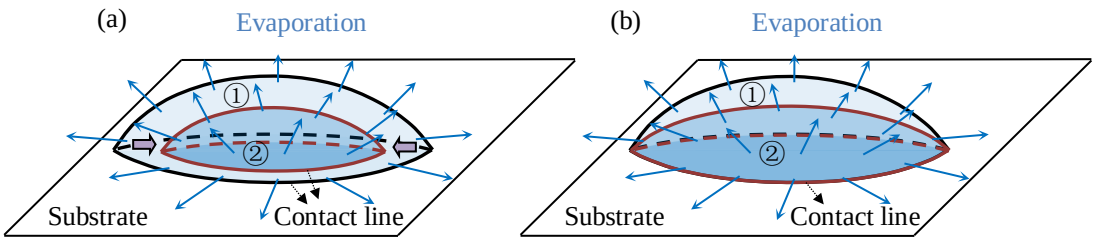

Figure 5-12 Schematic illustration of the two different sessile drop evaporation modes (a) constant contact angle mode (b) constant contact area mode

Generally contact line pinning in the coffee ring effect is believed to be due to the initial self-pinning caused by the roughness or chemical heterogeneity of the substrate and the strengthening of the pinning as material accumulates at the contact line, taking over as the primary pinning site [1,2]. During evaporation the surface of the sessile drop is cooled by the evaporation. The three phase contact line, on the other hand, is not subject to this condition due to the higher heat conductivity of the substrate than the surrounding atmosphere and stays close to the substrate temperature [131,132]. This higher temperature at the three phase contact line causes faster evaporation of the solvent at the periphery of the sessile drop. The evaporation at the border of a sessile drop is also expected to be faster because of the large dry substrate surrounding it, which is believed to provide faster vapour transport due to the more rapid fall in solvent concentration away from the surface [122]. The faster evaporation at the contact line than in the centre of the drop leads to a more rapid volume decrease at the droplet border. Since the contact area remains the same during evaporation, solvent is drawn from the central area to the border in order to replenish the volume loss to retain the pinning of the contact line. This solvent micro-flow within the sessile drop transfers more solute outwards to the border. With more solute being transferred and accumulated at the border during solvent evaporation and precipitating locally after evaporation of the solvent, the coffee ring pattern emerges when the sessile drop dries up. Deegans, *et al.* [3] used different types of solvents, solutes and substrates to demonstrate that the ring formation is insensitive to a wide range of experimental conditions such as temperature, humidity, pressure, gravity, electrostatic fields and surface tension. Two necessary conditions were defined: contact line pinning and

evaporation from the edge of the drop, and elimination of either will result in no ring formation.

5.1.2.2 Droplet Impacts on Surfaces

The impact of droplets on solid and liquid surfaces is a very diverse and complicated phenomenon depending on a lot of factors, such as impact velocity, liquid properties, surface tension and so on [133]. Based on the experimental conditions in this work, only droplet impacts on a thin liquid film and a solid dry surface are relevant. For inkjet printing, the Bond number, *Bo*, is used to characterise gravity related effects, and is usually small, implying that gravity related effects are negligible during droplet impact and spreading [122,133,134].

$$Bo = \rho g D^2/\sigma \qquad \textbf{(5-7)}$$

where D is the drop diameter (m);

ρ is the density of sessile drop (kg/m^3);

g is the gravitational acceleration (m/s^2);

and σ is kinematic viscosity (m^2/s).

5.1.2.2.1 Droplet Impacts on Solids

Drop impacts on dry solid surfaces have two possible outcomes in general: droplet deposition and droplet splash [135]. For the first outcome, a drop lands at low speed on the surface and a liquid film forms without phenomena such as splashing or jetting, known as a weak impact. For the second outcome, splashes with possible secondary drops are formed at high impact velocities. For highly energetic impacts, several other scenarios have been observed including prompt splash, corona splash, receding break-up, partial rebound and complete rebound with various drop impact morphologies as a result of different surface roughness, surface tension and wettability, and impact velocities [136]. Mundo, *et al*. derived a dimensionless term using *Oh* and *Re*, $K=Oh\cdot Re^{1.25}$, to correlate splashing and deposition and reported that $K>57.7$ results in splashing while $K<57.7$ leads to deposition [135]. K for the 30-60μm ethanol drops with impact velocities between 0.5-2m/s typically generated in this work is calculated to be in the range 0.009-0.49, *i.e.* much less than 57.7. Therefore,

the splashing scenario can be excluded here and the droplet impact is believed to follow a deposition process. The deposition outcome is believed to consist of four stages including the kinematic, spreading, relaxation and equilibrium phases [137]. In the kinematic phase, which usually lasts less than 1μs for a typical inkjet printing process [122], the dimensionless drop diameter increases with $t^{*0.5}$ (where $t^*=t(v/D)$ is the dimensionless time, v and D are impact velocity and initial drop diameter respectively), regardless of the physical properties of the liquid and the surface [137]. In the spreading phase, a lamella can be seen to be ejected from the drop base and a thin liquid film is formed. There is disagreement on whether the surface wettability is important during the initial stage of the spreading phase, but a consensus regarding its important role during the final stage of spreading has been reached [137,138,139]. During the spreading phase together with the kinematic phase, the contact line decelerates. The drop then may go through a post-spreading oscillation [133,134], which has a timescale of $\tau_{osc} = \sqrt{\rho a^3/\sigma}$ (where ρ is density, a is the drop radius, σ is surface tension) [134]. Based on the overview above, it is believed that when an ethanol drop lands on the poly(-4 vinyl phenol) surface, it quickly spreads out on the surface initially due to the impact velocity, then wets due to capillary effect as its kinetic energy is consumed by the increasing interface areas and dissipated by viscous forces until it reaches the maximum diameter. Therefore, in this work, the timescale for drop impact, *i.e.* the time for a drop to spread from the moment just before impact until when the maximum spreading is achieved, can be estimated by [139]:

$$t_c = \frac{8}{3}\left(\frac{D}{v_{impact}}\right) \quad \textbf{(5-8)}$$

where D is the drop diameter (m);

and v_{impact} is the impact velocity of the drop (m/s).

For a 30-60μm ethanol droplet with impact velocities of 1-3m/s, t_c is estimated with equation (5-8) to be 0.03-0.16ms. This calculation is in agreement with the timescale of the significant stages of a Ø40-50μm droplet impact and sessile drop formation, which is reported to be 0.1ms according to Dong, *et al.* [128].

5.1.2.2.2 Droplet Impacts on Liquids

Yarin and Weiss [140] studied the impact of successive monodisperse ethanol drops with diameters of 70-340μm on a solid surface at impact velocities up to 30m/s, which is close to the scale of the inkjet application in this work in terms of drop diameter and solvent choice. A thin liquid film was formed after the first drop impact, which is a similar situation to the experiments conducted here at higher frequencies. When a drop impacts on a thin liquid layer, two flow patterns on the surface can be expected: splashing and spreading. At high impact velocities, it has been observed that the thin film transforms into a crown-like shape with small droplets ejected [141,142]. No central jets, known as Worthington jets [143] and which are typically seen when the liquid film is replaced with a deep pool, have been observed for thin liquid films. Wang, *et al.* [141] gave an explanation of the absence of this central jet based on the impact energy transfer to the kinetic energy of the crown and a lack of cavity collapse because of the thin disk-like cavity. The droplet transforms into a thin liquid film in the shape of a lamella at low impact velocities. It is reported that the impact can be treated as a weak impact where surface tension is prominent when $We<40$ [133]. The Weber number of an ethanol drop in the diameter of 30-60μm at an impact velocity of 1-3m/s can be calculated to be 1-20, much less than 40. Therefore, the drop impact in this work can be treated as a weak impact and splashes are excluded.

5.1.2.3 Ethanol Drop Evaporation Time Estimation

The ethanol evaporation is estimated using an existing sessile drop evaporation model reported by Schönfeld, *et al.* [144]. The evaporation time is obtained for a single sessile drop to completely evaporate. The result is used in the explanation in the following section. These calculations were carried out for a substrate temperature of 20ºC.

An existing theoretical evaporation model for a sessile drop in still air with constant contact area is adopted here to estimate the evaporation time τ [144]:

$$\tau = V_0 \frac{\rho RT}{2\pi aDM(P_0 - P_\infty)} \cdot \frac{\sin(\theta_0/1.6)}{f(\theta_0/1.6)} \qquad \textbf{(5-9)}$$

where V_0 is the initial volume of the sessile drop (m^3);

ρ is the sessile drop density (kg/m^3);

R is the gas constant (J/mol·K);

T is the temperature (K);

a is the radius of the contact area (m);

D is the mass diffusion coefficient for vapour molecules in the gas phase (m^2/s);

M is the molar mass of the solvent (kg/mol);

P_0 is the saturation vapour pressure (Pa);

P_∞ is the ambient vapour pressure (Pa);

and θ_0 is the initial contact angle (rad).

f(θ) is given by the following two equations [144]:

$$f(\theta) = 0.00008957 + 0.6333\theta + 0.116\theta^2 - 0.08878\theta^3 + 0.01033\theta^4 \quad for\ \theta > 10^\circ \tag{5-10}$$

$$f(\theta) = 0.6366\theta + 0.09591\theta^2 - 0.06144\theta^3 \quad for\ \theta < 10^\circ \tag{5-11}$$

The mass diffusion coefficient *D* can be expressed as [145]:

$$D = \frac{0.00143T^{1.75}\sqrt{\frac{1}{M_1} + \frac{1}{M_2}}}{\sqrt{2}P[(\sum v_1)^{\frac{1}{3}} + (\sum v_2)^{\frac{1}{3}}]^2} \tag{5-12}$$

where M_1, M_2 are the molar masses of ethanol and air (g/mol);

P is the total pressure of the mixture (Pa);

and $\sum v_1$, $\sum v_2$ are group contribution values for the corresponding components determined by summing atomic diffusion volumes for each element in the molecule.

Taking ethanol for example, one ethanol molecule is composed of two carbon atoms, six hydrogen atoms and one oxygen atom. The diffusion volume for each individual atom are listed by Reid, *et al.* [145] and the group contribution value for ethanol in the ethanol/air system using this data is given by (5-13). The counterpart data for air used in (5-14) is also taken from Reid, *et al.* [145].

$$\sum v_{ethanol} = 15.9 \times 2 + 2.31 \times 6 + 6.11 = 51.77 \quad \textbf{(5-13)}$$

$$\sum v_{air} = 19.7 \quad \textbf{(5-14)}$$

$$\begin{aligned} D &= \frac{0.00143T^{1.75}\sqrt{\frac{1}{M_1}+\frac{1}{M_2}}}{\sqrt{2}P[(\sum v_1)^{\frac{1}{3}}+(\sum v_2)^{\frac{1}{3}}]^2} \\ &= \frac{0.00143 \times (293.15)^{1.75} \times \sqrt{\frac{1}{46.07}+\frac{1}{28.86}}}{\sqrt{2} \times 101325[(51.77)^{\frac{1}{3}}+(19.7)^{\frac{1}{3}}]^2} \\ &= 1.19 \times 10^{-6}\mathrm{m}^2/\mathrm{s} \end{aligned} \quad \textbf{(5-15)}$$

To estimate the timescale for sessile drop evaporation using equation (5-9), the initial contact angle of the solvent on the surface must be found. This can be calculated based on the model that the geometry of the sessile drop is presumed to be a spherical cap, as illustrated in Figure 5-9.

The volume for a spherical cap can be expressed as [130]:

$$V = \frac{\pi h}{6}(3a^2 + h^2) \quad \textbf{(5-16)}$$

Equation (5-16) above can be rewritten as a cubic equation of *h* as follows:

$$h^3 + 3a^2h - \frac{6V}{\pi} = 0 \quad \textbf{(5-17)}$$

The real solution to equation (5-17) can be expressed as:

$$h = \frac{3a^2}{\sqrt[3]{\left(\sqrt{\left(\frac{162V}{\pi}\right)^2 + 2916a^6} - \frac{162V}{\pi}\right)/2}} - \frac{\sqrt[3]{\left(\sqrt{\left(\frac{162V}{\pi}\right)^2 + 2916a^6} - \frac{162V}{\pi}\right)/2}}{3} \quad \textbf{(5-18)}$$

According to the Pythagorean theorem, we have:

$$a^2 + (R - h)^2 = R^2 \quad \textbf{(5-19)}$$

$$R = \frac{a^2 + h^2}{2h} \quad \textbf{(5-20)}$$

The contact angle can then be calculated as:

$$\theta = \arcsin\frac{a}{R} \quad \textbf{(5-21)}$$

For a Ø40μm ethanol droplet wetting the PVP surface with a diameter of 122μm, h can be calculated using equation (5-18) to be 5.7μm. R is, therefore, 329μm according to equation (5-20). The initial contact angle θ_0 is calculated to be 10.4°.

f(θ) for estimating the evaporation time is, therefore, defined by equation (5-10):

$$\begin{aligned} f(\theta) = {} & 0.00008957 + 0.6333 \times 0.187 + 0.116 \times 0.187^2 \\ & - 0.08878 \times 0.187^3 + 0.01033 \times 0.187^4 \\ & = 0.122 \end{aligned} \quad \textbf{(5-22)}$$

The evaporation time of a 40μm ethanol droplet wetting on the PVP surface into a sessile drop with a diameter of 122μm can be estimated as follows:

$$\begin{aligned} \tau &= V_0 \frac{\rho RT}{2\pi aDM(P_0 - P_\infty)} \cdot \frac{\sin(\theta_0/1.6)}{f(\theta_0/1.6)} \\ &= 3.35 \times 10^{-14} \\ &\times \frac{785.1 \times 8.314 \times 293.15}{2 \times 3.14 \times 6.1 \times 10^{-5} \times 1.19 \times 10^{-6} \times 0.046 \times 5950} \\ &\times \frac{\sin(0.187/1.6)}{0.122} \approx 0.5s \end{aligned} \quad \textbf{(5-23)}$$

5.1.2.4 Mechanism Discussion

The size evolution of the via holes throughout the etching process is attributed to the interrelationship between the volume of the sessile drop on the PVP layer and the

extent of its evaporation before another drop merges in, which will be discussed in more detail later in this section.

It has been shown that solvent first diffuses into the polymer during dissolution resulting in a swollen feature, which is then followed by the formation of intermediate layers between pure solvent and pure polymer, [146] as shown in Figure 5-13. Since the PVP layer in this experiment is very thin, it is assumed that chain disentanglement occurs immediately after solvent diffusion. The timescale of the polymer dissolution process can therefore be estimated to be similar to that of the solvent absorption into the polymer.

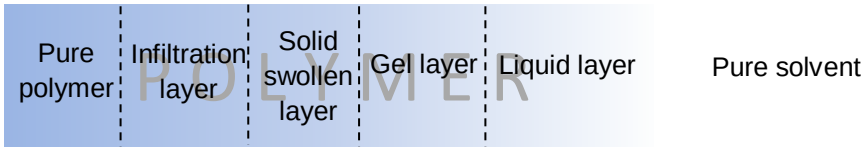

Figure 5-13 Illustration of different layers in polymer dissolved in a solvent. Separation between different layers is imaginary, and there is no marked border between layers in practice.

It has been reported by Desie, *et al.* [147] that absorption usually happens on the timescale of a few milliseconds. The timescale for drop spreading usually takes place on the order of 0.1ms, as discussed in section 5.1.2.2. The evaporation of an ethanol sessile drop has already been calculated to be 0.5s. Therefore the sequence of the timescale for these processes in ascending order is: droplet impact and spreading on the PVP layer to form a sessile drop; polymer dissolution into the sessile drop; and sessile drop evaporation into the ambient.

As schematically illustrated in Figure 5-14 (a)-(b), it is postulated that when a single ethanol droplet is jetted onto the PVP layer, it first impacts on the surface, and quickly wets and spreads to form a sessile drop covering an area within the diameter of φ. This is followed by the dissolution of the polymer into the ethanol drop, which is accompanied by simultaneous ethanol evaporation continuing beyond the completion of the polymer dissolution. The dissolved polymer is carried outwards away from the central area and subsequently re-deposited on the perimeter of the crater-like via hole due to the coffee ring effect, in which faster evaporation at the perimeter causes more

rapid volume loss at the periphery, thereby resulting in a compensating outward flow of material to maintain the sessile droplet shape. At low frequencies, *i.e.* no more than 5Hz, sufficient time is available for the preceding drop to evaporate substantially prior to the arrival of another drop. This is supported by the calculation of ethanol evaporation time in the last section. The time intervals between two consecutive drops are 1s, 0.5s and 0.2s respectively at 1Hz, 2Hz and 5Hz. For 1Hz and 2Hz, the time intervals between two drops are longer than or close to the droplet evaporation time, which is calculated to be 0.5s. This indicates that in theory complete or at least substantial evaporation of the previous sessile drop occurs before a new drop merges in. At a droplet ejection frequency of 5Hz, even though the time interval is less than the droplet evaporation time, the effect of the viscous force in the solution is believed to be sufficiently strong to prevent significant flow back to the centre. The process repeats itself from (c_1) to (e_1) for each droplet jetting, as shown in Figure 5-14. The contact line of the second sessile drop is believed to be pinned at the same location as for the preceding drop when the next droplet wets the polymer if the droplet diameter is constant. Therefore D_{out} remains constant. Dispensing more ethanol drops results in more polymer dissolution and re-deposition until the bottom is fully revealed, free of residual polymer. When the substrate at the bottom of the via hole is exposed, no more polymer is available to be transferred from the centre to the periphery of the via hole. Consequently D_{in} remains constant. Ideally, continuous dispensing of ethanol drops will not further enlarge the via hole in size once the polymer layer is completely penetrated and both D_{out} and D_{in} remain constant, as confirmed by the superimposition of hole profiles in Figure 5-15 and Figure 5-16.

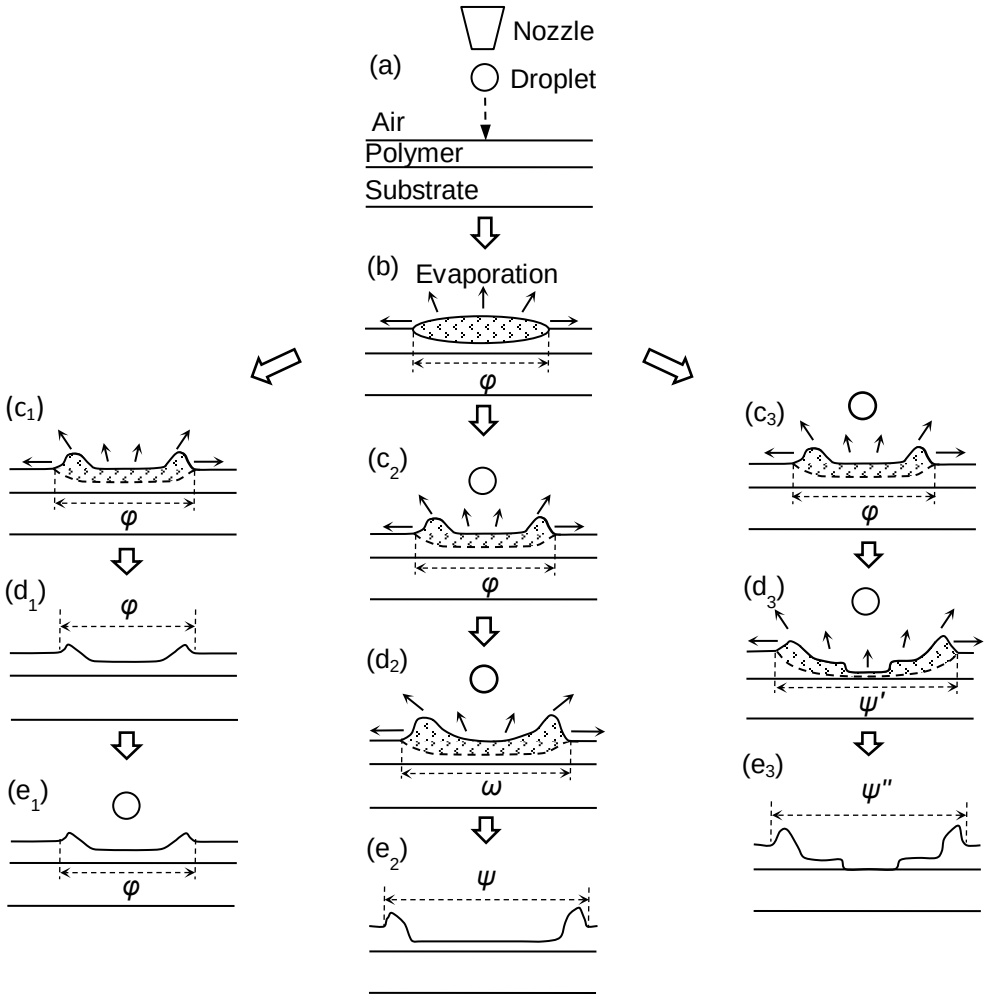

Figure 5-14 The process of via hole etching at different ejection frequencies: (a) Initial configuration; (b) After impact and spreading of the first drop; (c_1)-(e_1) The process of etching at frequencies sufficiently low for the preceding drop to evaporate before another drop impacts; (c_2)-(e_2) The process of etching at frequencies significantly above the threshold frequency featuring contact line enlargement and no secondary via hole; (c_3)-(e_3) The process of etching at frequencies higher than the threshold frequency featuring contact line enlargement and formation of a secondary via hole.

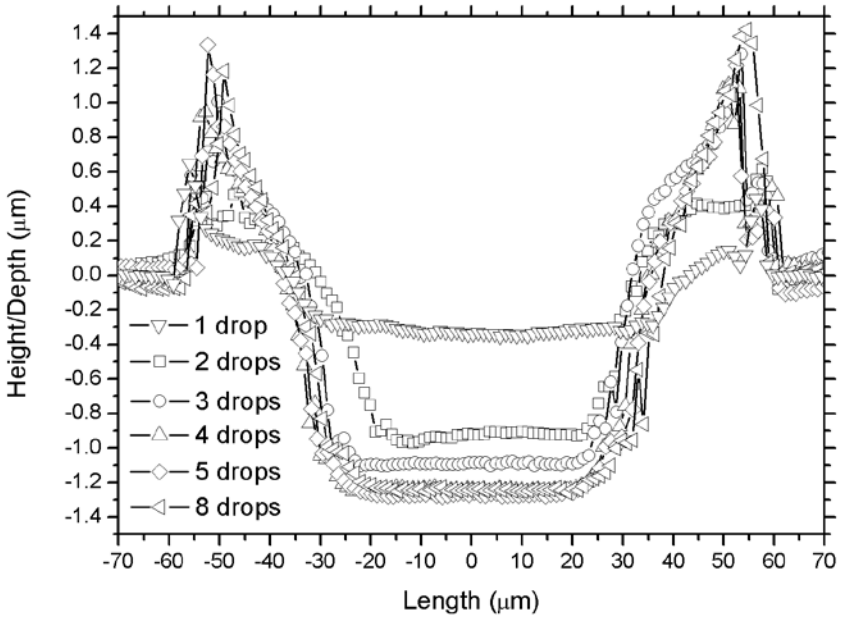

Figure 5-15 Superimposition of via hole profiles produced by 1-8 drops. Different holes show varying D_{in} and increasing H_d with increasing N_d

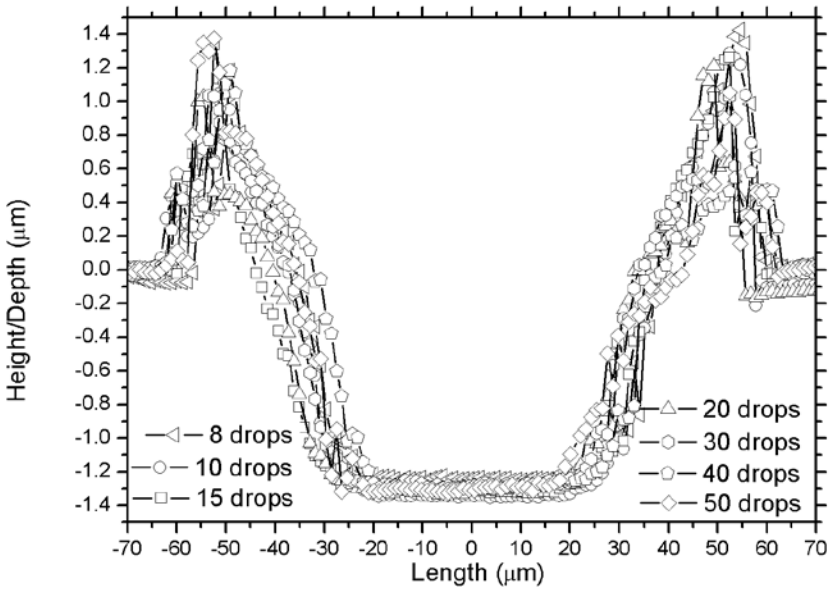

Figure 5-16 Superimposition of via hole profiles produced by 8-50 drops. Different holes show approximately equal D_{in} and H_d regardless of N_d

At an ejection frequency of 50Hz, the time interval between two consecutive drops (0.02s) is insufficient for the sessile drop to substantially evaporate (0.5s) before the next drop merges into it. Incomplete evaporation results in continuous volume expansion of the sessile drop due to the merging of multiple drops. The increasing quantity of solvent leads to further swelling, softening and dissolving of the polymer, and the contact line area becomes less and less viscous. This transforms the process from drops impacting a solid, as occurs at low ejection frequencies, to drops impacting a liquid. Accordingly, the contact line moves outwards, rather than being pinned locally, which consequently enlarges both D_{out} and D_{in}. Even though a drop can penetrate the shallow liquid film, the low viscosity of the liquid film allows it to flow back and recover after the collision. Therefore no secondary via hole is observed within 50 drops at 50Hz. This process is illustrated in Figure 5-14 (c_2)-(e_2). Nevertheless, due to a deeper penetration by subsequent ethanol drops, re-deposited polymer still leads to an initial D_{in} decrease. Then D_{in} starts to increase as a result of the dominating effect of contact line enlargement.

It is thought that the hole formation process can still be considered as drops impacting liquid at 10Hz and 20Hz. However, the viscosity of the liquid film can be expected to be higher than at 50Hz, due to less accumulation of incompletely evaporated solvent. It is believed that an appropriate impact velocity can provide sufficient kinetic energy transfer to counter the flowing-back of the viscous liquid. If the liquid film cannot then fully recover due to its relatively high viscosity, this will contribute to the formation of a secondary via hole, as illustrated in Figure 5-14 (c_3)-(e_3).

5.1.3 Threshold Frequency

Based on the experiments and analysis above, it can be concluded that a threshold dispensing frequency exists for an ethanol drop of a given volume under which no via hole enlargement will occur. This threshold frequency, f_c, is defined here as the droplet ejection frequency for a given droplet volume under which both D_{out} and D_{in} become constant once a sufficient number of droplets has been dispensed (assuming that the polymer layer is completely penetrated). An experiment was therefore performed to investigate f_c.

5.1.3.1 Experimental Preparation

For this experiment, a 7.8 *wt.*% polymer solution was used with the same spin coating parameters listed in section 5.1.1 to obtain a thinner layer of polymer approximately 0.77μm thick. The jetting parameters were set as t_{rise}=t_{fall}=3μs, t_{dwell}=45μs and U_{dwell}=55V here, and the resulting ethanol droplet diameter and volume were estimated to be 33μm and 19pl respectively. Since the size development of the via holes with increasing N_d has been demonstrated in section 5.1.1.1, only seven via holes were produced by 1, 2, 5, 7, 10, 12 and 15 drops, respectively for each frequency.

5.1.3.2 Threshold Frequency

Figure 5-17 shows no via hole enlargement for dispensing frequencies less than 16Hz, but D_{out} starts to increase as more drops are dispensed at 16Hz. As may be seen in Figure 5-18, H_d also decreases with N_d at 16Hz, which indicates incomplete penetration, *i.e.* f_c was found to be 15Hz. Even though D_{in} levels off to a constant value after dispensing of multiple droplets at ejection frequencies no more than 15Hz, D_{in} varies corresponding to the specific frequency used, as depicted in Figure 5-18. This variation is attributed to the liquid flowing back towards the centre.

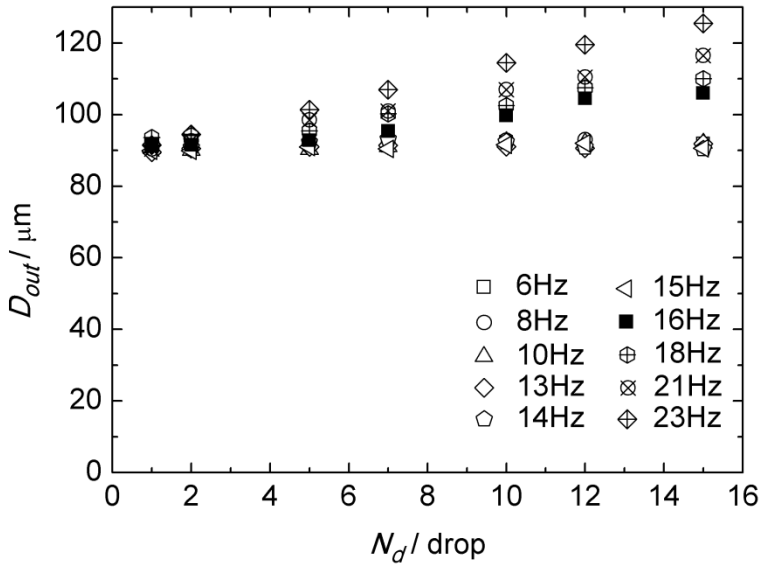

Figure 5-17 The profile of D_{out} versus N_d at different droplet ejection frequencies.

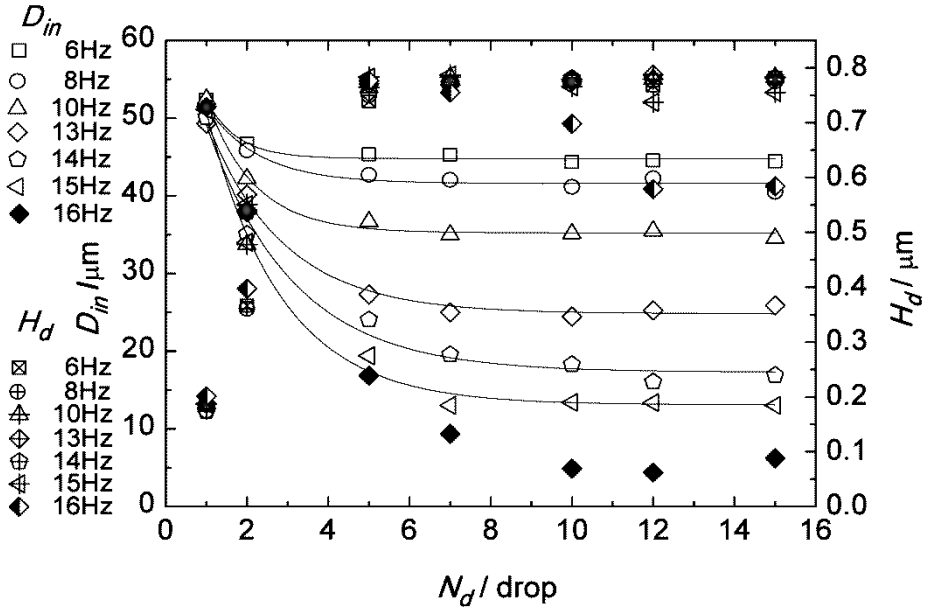

Figure 5-18 The profile of D_{in} and H_d versus N_d at different droplet ejection frequencies.

The evaporation time for the sessile drop on the PVP surface transforming from these 33μm in-flight ethanol drops was estimated using equation (5-9) to be 0.36s.

It is believed that the wetting of the sessile drop follows a constant contact area mode when the dispensing frequency is lower than f_c. Subsequent drops merge in without enlarging the contact area, due to the locally pinned contact line. This constant contact area mode contributes to D_{out} remaining constant, as illustrated in Figure 5-14 (c_1)-(e_1). At such dispensing frequencies, the time interval between two consecutive drops is more than 0.07s. The time is insufficient for each new drop to evaporate completely, but a considerable amount of solvent still evaporates within this time period. According to Hu and Larson [148], the net evaporation rate from the sessile drop is approximately constant with time for a small initial contact angle less than 40°, the amount of solvent loss for the sessile drop between two drop dispenses is, therefore, 0.07/0.36=19%. The excessive amount of solvent unable to evaporate allows some extra time for polymer to diffuse back to the centre caused by a concentration gradient. This inward micro-fluidic flow counters the outward flow caused by the coffee stain effect during solvent evaporation. However, the diffusion is believed to be limited as the viscous force is dominant. The net flow, therefore, is still

outward. Therefore the higher the dispensing frequency, the lower the viscosity of the sessile drop, and the further it can flow back into the bottom centre. This explains the different level-off values for D_{in} at different droplet ejection frequencies.

As the frequency rises above f_c, the time interval between two consecutive drops becomes even shorter (less than 0.07s). The accumulation of excessive solvent unable to evaporate becomes more prominent, which further decreases the viscosity of the polymer solution and facilitates polymer diffusion back to the centre. The reduced viscosity of the sessile drop and the kinetic energy transfer between the drop and the liquid film expand the contact line and increase D_{out}. The liquid can recover after impact, leading to a decrease in the via hole depth, as shown by the half-filled diamonds in Figure 5-18, which indicates incomplete penetration of the polymer.

5.2 Effect of Droplet Diameter

As discussed earlier, when a droplet lands on the surface, it quickly wets into a sessile drop covering an area. The larger the diameter of the in-flight droplet is, the more area it wets when transforming into a sessile drop on the substrate. Therefore it can be assumed that droplet diameter (D_0) can affect the size of the via hole produced. To test the effect of droplet volume on the dimensions of via holes created, IPA drops of various volumes were jetted with nozzles of different sizes and under different jetting parameters, as listed in Table 5-2. The diameters of the droplets jetted were estimated to be 29µm, 39µm, 48µm and 56µm respectively. Experiments were carried out on three samples with different PVP thicknesses. These different polymer thicknesses were achieved with solutions of different concentration and varied spin coating parameters, as listed in Table 5-3.

The droplet ejection frequency was set to 1Hz to ensure enough time was available for the previous sessile drop to evaporate substantially so that via holes would not enlarge with increasing N_d. As discussed above in section 5.1.1.1, D_{in} and D_{out} remain constant once no polymer residue is present at the bottom of via holes. For each droplet diameter, D_{out} and D_{in} were calculated as the average of those completely etched. In this case, via holes produced by 7 drops or more are used to calculate the average D_{out} and D_{in}.

Table 5-2 Jetting parameters and corresponding drop volume

Nozzle size (μm)	U_{dwell} (V)	t_{dwell} (μs)	Droplet diameter (D_0 / μm)	Droplet volume (V_0 / pl)
20	35	52	29	13
40	24	41	39	31
40	36	38	48	58
60	42	43	56	92

Table 5-3 Parameters for spin coating PVP films on glass substrates and the corresponding thickness of polymer

PVP concentration *wt*.%	Spin speed (rpm)	Spin time (s)	Polymer thickness (μm)
7.8	1500	30	0.78±0.05
11.3	1500	30	1.12±0.05
20.3	1500	40	2.61±0.04

Figure 5-19 illustrates the effect of droplet diameter on the size of via holes produced in polymer layers of different thicknesses. Since the volume of an in-flight drop and a sessile drop can be expressed as $V_0=\pi D_0^3/6$ and $V_s=\pi D_{out}^3(1-\cos\theta)^2(2+\cos\theta)/24\sin^3\theta$ respectively, it can be expected that $D_{out} \propto D_0$. By equating these two formulae, the following derivation can be obtained:

$$D_{out} = \sqrt[3]{4\sin^3\theta\,/[(1-cos\theta)^2(2+cos\theta)]}D_0 \qquad \textbf{(5-24)}$$

The proportionality can be expressed as $\sqrt[3]{4\sin^3\theta\,/[(1-cos\theta)^2(2+cos\theta)]} \approx 3.1$. D_{out} was found to fit a linear relationship with D_0 for each polymer thickness as expected. The equation was found to be $D_{out}=3D_0$, which is in close agreement with that predicted above. Since polymer thickness does not influence D_{out}, it is expected that D_{out} stays constant regardless of the polymer thickness, so long as D_0 remains unchanged. However, D_{in} does vary with polymer thickness and the thicker the polymer is, the smaller the D_{in}. As illustrated in Figure 5-19, with the same D_0, the corresponding D_{in} of the generated via hole is the smallest in the 2.61μm polymer layer and biggest in the 0.78μm polymer layer. This result is in good agreement with the explanation for the effect of polymer thickness on D_{out} and D_{in}. Linear regression to the data results in different intersections with the D_0 axis. The intersection refers to

a scenario that just the right amount of solvent is dispensed to completely etch through the polymer layer with the exposed bottom area decreasing to a point and D_{in} becoming zero. It seems reasonable to infer that this value should differ with the polymer thickness.

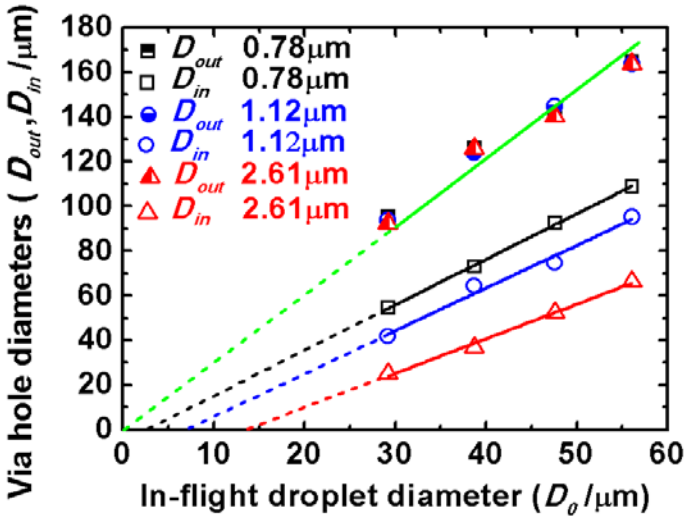

Figure 5-19 The profile of D_{out} and D_{in} of completely penetrated via holes versus the diameter of the in-flight droplet (D_0)

5.3 Effect of Solvent Used for Etching

The effect of solvent type on the dimensions of via holes created in PVP polymer was tested. Table 5-4 below lists some of their physical properties of various solvents.

Table 5-4 Main physical properties of the solvents at 20°C (at 1.01325kPa for boiling point)

Solvent (Linear formula)	Boiling point (°C)	Vapour pressure (Pa)	Surface tension (10^{-3}J/m^2)	Viscosity (mPa·s)
Ethanol (CH_3CH_2OH)	78	5950	22	1
Isobutanol ($(CH_3)_2CHCH_2OH$)	108	800	23	4
Ethylene glycol ($HOCH_2CH_2OH$)	197	16	47	16

The jetting parameters and resulting drop sizes for the solvents are listed in Table 5-5.

Table 5-5 Jetting parameters for different solvents and the corresponding drop size

Solvent	U_{dwell} (V)	t_{dwell} (μs)	D_0 (μm)	V_0 (pl)
Ethanol	35	24	40	33
Isobutanol	27	29	61	122
Ethylene glycol	45	31	57	99

It has already been shown in Figure 5-4 and Figure 5-5 that, for the etchant ethanol, once the entire polymer layer is penetrated, neither D_{out} nor D_{in} changes with further increases in the number of drops used to etch the holes at an ejection frequency of 1Hz.

5.3.1 Isobutanol (2-Methylpropyl Alcohol)

Figure 5-20 presents the evolution of D_{out} and D_{in} with N_d for isobutanol. As can be observed in Figure 5-20, D_{out} is independent of N_d while D_{in} varies with N_d.

It is believed that the slower evaporation rate of isobutanol contributes to this different evolution pattern of D_{out} and D_{in} with N_d. Isobutanol drops evaporate at such a rate that the accumulating solvent does not enlarge D_{out}, but does alter D_{in} with increasing N_d. During the first several drops, the flow of polymer solution back to the centre and deeper excavation in the polymer both contribute to a narrower D_{in}, as illustrated in Figure 5-21 (b). As N_d further increases, the accumulating residual solvent renders the polymer solution less viscous, so that it flows back to refill the hole, as shown in Figure 5-21 (c). This is shown by the rapid D_{in} increase and drop in H_d when N_d exceeds 7.

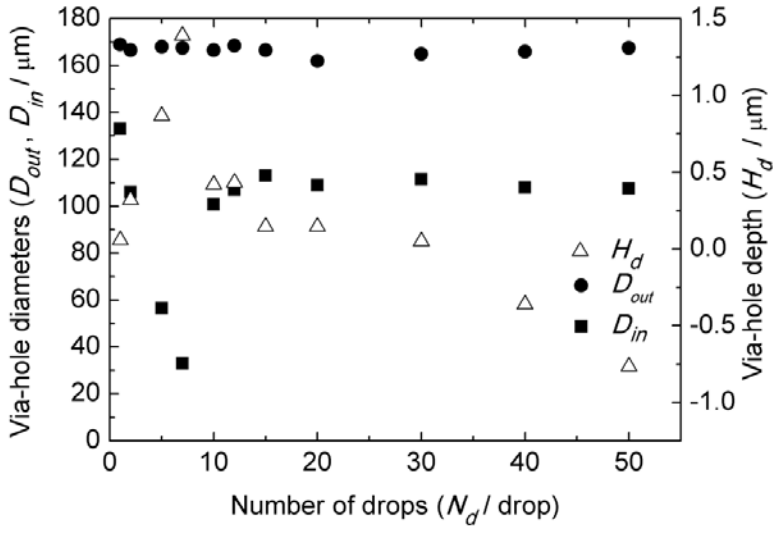

Figure 5-20 D_{out}, D_{in} and H_d versus N_d for via holes produced by isobutanol drops at intervals of 1s

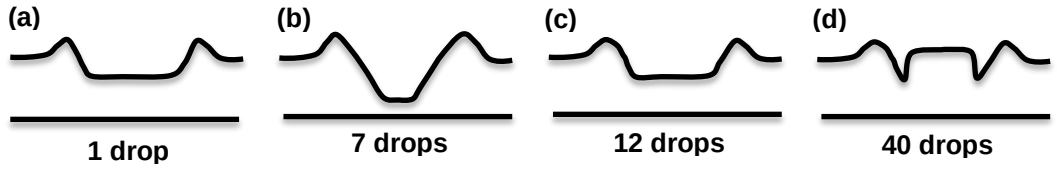

Figure 5-21 Illustration of via hole profile evolution with N_d using isobutanol

From N_d=30 drops, the bottom of the produced via holes starts to become protruded rather than depressed. The depth of hole becomes negative for holes produced by 40 and 50 isobutanol drops, as indicated by triangles in Figure 5-20. This can be observed more clearly from the 3D images of the via holes as presented in Figure 5-22 and Figure 5-23.

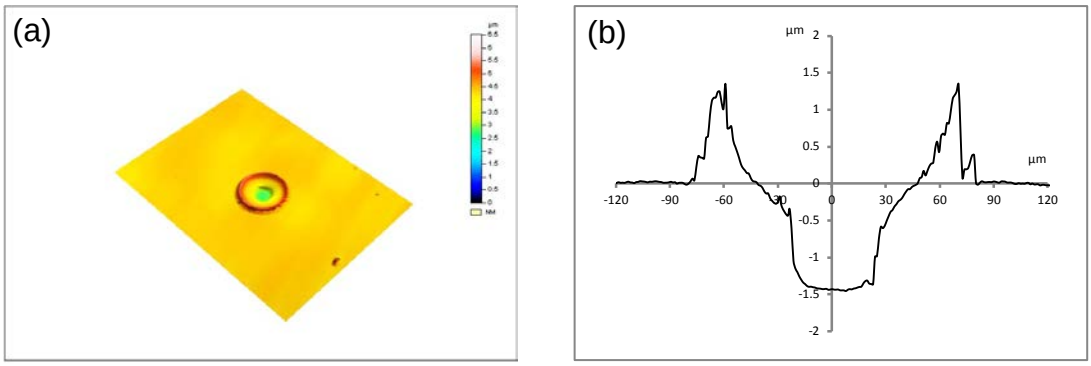

Figure 5-22 Views of a via hole created by 7 isobutanol drops (a) 3D (b) cross section

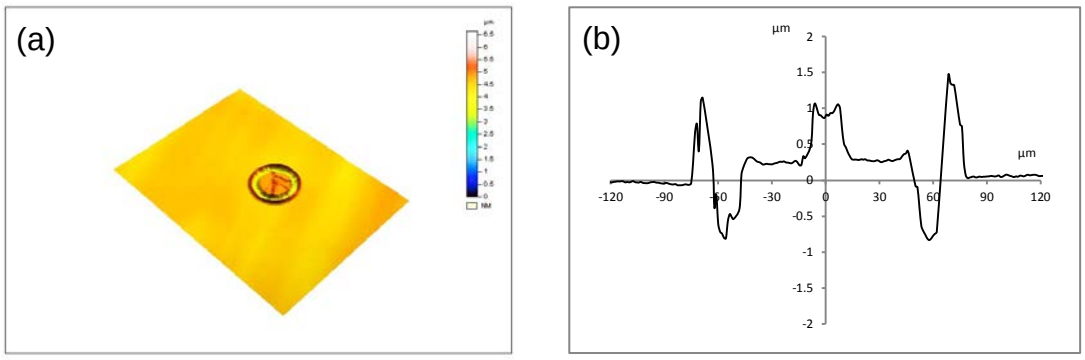

Figure 5-23 Views of a via hole created by 40 isobutanol drops (a) 3D (b) cross section

It is postulated that this protrusion formation is due to the Marangoni effect, which will be further discussed in chapter 7.

To provide further evidence for this feature evolution being due to the lower solvent evaporation rate, the same experiment was carried out again with a 90s delay between two consecutive droplets, giving 91s total time interval, which was intended to allow enough time for the preceding drop to fully evaporate before the next one. The jetting delay was achieved by calling subroutines in the main script. The subroutine script is similar to the one given in section 4.1.2 only with additional delay information. The main script and subroutine script were written in separate .txt files as shown below.

Main script

moveall 10 8 -93.5

repeat 1 "C:\jetlab\scripts\delay scripts\frequency subroutine 1.txt"
moveall 10 8 -93.5
repeat 2 "C:\jetlab\scripts\delay scripts\frequency subroutine 2.txt"
moveall 10 8 -93.5
repeat 5 "C:\jetlab\scripts\delay scripts\frequency subroutine 3.txt"
moveall 10 8 -93.5
repeat 7 "C:\jetlab\scripts\delay scripts\frequency subroutine 4.txt"
moveall 10 8 -93.5
repeat 10 "C:\jetlab\scripts\delay scripts\frequency subroutine 5.txt"
moveall 10 8 -93.5
repeat 12 "C:\jetlab\scripts\delay scripts\frequency subroutine 6.txt"
moveall 10 8 -93.5
repeat 15 "C:\jetlab\scripts\delay scripts\frequency subroutine 7.txt"
Subroutine script 5
begin
16 8 1 1 0
end
wait 90

Figure 5-24 schematically presents the evolution of D_{out}, D_{in} and H_d with N_d for the 91s printing delay. This evolution resembles that of when ethanol was used with a 1s delay, as shown in Figure 5-4 and Figure 5-5. D_{out} stays constant throughout the process and D_{in} begins to level off to a constant value when the polymer is completely penetrated.

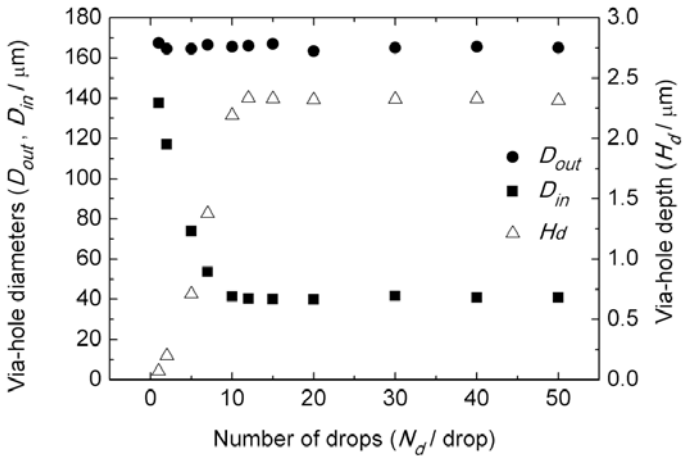

Figure 5-24 D_{out}, D_{in} and H_d versus N_d for via holes produced by isobutanol drops at intervals of 91s

5.3.2 Ethylene Glycol (1,2-Ethanediol Glycol)

From the results above, it could be predicted that jetting ethylene glycol at 1s intervals would cause the via holes to quickly enlarge with increasing N_d because of the significant amount of residual solvent left before the next drop merges in, due to its even higher boiling point and lower vapour pressure. Ideally, via holes produced by ethylene glycol could still be independent of N_d if sufficient time was allowed for the sessile drop to evaporate substantially before dispensing the next drop. However this encounters practical difficulties, as jetting becomes inconsistent in terms of satellite drop formation, drop trajectory deviation and drop volume fluctuation when the inkjet printer sits idle for so long. All these issues can contribute to poor quality via hole formation, since multiple droplets will not land at the same location and their contact lines may overlap. A higher temperature of 100°C was therefore applied to the printing stage to accelerate evaporation of the ethylene glycol.

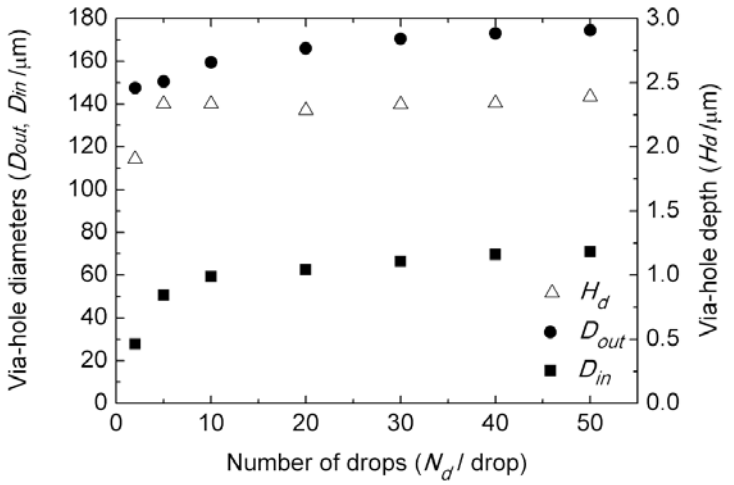

Figure 5-25 D_{out}, D_{in} and H_d versus N_d for via holes produced by ethylene glycol drops at intervals of 1s at 100°C

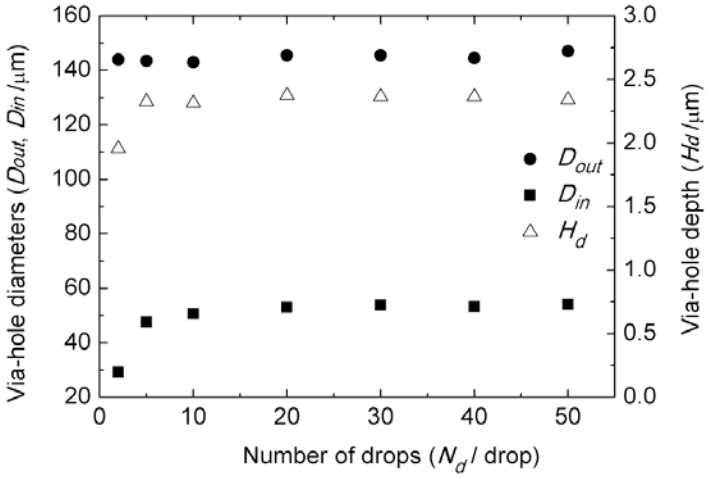

Figure 5-26 D_{out}, D_{in} and H_d versus N_d for via holes produced by ethylene glycol drops at intervals of 31s at 100°C

As illustrated in Figure 5-25, D_{out} and D_{in} still gradually increased with N_d at 100°C when the ejection frequency is set to 1Hz. However, it should be mentioned that even though the via holes are enlarged with increasing N_d, the depths of the holes equalled the polymer thickness, which indicates the holes are etched through the entire polymer layer. This can be potentially used for tuning the diameter of the via

holes produced without compromising penetration. When an extra jetting delay of 30s is applied, both D_{out} and D_{in} stay constant after 10 drops, as shown in Figure 5-26.

It has already been demonstrated that the time for ethanol drop evaporation is estimated to be 0.5s, which is less than the time interval of two consecutive dispenses in section 5.1.2.3. The same model can be used to estimate the evaporation time for isobutanol and ethylene glycol drops as well. The contact angle of an isobutanol drop is calculated to be 13.2º and the evaporation time for the isobutanol drop is estimated to be 6.1s. When an ejection frequency of 1Hz was used, the time interval between two consecutive drops is shorter than the time needed for evaporation, and a different development of D_{in} versus N_d was observed. However, when the jetting delay was set to 91s, which is sufficient for the previous drop to evaporate, the evolution resembles that for ethanol. For ethylene glycol, the evaporation time at room temperature is estimated to be 520s, and it is expected that the via holes would keep enlarging at a drop ejection frequency of 1Hz. A calculation was carried out using a model in the literature [149] to show that the drop diameter decreases less than 2% while travelling through the 3.5mm stand-off distance at 100ºC, so the diameter change during its travel from the nozzle to the substrate is negligible. The contact angle and evaporation time for the ethylene glycol drops were calculated to be 19.1º and 3.2s respectively. Therefore, the diameters were found to slowly increase with N_d for a 1s delay. When the delay was 31s, which is sufficient for the previous drop to fully evaporate, the evolution also resembles that for ethanol.

D_{out} remains unchanged regardless of N_d for isobutanol drops, even though the sessile drop evaporation time (6.1s) is longer than the time interval between two consecutive dispenses (1s), as shown in Figure 5-20. While for ethylene glycol, D_{out} slightly increases with N_d, as illustrated in Figure 5-25. This is postulated to be caused by the different viscous forces induced by different polymer solubility in these two solvents. The Hansen solubility parameters for each substance are listed in Table 5-6.

The solubility parameter distance (Ra) between two materials is defined as [150]:

$$(Ra)^2 = 4(\delta_{D2} - \delta_{D1})^2 + (\delta_{P2} - \delta_{P1})^2 + (\delta_{H2} - \delta_{H1})^2 \qquad \textbf{(5-25)}$$

where δ_D is the dispersion solubility parameter component ($MPa^{1/2}$);

δ_P is the polar solubility parameter component ($MPa^{1/2}$);

and δ_H is the hydrogen solubility parameter component ($MPa^{1/2}$).

Table 5-6 Hansen solubility parameters of PVP, isobutanol and ethylene glycol at 20°C [150,151,152]

Substance	Hansen Solubility Parameters			*Ra* ($MPa^{1/2}$)
	δ_D ($MPa^{1/2}$)	δ_P ($MPa^{1/2}$)	δ_H ($MPa^{1/2}$)	
PVP	17.6	10	13.7	-
Isobutanol	15.8	5.7	14.5	5.7
Ethylene glycol	17	11	26	12.4

Based on Table 5-6 and equation (5-25), the solubility parameter distance can be calculated for the PVP/isobutanol and PVP/ethylene glycol systems to be 5.7 and 12.4 respectively at 20°C. Raising the temperature for ethylene glycol to 100°C reduces its *Ra* to approximately 10, according to the calculation based on the equations given by Hansen [150].

This indicates that the solubility of PVP in ethylene glycol is much lower than in isobutanol. Therefore, the viscous effect is stronger in the PVP/isobutanol system than in PVP/ethylene glycol, resulting in the different D_{out} evolution with N_d.

5.3.3 Determination of D_{out}

It has already been mentioned in section 5.1.2.2 that the Bond number for droplets in inkjet printing is low and therefore gravity can be considered negligible. The Weber number (*We*), defined as $We=\rho v^2 D_0/\gamma$ (ρ is the fluid density, v is the drop velocity at impact, D_0 is the drop diameter, and γ is the surface tension), is a measure of the relative effect of the fluid's inertia versus its surface tension. The capillary number (*Ca*), defined as $Ca= \eta v/\gamma$ (η is the viscosity, v is the drop impact velocity, and γ is the surface tension), represents the relative effect of viscous forces versus surface tension. For all the solvents used in this work, the jetted drops have a Weber number range of 1-4, much less than the reported low Weber numbers between 20-30 [153,154]. The Ohnesorge number (*Oh*) is between 0.04-0.12. The corresponding capillary number is calculated to be 0.05-0.1. The wetting of drops on the substrate can be considered as impact-driven when $We>1$ [118,122,134]. The fluid can be treated as almost

inviscid when $Oh<1$ [118,122,134]. For a low *Ca* system, the surface tension is dominant over its viscous forces. Therefore most of the spreading is believed to occur in a short period of time where flow is driven by the dynamic pressure of impact and resisted primarily by inertia first and then by viscous effects in the final stage of spreading [134]. This has been previously shown to be the typical flow regime for inkjet printing [118].

The spreading factor (β), defined as the ratio of the maximum spreading diameter (D_{max}) on the substrate to the initial drop diameter (D_0), $\beta=D_{max}/D_0$, is known to be associated with the kinetic energy, viscous dissipation and surface energy of the droplet [155]. Pasandideh-Fard, *et al*. developed a model to estimate β using energy conservation [156]. Before impact, a droplet possesses kinetic energy KE_1 and surface energy SE_1. The droplet only maintains surface energy SE_2 and no kinetic energy at its maximum spreading diameter. The energy difference before and after the impact should be equal to the energy loss due to the work done to overcome the viscosity of the drop, according to the energy conservation condition. Based on the calculation, the outer diameter of the via holes is in agreement with the model proposed by Pasandideh-Fard, *et al.* [156], taking surface tension into consideration, as follows:

$$\beta = \frac{D_{max}}{D_0} = \sqrt{\frac{We + 12}{3(1 - cos\theta) + 4(We/\sqrt{Re})}} \quad \textbf{(5-26)}$$

Since the contact angle of the solvents, θ, is very low on the polymer, the contact angle is neglected here so as to reduce (5-26) into the following equation:

$$\beta = \frac{D_{max}}{D_0} = \sqrt{\frac{We + 12}{4(We/\sqrt{Re})}} \quad \textbf{(5-27)}$$

Therefore, the outer diameter can be estimated by:

$$D_{max} = \beta D_0 = D_0 \sqrt{\frac{We + 12}{4(We/\sqrt{Re})}} \quad \textbf{(5-28)}$$

The equilibrium contact diameter for a sessile drop wetting on the surface is assumed to be equal to D_{out} of the via hole. The estimation discrepancy between the predicted maximum wetting diameter (D_{max}) and the measured D_{out} is presented in Table 5-7. D_{max} based on Pasandideh-Fard's model overestimates D_{out}, and it is likely to be caused by contraction due to the capillary action.

Table 5-7 The estimation discrepancy between the predicted maximum wetting diameter (D_{max}) and the measured outer diameter (D_{out})

Solvent	β	D_0 (μm)	Predicted D_{max} (μm)	Measured D_{out} (μm)	Estimation discrepancy
Ethanol	3.35	40	134	123	9.0%
Isobutanol	3.04	61	185	165	12.2%
Ethylene Glycol	2.69	57	153	145	5.6%

The equation for estimating the maximum spreading diameter is insensitive to the contact angle (i.e. within 13% over an angle range of 0°-30° for all three solvents).

5.4 Effect of Substrate Temperature

It is known that solvent evaporation strongly depends on temperature. Therefore it was expected that adjusting the temperature of the substrate would change the size of the via holes produced. The effect of substrate temperature is therefore investigated in this section. The jetting parameters were set to U_{dwell}=55V, t_{dwell}=45μs and the corresponding droplet induced was estimated to be 56μm. The droplet ejection frequency was set to 1Hz.

It can be seen from Figure 5-27 that D_{out} for all stage temperatures is independent of N_d and remains constant during the etching process. The drop evaporates faster at higher temperatures, even before it touches the substrate surface, and the contact time between the drop and the substrate is shorter. Therefore, the drop is smaller when it is deposited, and D_{out} is also smaller.

As shown in Figure 5-28, D_{in} decreases first with increasing N_d and then levels off to a constant at 20°C, which is in agreement with the previous results without

substrate heating. However, the evolution of D_{in} versus N_d becomes different at higher temperatures. D_{in} first decreases with N_d and then increases before it eventually levels off to a constant, resembling a spoon-like cross section, as shown in Figure 5-28 at 40°C-80°C. This is postulated to be caused by the relationship between solvent evaporation and polymer re-deposition within the sessile drop.

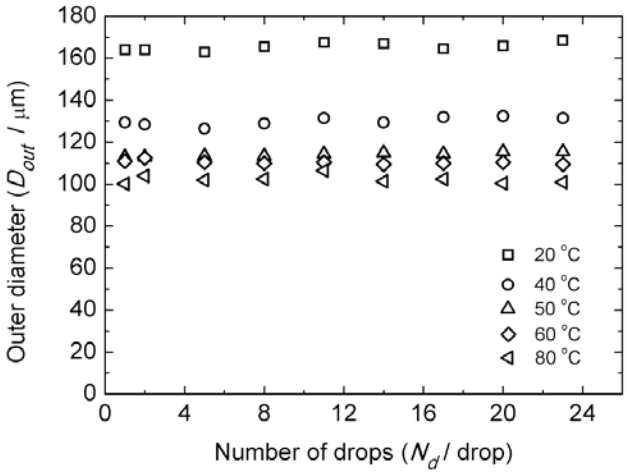

Figure 5-27 The profile of D_{out} versus N_d for ethanol drops at different stage temperatures.

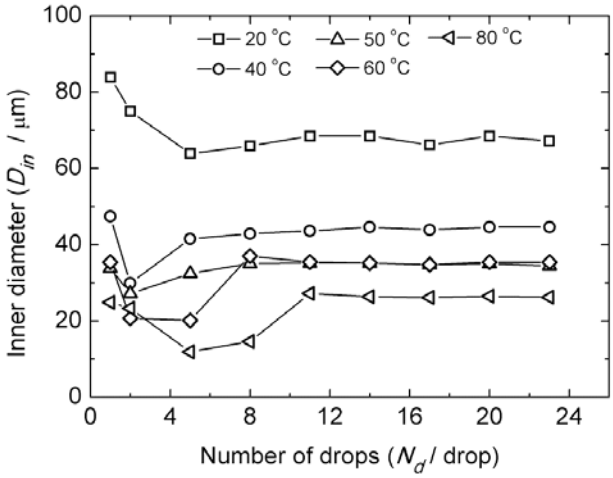

Figure 5-28 The profile of D_{in} versus N_d for ethanol drops at different stage temperatures.

When an elevated temperature is applied to the printing stage, there is a fast dissolution of the uppermost polymer layer and thus the coffee ring effect is pronounced for the first drop. The timescale for the evaporation of the sessile drop

from the PVP surface is estimated to be 0.6s at 20ºC using equation (5-9). Therefore, it is believed that the sessile drop evaporates completely before the next drop merges in. With increasing numbers of drops, the polymer is increasingly softened and dissolved. However, since the evaporation is fast after each drop deposition at higher temperatures, even though more polymer is dissolved, it cannot be transported to the rim completely. Hence D_{in} decreases first with N_d resulting in the profile changing from the solid line to the dotted line, as illustrated in Figure 5-29 (a) and (b). When most of the polymer is removed from the centre with a further increasing of N_d, the polymer from the sidewalls starts being transported to the rim. Even though the ethanol sessile drop evaporates drastically at higher temperatures, D_{in} increases further due to a faster transport velocity closer to the contact line [5]. Therefore, the via hole profile evolves from the solid line to the dotted line, as sketched in Figure 5-29 (c). When the maximum distance is achieved, the final profile remains independent of N_d, as shown in Figure 5-28. The higher the temperature, the faster the evaporation compared to the dissolution. Thus, more drops are needed for the same resulting structure. This is clearly demonstrated in Figure 5-28 where the higher the temperature, the larger the ‘‘bowl’’ of the ‘‘spoon’’, and the shorter the ‘‘handle’’.

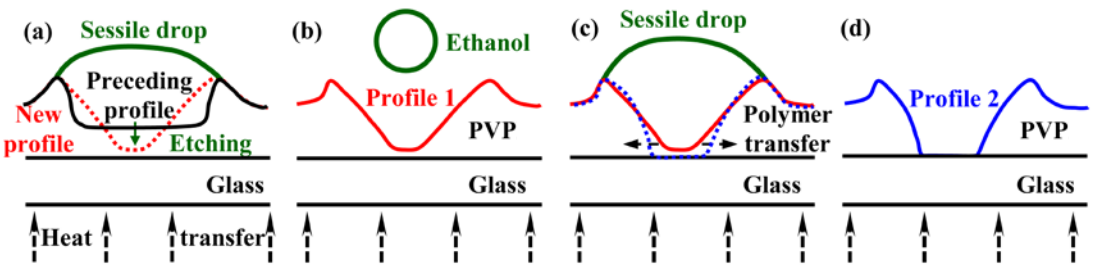

Figure 5-29 A schematic illustration of the proposed mechanism of via hole profile evolution with N_d for ethanol drops at higher temperatures. (a) A sessile drop wets the patterned polymer layer up to its ridge at a maximum distance (b) A new via hole forms after solvent evaporation. (c) Another drop wets within the hole up to its ridge (d) The new profile after the PVP film is completely penetrated.

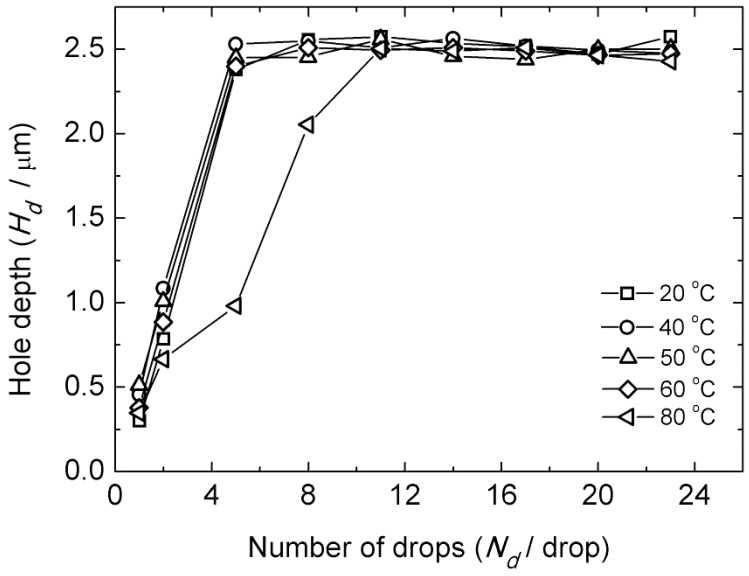

Figure 5-30 The profile of H_d versus N_d for ethanol drops at different stage temperatures.

As illustrated in Figure 5-30, the etching rate is not greatly compromised when elevated temperatures are applied to the printing stage below the boiling point of ethanol (78°C). The polymer layer is considered to be thoroughly penetrated after 5 drops for temperatures below the boiling point. Above the boiling point, more than 8 drops are needed to penetrate the PVP layer completely, due to the extremely fast solvent evaporation.

Aspect ratios as calculated by both H_d /D_{out} and H_d /D_{in} are given in Figure 5-31. It can be clearly seen that the aspect ratio of the via holes produced increases with temperature, since both D_{out} and D_{in} decrease with increasing temperature for completely etched via holes, and the ratio increases more strongly for H_d /D_{in} than for H_d /D_{out}. This can be used as a method to reduce the size and increase the aspect ratio of via holes produced using the inkjet etching technique.

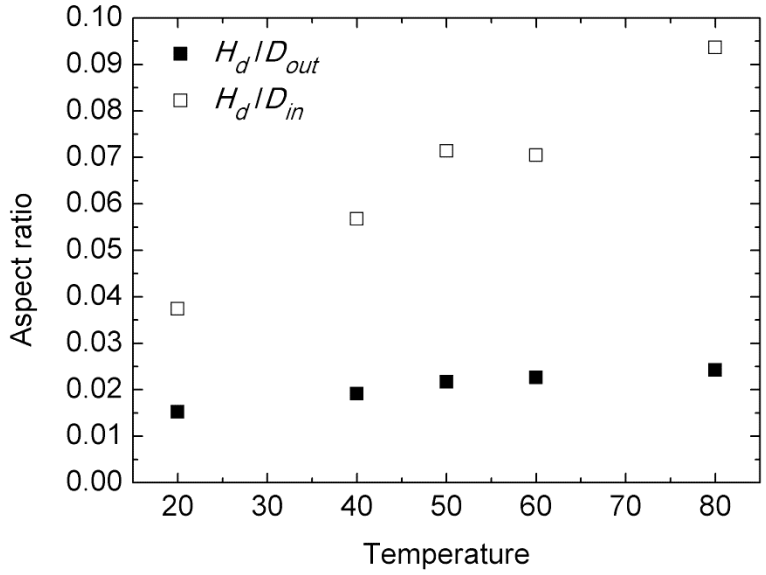

Figure 5-31 The aspect ratio (H_d/D_{out} and H_d/D_{in}) for completed etched via holes produced at various temperatures

5.5 Summary

This chapter has explored some of the factors which influence the dimensions of via holes produced by inkjet etching, including droplet ejection frequency, droplet diameter (D_0), solvent types and substrate temperature.

A threshold droplet ejection frequency f_c was found. For via holes produced at frequencies above f_c, both D_{out} and D_{in} increase with N_d. If below f_c, both D_{out} and D_{in} stay constant when all polymer is transferred outwards away from the bottom centre with no residual polymer left. Ideally, droplet ejection frequency does not change the diameter of the droplet, which in turn indicates that the via holes produced by only one droplet is of the same size regardless of the ejection frequency.

Larger droplets cover more area on the polymer surface, resulting in a larger contact area, which renders larger via hole diameters. Both D_{out} and D_{in} were found to increase linearly with D_0. Profiles of D_{in} versus D_o for different polymer thicknesses were fitted to different lines intersecting the D_0 axis at various points. Two conclusions can be drawn from this. First, the polymer thickness has an impact on D_{in},

but not D_{out}. The thicker the polymer is, the smaller D_{in} is. Second, the minimum amount of solvent needed to completely penetrate the polymer layer increases with polymer thickness.

The influence of the solvent on the size evolution of via holes with N_d depends on its evaporation properties: boiling point and vapour pressure. Solvents with high boiling points and low vapour pressure can enlarge via holes and create the refill issue even at low droplet ejection frequencies. It has also been demonstrated that substrate temperature is able to decrease the diameter of the via hole. Both D_{out} and D_{in} decrease with increasing temperature.

6 Penetration

This chapter mainly studies the factors that can influence whether via holes produced by inkjet etching achieve complete penetration of the polymer layer. The experiments were performed under such conditions that each etchant drop evaporated substantially before the next one lands on the polymer surface.

6.1 Penetration Testing Using Electroplating

In chapter 5, the via holes produced were considered to penetrate the PVP layer completely without any residual polymer at the bottom if the depth of hole is approximately equal to the thickness of the PVP layer. However, comparison between the depth of hole and PVP thickness cannot provide sufficient evidence to prove the absence of any PVP residue at the bottom of the via holes. Xia, *et al*. have reported detecting a residual layer several nanometres thick at the centre of their via holes, which indicated that the holes were not completely etched through to the bottom[13,14]. Nonetheless, they also showed that repeated solvent dispensing can eventually remove this residue. It is therefore very difficult to know precisely if the via holes are completely etched or there is still residual polymer present at the bottom. Hence a more accurate technique was developed to test the completeness of penetration: electroplating.

6.1.1 The Principle

The principle of the penetration test method employed here is that electroplating processes can only occur on to a conducting substrate. The samples used were different from the previous ones in that there is a layer of sputtered Cu in between the substrate and the spin coated PVP polymer layer. This metallic layer was used to help

identify the presence of any polymer residue by it blocking an electroplating process. Before spin coating, substrates with sputtered Cu on top had tape applied around the edge area so that the area was protected from being covered with PVP, as shown in Figure 6-1 (a). The prepared sample was placed in the spin coating device to have a PVP layer coated on top of the sputtered Cu afterwards, as shown in Figure 6-1 (b). The tape was then peeled off so that a Cu opening was exposed to make electrical connection with the electrode, as shown in Figure 6-1 (c).

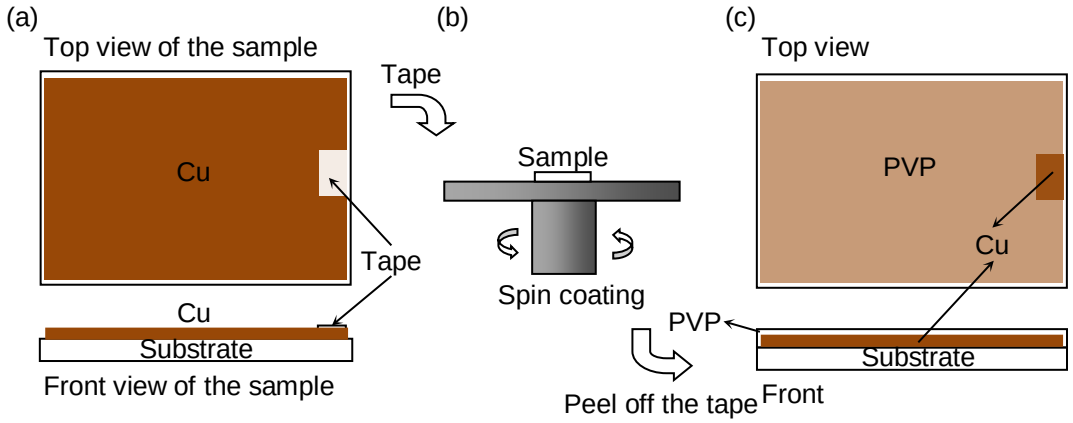

Figure 6-1 The procedure for preparing a sample used in the penetration test

The sample to be tested was immersed in the electrolyte, a commercially available $CuSO_4$ based electrolyte solution, with its exposed Cu area above the solution level and connected as the plating cathode. The anode was a Cu plate, which provided a source of Cu atoms to be oxidised into Cu cations.

When the via hole is completely etched through the PVP layer, Cu is exposed to the electrolyte and a circuit is formed between the electrolyte solution and electrodes, as indicated by the dashed line in Figure 6-2(a). At the anode, the Cu plate keeps supplying Cu^{2+} to the electrolyte solution in the following oxidation reaction:

$$Cu - 2e^- = Cu^{2+}$$

Cu^{2+} tends to move to the cathode and be reduced to Cu during the following reduction reaction where Cu is deposited in the penetrated via hole.

$$Cu^{2+} + 2e^- = Cu$$

This process is illustrated in Figure 6-2 (a).

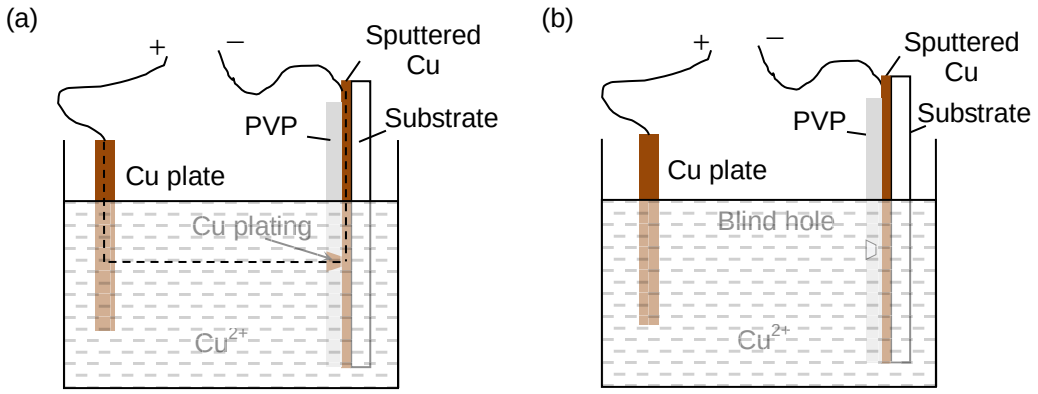

Figure 6-2 (a) Cu deposition in the via hole during electroplating when the PVP layer is completely penetrated and a circuit forms through the hole opening as indicated by the dashed line (b) No Cu deposition in the via hole when the PVP layer is only partially penetrated.

When the PVP layer is not completely dissolved and residual polymer is present at the bottom, only a blind hole is formed in the dielectric PVP layer. An open circuit is caused between the electrolyte solution and the electrodes due to the electrical insulation of the polymer. Neither oxidation nor reduction reaction can happen at the anode or cathode. Therefore, no Cu deposition can be found in partially dissolved blind via holes, as illustrated in Figure 6-2(b). The surface energy for glass and Cu used in this work were found to be 48.3mJ/m^2 and 45.5mJ/m^2 respectively, fairly close to each other. Additionally, Deegan, *et al*. have already demonstrated experimentally that the coffee ring effect occurs on a wide variety of substrates and is insensitive to a wide range of experimental conditions including surface energy [3]. Therefore, it is believed that glass and Cu surfaces are substantially equivalent.

6.1.2 Electroplating Test Results

The droplet ejection frequencies utilised for producing via holes subsequently used for the electroplating test were 1Hz and 2Hz. The waveform parameters were U_{dwell}=55V, t_{dwell}=45µs. The size of the droplet was estimated to be 33µm (19pl). Figure 6-3 presents optical microscopy images of via holes created by 1-6 drops of ethanol at an ejection frequency of 1Hz, before and after electroplating.

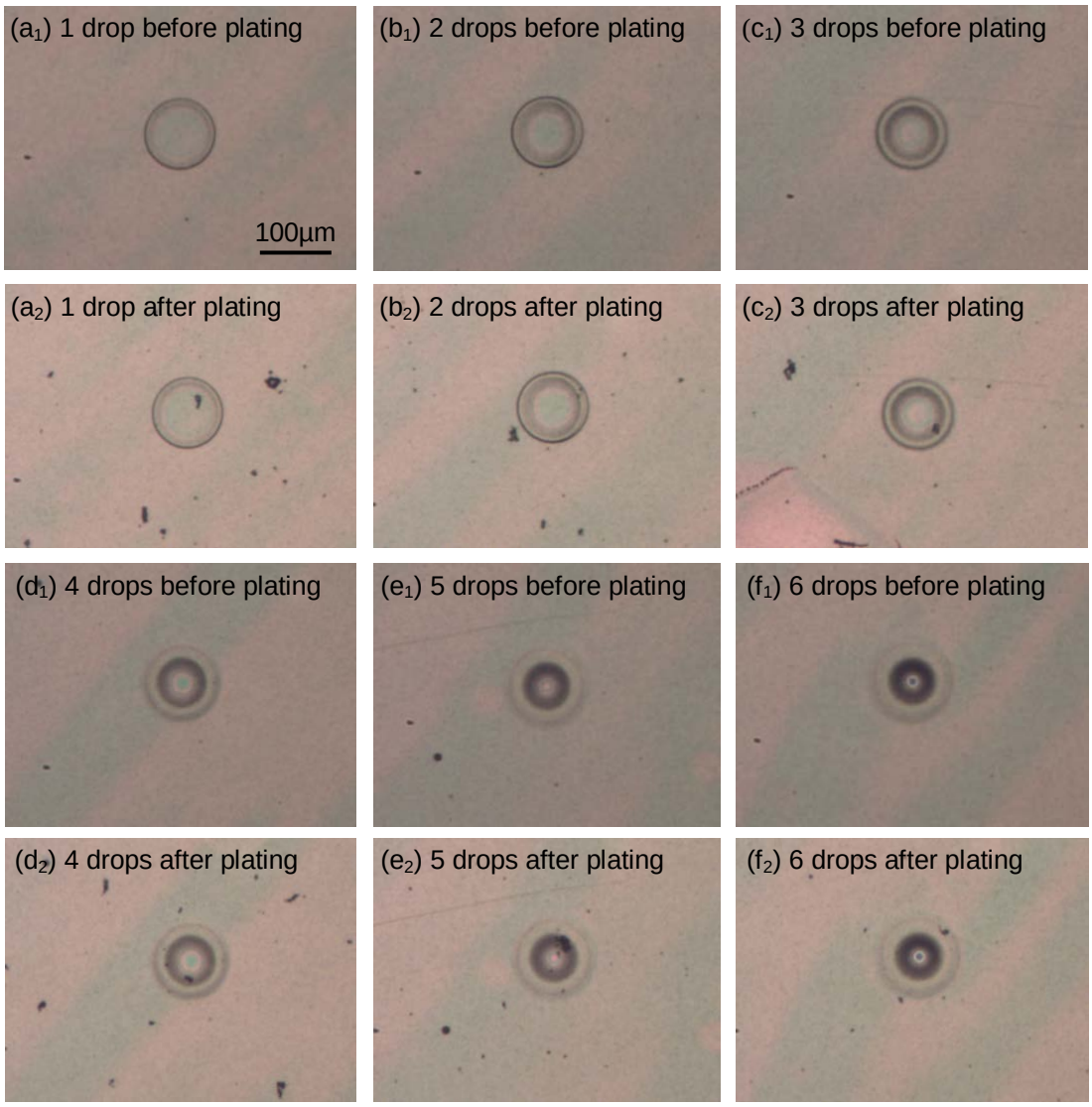

Figure 6-3 Optical microscopy images of via holes created by 1 to 6 drops of ethanol before and after the electroplating process. The droplet ejection frequency was 1Hz.

From the photos above, it can be clearly observed that no apparent change occurs at the bottom of any of the holes. No Cu deposition can be found within the holes produced by 6 drops of ethanol or less, which indicates that residual polymer is present at the bottom of all these via holes. Figure 6-4 presents the optical microscopy images of via holes created by 7 drops or more at an ejection frequency of 1Hz.

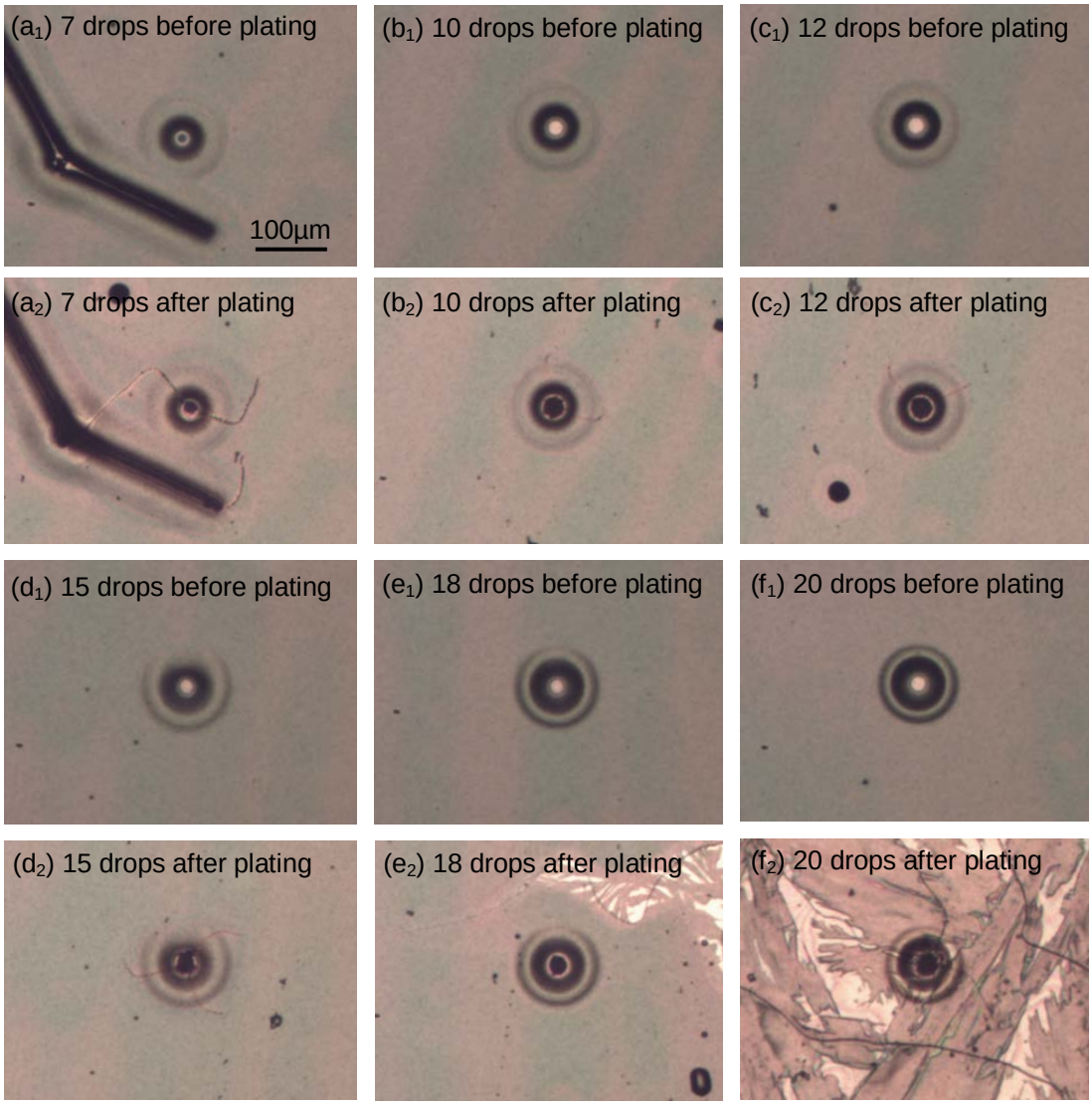

Figure 6-4 Optical microscopy images of via holes created by 7 to 20 drops of ethanol before and after the electroplating process. The droplet ejection frequency was 1Hz.

Cu deposition can be found in the holes created by 7 or more drops. For the one produced by 7 ethanol drops, the residual polymer might not be removed from the centre completely, which results in partial Cu plating in the hole. For via holes created by 10 drops or more, it can be observed that the Cu layer beneath the polymer is exposed before electroplating, and Cu deposition occurs over the whole hole area after electroplating, which indicates absence of polymer residue at the bottom and complete penetration of the dielectric layer. Cracking of some areas of the polymer layer

occurred after electroplating and damaged the via hole appearance, as shown in Figure 6-4 (f_2).

Figure 6-5 and Figure 6-6 are optical microscopy images of via holes created by different numbers of ethanol drops at an ejection frequency of 2Hz, before and after electroplating. Figure 6-5 shows via holes with the presence of polymer residue at the bottom before electroplating, and no Cu deposition after. Figure 6-6 presents via holes without polymer residue before electroplating and successful Cu deposition after electroplating.

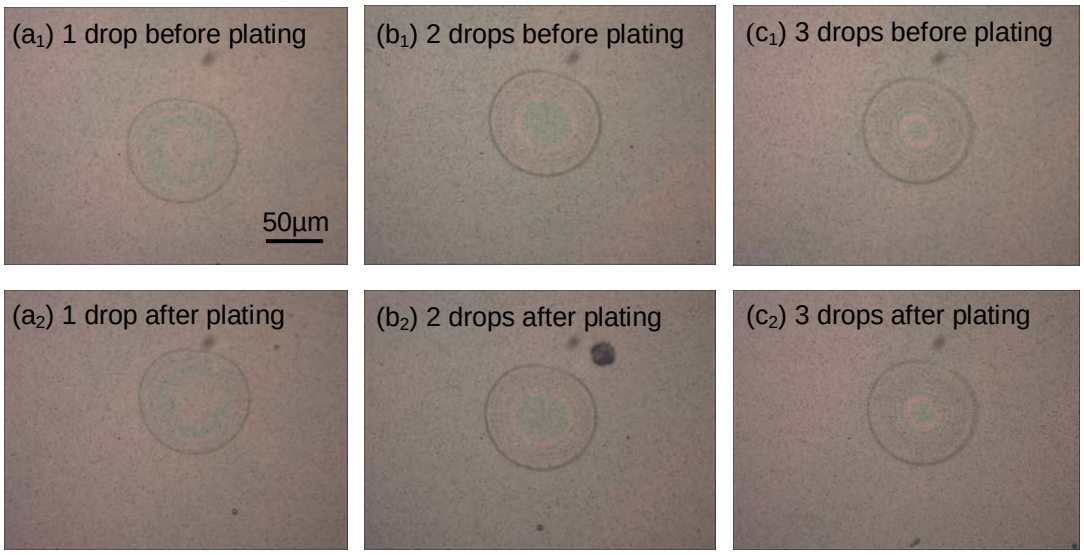

Figure 6-5 Optical microscopy images of via holes created by 1 to 3 ethanol drops at the droplet ejection frequency of 2Hz before and after electroplating. No Cu plating is found in these via holes.

The electroplating test provides more convincing evidence for the development of via hole size versus the number of droplets, as discussed in chapter 5. Using ethanol as the etching solvent, once the layer has been penetrated completely, further droplet dispensing does not change the size of the via hole. Extra droplets do not cause the issue of hole refill.

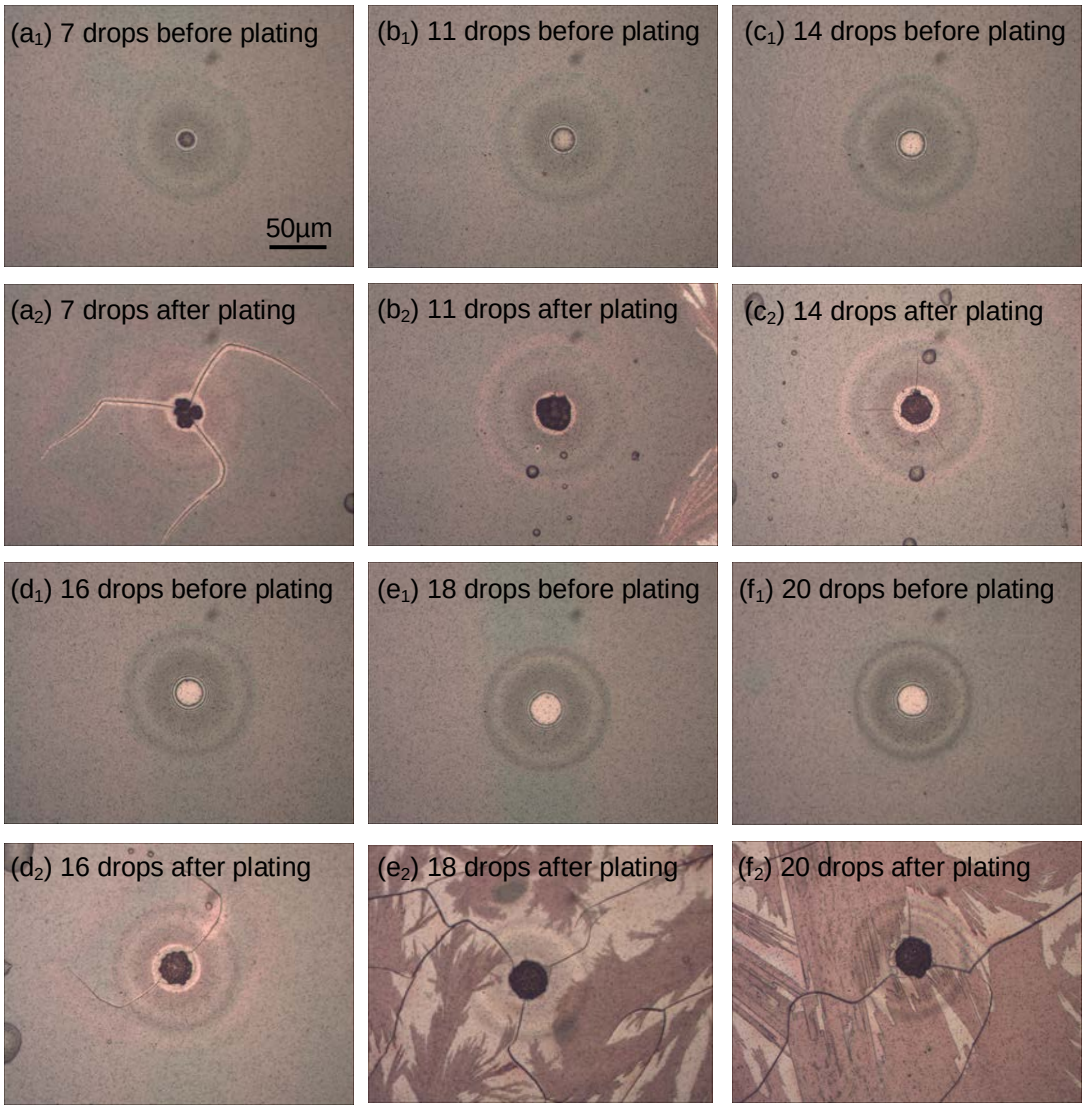

Figure 6-6 Optical microscopy images of via holes created by 7 to 20 ethanol drops at the droplet ejection frequency of 2Hz, before and after electroplating. The shining Cu layer beneath the polymer is exposed and Cu deposition can be found in the holes after electroplating.

6.2 Effect of Outer Diameter (D_{out}) on Penetration

As discussed in chapter 5, the mechanism of the via hole formation is re-deposition of the dissolved polymer during solvent evaporation. Since there is neither local removal of the dissolved polymer from inside the hole nor evaporation of the dissolved polymer, the re-deposited polymer must occupy the space within or around the formed via hole. The smaller the outer diameter of the via hole is, the less the volume of the via hole will be, and the more likely the hole will be refilled. Therefore,

one can expect that there is a correlation between the outer diameter and the penetration of the via hole produced. This section experimentally investigates the relationship between D_{out} and D_{in} for a fixed polymer thickness.

6.2.1 Sample Preparation

Print heads with different nozzle sizes were used and various temperatures were applied to the printing stage in order to obtain different D_{out}. Seven rows of via holes were created by printing IPA drops onto the glass sample coated with PVP. Since the development of D_{in} versus N_d has already been established, only five holes in a row were produced here by dispensing 10, 20, 30, 40 and 50 IPA droplets respectively to avoid repetition. A delay of 10s was applied in the printing script to allow for sufficient evaporation. The experimental parameters are listed in Table 6-1.

Table 6-1 Experimental parameters

Line No.	Nozzle size (μm)	Printing stage temperature (°C)	Droplet diameter (μm)	Droplet volume (pl)
1	40	70	45	49
2		60		
3		50		
4		40		
5		30		
6		20		
7	60	20	58	105

6.2.2 Results

As shown in Figure 6-7, when solvent evaporation is dominant, D_{in} remains unchanged regardless of N_d after the polymer layer is almost completely penetrated. Therefore the average D_{in} was calculated using only the holes produced by 20 or more drops, when the hole depth is approximately equivalent to the polymer thickness *i.e.* 4.53±0.08μm. Table 6-2 lists the values of D_{in} and H_d corresponding to the different D_{out} of via holes created in the same polymer layer. From the table below, one can observe that D_{in} decreases with D_{out} and H_d approximates the thickness of the polymer.

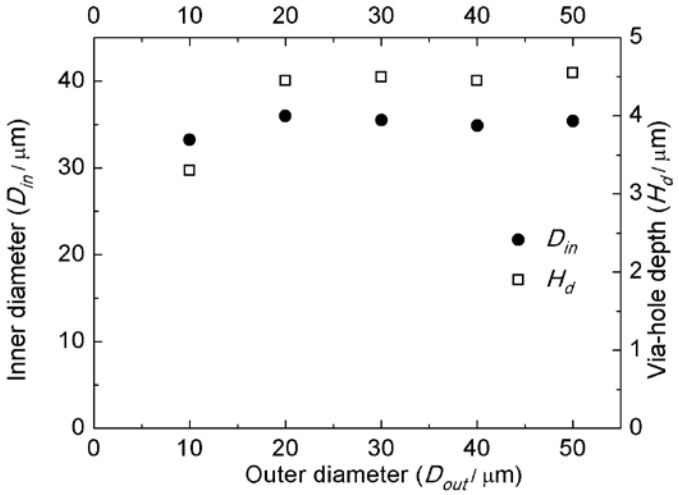

Figure 6-7 D_{in} and H_d versus D_{out} for via holes in line 7

Table 6-2 Dimensions (outer diameter D_{out}, inner diameter D_{in} and the depth of hole H_d) of via holes produced for the different experimental parameters

Line No.	D_{out} (μm)	D_{in} (μm)	H_d (μm)
1	70±1	10±2	4.56±0.04
2	76±1	14±2	4.54±0.06
3	83±1	17±2	4.65±0.02
4	92±2	21±2	4.46±0.03
5	103±1	26±2	4.42±0.03
6	134±2	35±2	4.49±0.05
7	152±1	46±2	4.53±0.04

Figure 6-8 presents the relationship between D_{in} and D_{out}, which can be described by a linear equation: D_{in}=0.4D_{out}-17.7. Due to the nozzle size limit and the low surface tension of IPA, the smallest D_{out} that could be achieved with a completely-penetrated polymer layer in this study was 70μm. However, by extrapolating the linear equation to the intersection A (D_{in}=0), we have D_{out}=44μm. Therefore, to penetrate a 4.5μm thick PVP layer with IPA, the minimum outer diameter $D_{out\ min}$ of the via hole should exceed 44μm. If D_{out} is smaller than $D_{out\ min}$, the resulting via hole cannot penetrate the polymer layer completely. This therefore defines the maximum aspect ratio achievement using this technique.

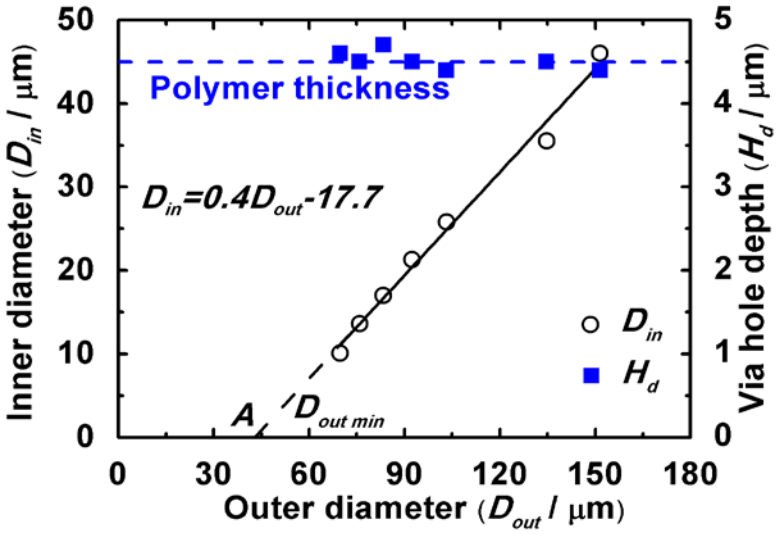

Figure 6-8 The profile of H_d and D_{in} as a function of D_{out}

6.3 Effect of Polymer Thickness on Penetration

6.3.1 Sample Preparation

Samples having different polymer thicknesses were achieved by varying the polymer concentration in the PVP/IPA solutions and the parameters during the spin coating process as listed in Table 6-3.

Table 6-3 Polymer concentrations and spin coating parameters used to generate different polymer thicknesses

Sample	Polymer concentration (*wt*.%)	Spin coating parameters		Polymer thickness (μm)
		Speed (rpm)	Time (s)	
1	6.0	2000	40	0.38±0.05
2	7.8	1500	30	0.78±0.06
3	11.3	1500	30	1.27±0.03
4	14.5	1200	40	2.34±0.04
5	14.5	1000	30	2.52±0.05
6	20.3	1200	30	3.43±0.05
7	29.8	1800	30	4.53±0.05
8	29.8	1500	30	5.27±0.04

The effect of polymer thickness on penetration was investigated using a fixed droplet diameter/volume. A Φ40μm nozzle was used to jet IPA as the etching solvent.

The jetted droplet diameter and volume were estimated to be approximately 38µm and 30pl respectively. A delay of 10s was also applied in the printing script to allow sufficient time for evaporation.

6.3.2 Results

Figure 6-9 illustrates the relationship between D_{in}, D_{out} and polymer thickness. It can be clearly observed that D_{in} decreases with increases of polymer thickness, while D_{out} stays independent of polymer thickness. Since D_{out} is primarily determined by drop diameter/volume, it remains constant due to the fixed droplet diameter used in the experiment. D_{in} decreases rapidly with polymer thickness at the initial stage, but then slowly when the polymer layer becomes thicker.

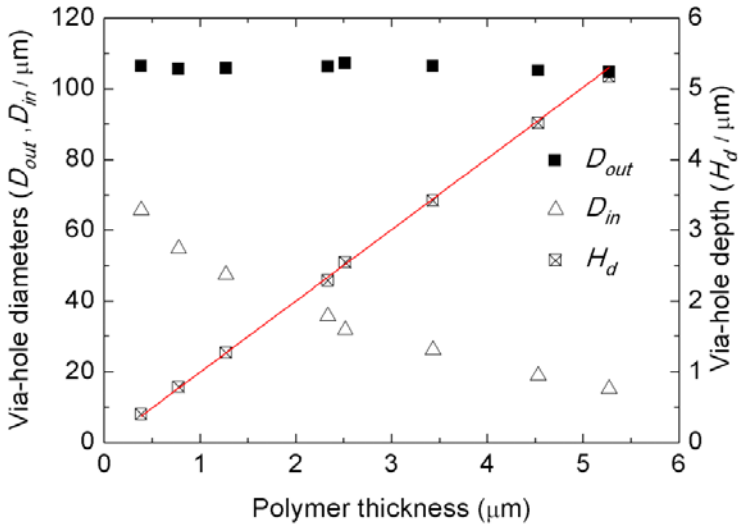

Figure 6-9 The profile of D_{out} and D_{in} as a function of the polymer thickness

The depth of the produced via hole and the corresponding polymer thickness are proportional, with the constant of proportionality being 1 as plotted by the solid line in Figure 6-9. This implies that the depth of each via hole created is equivalent to the polymer thickness, which, in turn, indicates complete penetration of the polymer films. Due to the difficulty of further increasing PVP thickness because of the internal stress induced, which can cause polymer cracking, the threshold polymer thickness could not be found experimentally in this work. However, it can be postulated that a

threshold polymer thickness exists, above which a 38μm IPA droplet cannot successfully penetrate the entire PVP layer regardless of the number of drops dispensed.

6.4 Mechanism Discussion

This section demonstrates calculation of the velocity of the flow within the sessile drop during evaporation, and then moves on to consider diffusion flux as the barrier to the outward flow caused by the coffee ring effect, and the underlying reason for the existence of a penetration limit.

6.4.1 Contribution of Surface Tension

Laplace pressure is defined as the difference in pressure between the inside and the outside of a curved surface forming an interface between liquid and gas phases. It is caused by the surface tension of the interface and is expressed as [157]:

$$\Delta P = P_1 - P_2 = \sigma\left(\frac{1}{R_1} + \frac{1}{R_2}\right) \quad \textbf{(6-1)}$$

where ΔP is the pressure difference between the inside and outside of the surface (Pa);

P_1 is the inside pressure (Pa);

P_2 is the outside pressure (Pa);

R_1, R_2 are the radii of curvature of the liquid/gas interface;

and σ is the surface tension of the interface (N/m).

Equation (6-1) can be reduced to $\Delta P = \frac{2\sigma}{R}$ for a spherical surface *i.e.* when $R_1=R_2=R$. The phenomenon of two immiscible liquids forming a curved interface between them due to this pressure is well understood. However, the system in this work is far more complicated as there is no discrete boundary between the liquid and the solid polymer substrate. Instead there is a concentration gradient due to the dissolution of the polymer into the solvent drop. The Laplace pressure has been postulated to be the cause of the depression formed on a non-rigid but insoluble substrate [158,159]. However such a system is also less complex than considered here and a more complex model is required to allow an understanding of this phenomenon.

The ridge height of the via hole (H_r), as indicated in Figure 5-1, does not keep increasing, because the wetting condition changes as the via hole goes deeper. This is confirmed by Figure 6-10.

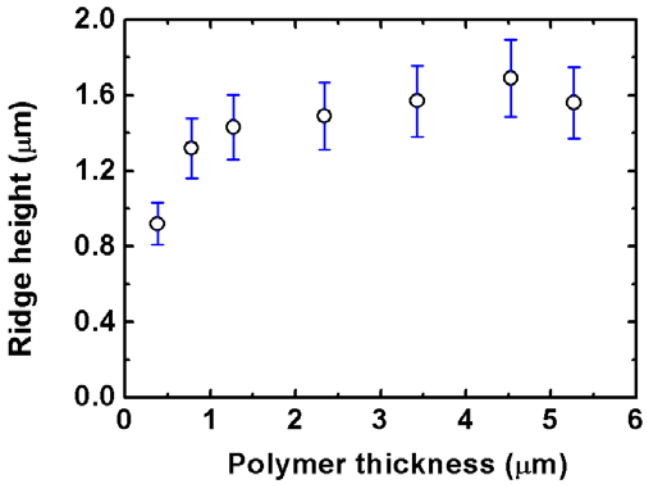

Figure 6-10 The evolution of ridge height for completely etched via holes versus the polymer thickness

During the first several drops, the in-flight droplet lands on the substrate and wets to the rim of the previous via hole at its maximum distance, as sketched in Figure 6-11 (c) (lower inset). However, as the ridge increases and the hole is etched deeper, the volume of the hole also expands. The shape of the via hole is approximately that of a truncated cone, as shown in Figure 6-11 (a). A lower limit estimate of the via hole was calculated using a number of cylinders with a thickness of 0.1μm locating within the hole, as illustrated in Figure 6-11 (b). The deviation between this and an estimate of via hole volume using a truncated cone is less than 6%, which indicates the truncated cone calculation provides a good approximation. The volume of the via hole will exceed that of the in-flight droplet at some point, as shown in Figure 6-11 (c). Therefore, the drop is expected to remain within the via hole rather than wetting up to the rim when the polymer thickness exceeds a certain value, as shown in Figure 6-11 (c) (upper inset).

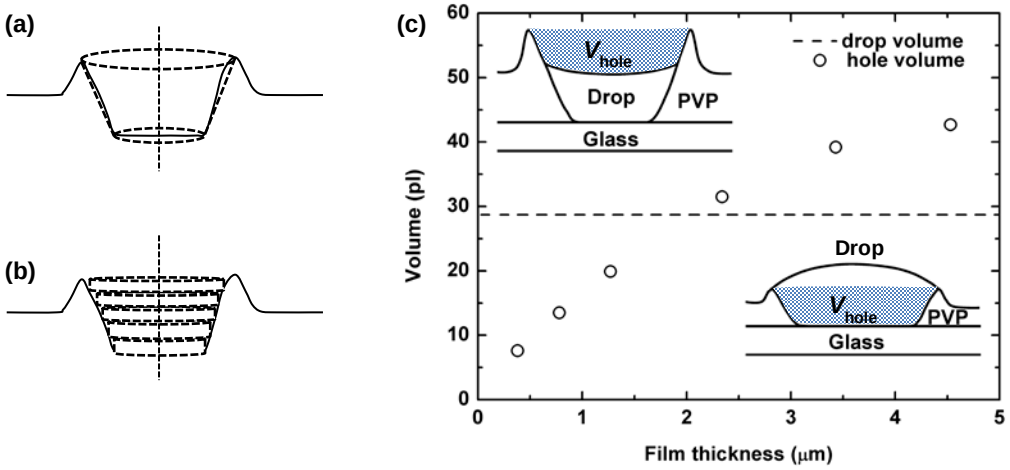

Figure 6-11 The evolution of hole volume versus the film thickness

Since the occurrence of a ridge in a via hole profile is a result of the surface tension exerted by the sessile drop on the polymer layer pulling the dissolved polymer upwards [158], the transition of the wetting condition prevents the surface tension from further increasing the ridge height once the droplet is located within the via hole. Therefore any further re-deposition must occur within this space, causing D_{in} to decrease.

6.4.2 Velocity Calculation for Coffee Ring Flows

Figure 6-12 establishes the coordinate system of an evaporating sessile drop. The vertically-averaged radial flow of the liquid $v(r,t)$ can be expressed as follows [3]:

$$v(r,t) = -\frac{1}{\rho r h}\int_0^r [J(r,t)\sqrt{1+\left(\frac{\partial h}{\partial r}\right)^2} + \rho\frac{\partial h}{\partial t}]rdr \qquad \textbf{(6-2)}$$

where $v(r,t)$ is the averaged radial flow of the liquid (m/s);

R is the wetting radius of the sessile drop on the substrate (m);

θ is the contact angle (rad);

ρ is the density of the solvent (kg/m^3);

h is the height of the sessile drop at radius r (m);

and J is the mass loss from the sessile drop per unit area per unit time (kg/m^{2}s).

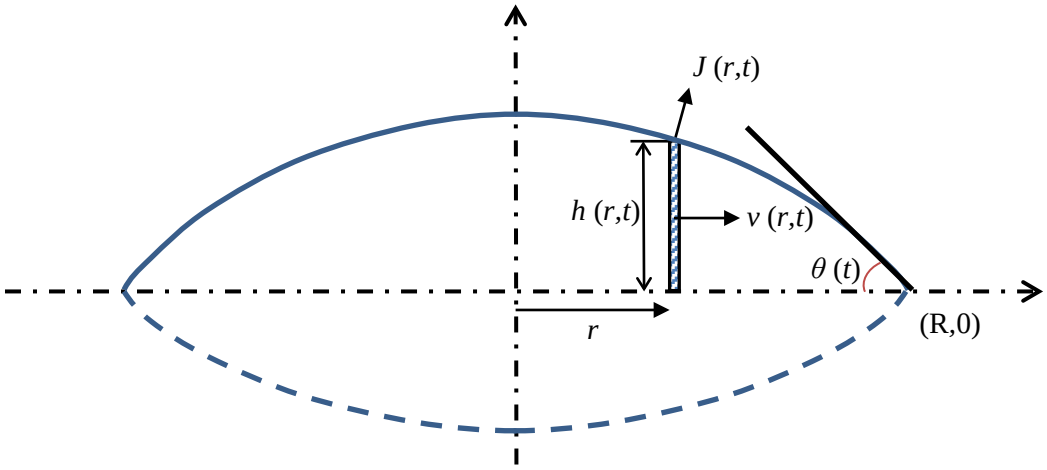

Figure 6-12 Cross section of an evaporating sessile drop in a cylindrical coordinate system with relevant parameters

By splitting the integral function in equation (6-2) into two terms v_1 and v_2, it can be rewritten as:

$$v(r,t) = v_1 + v_2 \tag{6-3}$$

where $v_1$is $-\frac{1}{\rho r h}\int_0^r J(r,t)\sqrt{1+\left(\frac{\partial h}{\partial r}\right)^2}\,rdr$ and v_2 is $-\frac{1}{rh}\int_0^r \frac{\partial h}{\partial t} rdr$.

In order to calculate $v(r,t)$, both $J(r,t)$ and $h(r,t)$ need to be specified. The explicit expressions for $J(r,t)$ and $h(r,t)$ used here are taken from the literature [148,160]:

$$J(r,t) = J_0(\theta)(1-\tilde{r}^2)^{-\lambda(\theta)} \tag{6-4}$$

$$J_0(\theta) = \frac{Dc_v}{R}(0.27\theta^2 + 1.30)[1-\Lambda(\theta)] \tag{6-5}$$

$$\Lambda(\theta) = \lambda(\theta) + \delta(\theta) = 0.2239(\theta - \frac{\pi}{4})^2 + 0.3619 \tag{6-6}$$

$$\lambda(\theta) = 0.5 - \frac{\theta}{\pi} \tag{6-7}$$

$$h(r,t) = \sqrt{\frac{R^2}{sin^2\theta} - r^2} - \frac{R}{tan\theta} \tag{6-8}$$

$$\sqrt{1+\left(\frac{\partial h}{\partial r}\right)^2} = (1-\tilde{r}^2)^{-\delta(\theta)} \tag{6-9}$$

where $J_0(\theta)$ is the evaporation flux at r=0 for a specific contact angle θ (kg/m^2·s);

$\tilde{r} = r/R$;

D is the diffusion coefficient of the solvent into air (m^2/s);

c_v is the saturated vapour concentration (kg/m^3);

Therefore, we have:

$$\begin{aligned} v_1 &= -\frac{1}{\rho r h}\int_0^r J(r,t)\sqrt{1+\left(\frac{\partial h}{\partial r}\right)^2}\, r dr \\ &= -\frac{1}{\rho r h}\int_0^r J_0(\theta)(1-\tilde{r}^2)^{-\lambda(\theta)}(1-\tilde{r}^2)^{-\delta(\theta)} r dr \\ &= \frac{J_0(\theta)}{2\rho r h}\int_0^r (1-\tilde{r}^2)^{-\Lambda(\theta)} d(-r^2) \\ &= \frac{J_0(\theta)R^2}{2\rho r h}\int_0^r (1-\tilde{r}^2)^{-\Lambda(\theta)} d\left(1-\frac{r^2}{R^2}\right) \\ &= \frac{J_0(\theta)R^2}{2\rho r h}\int_0^{\frac{r}{R}} (1-\tilde{r}^2)^{-\Lambda(\theta)} d(1-\tilde{r}^2) \\ &= \frac{J_0(\theta)R^2}{2\rho r h(1-\Lambda(\theta))}(1-\tilde{r}^2)^{1-\Lambda(\theta)}\Big|_0^{\frac{r}{R}} \\ &= \frac{J_0(\theta)R^2}{2\rho r h(1-\Lambda(\theta))}\left[(1-r^2/R^2)^{1-\Lambda(\theta)}-1\right] \\ &= \frac{RDc_v}{2\rho r h}(0.27\theta^2+1.30)[(1-r^2/R^2)^{1-\Lambda(\theta)}-1] \end{aligned} \tag{6-10}$$

According to Hu and Larson [160]:

$$\frac{\partial h}{\partial t} = \dot{h}(0,t)(1-\tilde{r}^2) = \frac{2\dot{m}(t)}{\rho\pi R^2}(1-\tilde{r}^2) \tag{6-11}$$

$$\dot{m}(t) = -\pi R D c_v (0.27\theta^2+1.30) \tag{6-12}$$

Substitution of equation (6-11) and (6-12) into v_2 yields:

$$v_2 = -\frac{1}{rh}\int_0^r \frac{\partial h}{\partial t} r dr = -\frac{1}{rh}\int_0^r \frac{-2\pi RDc_v(0.27\theta^2+1.30)}{\rho\pi R^2}(1-\tilde{r}^2) r dr =$$

$$= -\frac{1}{rh}\int_0^r \frac{\pi RDc_v(0.27\theta^2+1.30)}{\rho\pi R^2}(1-\tilde{r}^2) d(-r^2)$$

$$= -\frac{1}{rh}\int_0^r \frac{\pi RDc_v(0.27\theta^2+1.30)}{\rho\pi}(1-\tilde{r}^2) d(1-\frac{r^2}{R^2}) \quad \textbf{(6-13)}$$

$$= -\frac{RDc_v(0.27\theta^2+1.30)}{\rho rh}\int_0^{\frac{r}{R}}(1-\tilde{r}^2) d(1-\tilde{r}^2)$$

$$= -\frac{RDc_v(0.27\theta^2+1.30)}{2\rho rh}(1-\tilde{r}^2)^2\Big|_0^{\frac{r}{R}}$$

$$= -\frac{RDc_v(0.27\theta^2+1.30)}{2\rho rh}[(1-\frac{r^2}{R^2})^2-1]$$

Hence, equation (6-3) can be expressed as:

$$v(r,t) = v(r,\theta) = v_1 + v_2$$

$$= \frac{RDc_v(0.27\theta^2+1.30)}{2\rho r\left(\sqrt{\frac{R^2}{sin^2\theta}-r^2}-\frac{R}{tan\theta}\right)}\left[\left(1-\frac{r^2}{R^2}\right)^{0.6381-0.2239\left(\theta-\frac{\pi}{4}\right)^2}-1\right] \quad \textbf{(6-14)}$$

$$-\frac{RDc_v(0.27\theta^2+1.30)}{2\rho r\sqrt{\frac{R^2}{sin^2\theta}-r^2}-\frac{R}{tan\theta}}\left[\left(1-\frac{r^2}{R^2}\right)^2-1\right]$$

The diffusion coefficient of IPA in air can be calculated using equation (5-12) to be D=9.96×10^{-7}m^2/s; R=D_{out}/2=53μm; c_v=1.046×10^{-7}g/m^3; ρ=786kg/m^3. The flow velocity within the sessile drop can be plotted as shown in Figure 6-13 after substitution of all the values above into (6-14).

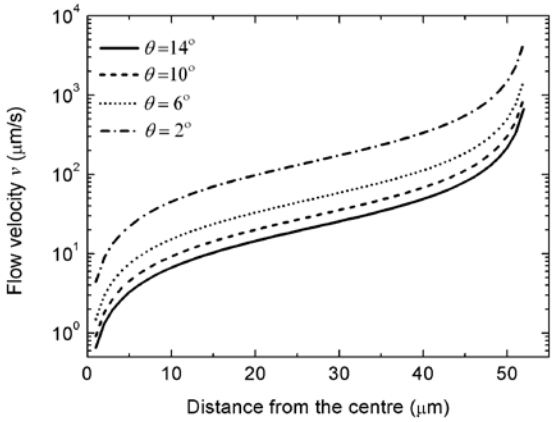

Figure 6-13 Predicted outward flow velocity as a function of distance from the centre at different contact angles within the sessile drop

As more polymer is re-deposited at the contact line, the polymer concentration front advances toward the centre, while the diffusion flux near the centre keeps increasing as it approaches the front. Therefore the net outward flow is believed to become smaller and smaller as the diffusion flux becomes more dominant. The diffusion speed can reach as high as 100μm/s according to Kawase, *et al.* [5]. The outward flow due to the coffee ring effect at locations less than 20μm from the centre, on the other hand, is below 100μm/s, as shown in Figure 6-13. It is therefore believed that there is a point when the net flow is inward, when diffusion dominates the process and the polymer layer cannot be completely etched through.

6.5 Summary

This chapter mainly discussed the penetration issue of inkjet-etched via holes. This issue is highly significant as these holes need to be thoroughly penetrated through the entire polymer layer, so that subsequent filling with conductive materials converts the structure into electrically-conductive vias. The chapter began with electroplating thoroughly-etched via holes with Cu as a precise penetration test technique, which can ascertain whether polymer residue is present at the bottom of via holes regardless of any polymer thickness variation. Experimental results showed that via holes produced by 7 drops or more were observed to have Cu covering their base after electroplating, which indicated the absence of polymer residue at the bottom of

those via holes. For those produced by less than 7 drops, no Cu could be found after electroplating, due to the open circuit caused by residual polymer between the electrolyte solution and the metal layer. Electroplating provides strong evidence for successful via hole penetration.

It is expected that there is a threshold polymer thickness above which a certain amount of solvent cannot completely etch through the polymer layer. The outward flow velocity was calculated and the relationship between this flow and diffusion was proposed to explain the existence of the penetration limit. The limit is postulated to be caused by stronger diffusion as well as a transition of the wetting condition.

7 Influence of the Marangoni Effect on Polymer Drying Patterns

Previous chapters described various experiments conducted to test the factors which influence the size of via holes produced by inkjet printing and the penetration limit for a specific solvent and droplet volume. However, it has been demonstrated that this method can also be employed to fabricate protrusions instead of depressions in polymer layers. This protrusion pattern was also observed while isobutanol was used as the etchant. This chapter aims to propose a mechanism to explain the bump-like structures observed in the polymer layer when using isobutanol as the etchant, as presented in chapter 5.

7.1 The Marangoni Effect

The Marangoni effect is mass transfer induced by a surface tension gradient, which causes a flow from the low surface tension area to the high surface tension area. Such flows have been observed in sessile drops, e.g. Hu, *et al.* [161] used monodispersed PMMA fluorescent particles as tracers to visualise a strong recirculating Marangoni flow in a drying octane droplet.

It has already been reported that solvent mixtures can be used to modulate the shape of polymer patterns [9,10,11,162,163,164,165,166]. The mechanism behind this pattern modulation is believed to be caused by the dissimilar surface tension and boiling points of the two mixture components. Since the evaporation at the contact line of the sessile drop is faster, this creates a dissimilar concentration of the low boiling point component at the contact line than in the centre, which induces an increasing surface tension gradient from the contact line to the centre. This surface tension gradient

contributes to the polymer re-deposition in the centre due to the inward Marangoni flow. The Marangoni number is usually very large in such solvent mixtures [167,168], which results in a strong Marangoni flow countering the coffee ring flow. Meanwhile, solutions with only one solvent component have also been reported to result in a bump-like appearance in some cases [10,169]. Such features have also been demonstrated in section 5.3.1 of this thesis.

Nonuniform evaporation from a sessile drop induces a temperature gradient within the drop, which generates a Marangoni flow. Ristenpart, *et al.* [170] investigated the influence of substrate conductivity on the temperature gradient and the Marangoni circulation direction. It is reported that an evaporating sessile drop is warmer at the contact line than in the centre only if the ratio ($k_R = k_S/k_L$) of substrate conductivity (k_S) and liquid conductivity (k_L) is larger than 2. When k_R <1.45, the sessile drop is colder at the contact line than in the centre. If 1.45< k_R <2, the temperature gradient depends on the contact angle. Their result is consistent with the numerical work by Hu and Larson, [171] who reported that the Marangoni recirculation reverses its direction at a critical angle.

7.2 Proposed Explanation

The Marangoni effect considered here is induced by thermal gradients caused by evaporation across the surface of the drop. It is known that evaporation tends to cool down the sessile drop, and uneven evaporation fluxes across the sessile drop surface create a temperature gradient. Since surface tension decreases with increasing temperature and the relationship between surface tension and temperature can be treated as linear for small temperature differences, [171] a surface tension gradient can be expected across the free surface of the sessile drop, which can, in turn, create a Marangoni flow within the sessile drop.

The thermal Marangoni number is defined as [171]:

$$Ma = -\beta \Delta T_0 \frac{t_f}{\mu R} \qquad \textbf{(7-1)}$$

where Ma is the Marangoni number;

β is the temperature coefficient of surface tension (N/m·K);

$\Delta T_0 = T_{contact\ line} - T_{centre}$ is the temperature difference between the contact line and the centre;

t_f is the evaporation time of the drop (s);

μ is the viscosity of the solvent (Pa·s);

and R is the contact line radius (m).

The temperature gradient across an evaporating sessile drop can be expressed as [170]:

$$\frac{\partial T}{\partial r} = \frac{\Delta H_v J_0}{k_L (2\cos\theta_c)^{\lambda-1}} r^{\lambda-1} \frac{1 + k_R \tan(\lambda\pi)\tan(\lambda\theta_c)}{\tan(\lambda\theta_c) - k_R \tan(\lambda\pi)} \quad \textbf{(7-2)}$$

where J_0 is the evaporation flux at r=0 (kg/m^2·s);

ΔH_v is the latent heat of evaporation (J/kg);

k_L is the thermal conductivity of the liquid (w/m·K);

k_R is the ratio of the thermal conductivity of the liquid to the substrate;

θ_c is the contact angle (rad);

$\lambda = 0.5 + \theta_c/\pi$;

and r is the radius distance of the position from the centre (m).

Therefore, the temperature difference between the contact line and the centre can be deduced from equation (7-2) to be:

$$\Delta T = \frac{\Delta H_v J_0}{k_L \lambda (2\cos\theta_c)^{\lambda-1}} R^{\lambda} \frac{1 + k_R \tan(\lambda\pi)\tan(\lambda\theta_c)}{\tan(\lambda\theta_c) - k_R \tan(\lambda\pi)} \quad \textbf{(7-3)}$$

Hu and Larson concluded that the evaporation rate remains nearly constant during evaporation [160]. Thus, we estimate the sessile drop volume using this simplified relation. The evaporation time for an isobutanol sessile drop was calculated to be 6.1s in section 5.3.2 and the jetting delay between two consecutive dispenses was 1s. In the beginning phase, the volume of the sessile drop increases with more isobutanol drops merging in and residual solvent left from incomplete evaporation. The contact angle also increases as a result of a pinned contact line. This condition holds until a dynamic

equilibrium is reached and a maximum contact angle/volume establishes. Therefore, the volume of the isobutanol sessile drop after N_d can be estimated with equations (7-4) and (7-5):

$$V_{Nd} = V_0 \times \frac{6.1-(N_d-1)}{6.1} + V_0 \times \frac{6.1-(N_d-2)}{6.1} + \cdots + V_0 \times \frac{6.1-1}{6.1} + V_0 = \frac{13.2N_d - {N_d}^2}{12.2} V_0 \, , N_d \leq 5 \quad \textbf{(7-4)}$$

$$V_{Nd} = V_0 \times \frac{6.1-5}{6.1} + V_0 \times \frac{6.1-4}{6.1} + \cdots + V_0 \times \frac{6.1-1}{6.1} + V_0 = 3.54 V_0 \, , N_d \geq 6 \quad \textbf{(7-5)}$$

The latent heat of evaporation can be estimated by [172]:

$$\Delta H_v = C_1 (1-T_r)^{C_2 + C_3 T_r + C_4 {T_r}^2 + C_5 {T_r}^3} \quad \textbf{(7-6)}$$

where ΔH_v is the latent heat of evaporation (J/kg);

C_1, C_2, C_3, C_4 and C_5 are constants;

$T_r = T/T_c$;

and T_c is the critical temperature (K).

The thermal conductivity can be approximated as [172]:

$$k = C_1 + C_2 T + C_3 T^2 + C_4 T^3 + C_5 T^4 \quad \textbf{(7-7)}$$

where C_1, C_2, C_3, C_4 and C_5 are constants;

Based on published values, [172] the latent heat of evaporation for isobutanol at 20ºC can be estimated to be:

$$\Delta H_v = C_1 (1-T_r)^{C_2 + C_3 T_r + C_4 {T_r}^2 + C_5 {T_r}^3} = 7.7646 \times 10^7 \times \left(1 - \frac{293.15}{407.8}\right)^{\frac{0.56757}{74.12}} \approx 509813 \text{ J/kg} \quad \textbf{(7-8)}$$

The thermal conductivity of isobutanol can be calculated to be:

$$k = C_1 + C_2T + C_3T^2 + C_4T^3 + C_5T^4 = 0.21258 - 0.00029864 \times 293.15 \approx 0.125 \text{ W/m·K} \quad \textbf{(7-9)}$$

When only one isobutanol drop is dispensed onto the substrate, the sessile drop volume is equal to the in-flight drop volume (V_0), which is 106pl, and the initial contact angle can be calculated as described in section 5.1.2.3 to be 12.7º. The thermal conductivity of PVP is taken as k_s=0.2W/mK based on the data [173] given. $k_R = k_s/k_L$ = 0.2/0.125=1.6. The temperature difference during its evaporation is therefore calculated to be:

$$\begin{aligned} \Delta T &= \frac{\Delta H_v J_0}{k_L \lambda (2\cos\theta_c)^{\lambda-1}} R^{\lambda} \frac{1 + k_R \tan(\lambda\pi)\tan(\lambda\theta_c)}{\tan(\lambda\theta_c) - k_R \tan(\lambda\pi)} \\ &= \frac{509813 \times (-0.0001814)}{0.125 \times 0.57 \times (2 \times \cos 0.22)^{-0.43}} \\ &\times 0.000083^{0.57} \\ &\times \frac{1 + 1.6 \times \tan 0.57\pi \times \tan(0.57 \times 0.22)}{\tan(0.57 \times 0.22) - 1.6 \tan 0.57\pi} \\ &\approx -0.1K \end{aligned} \quad \textbf{(7-10)}$$

The temperature coefficient of surface tension for isobutanol are taken to be β = -0.0001 N/mK and μ=3.95×10^{-3} Pa·s based on the data [152] given.

Therefore, the Marangoni number *Ma* can be calculated to be:

$$\begin{aligned} Ma &= -\beta \Delta T_0 \frac{t_f}{\mu R} \\ &= 0.0001 \times (-0.1) \\ &\times \frac{6.1}{0.00395 \times 8.3 \times 10^{-5}} \approx -186 \end{aligned} \quad \textbf{(7-11)}$$

The direction of the Marangoni flow at the free liquid surface is from the centre to the contact line when only one drop is dispensed onto the substrate.

When 40 drops of isobutanol are dispensed, the sessile drop volume at the time when the dispensing is just finished can be estimated to be 378pl using equation (7-5) and the contact angle can be calculated to be 43º. The temperature difference is

calculated to be $\Delta T \approx 0.04$K using equation (7-3). Therefore, the Marangoni number Ma can be calculated to be $Ma \approx 67$. Now, the direction of the Marangoni flow at the free liquid surface is from the contact line to the centre. Figure 7-1 lists the Marangoni number calculated for sessile drops versus N_d. It can be concluded from Figure 7-1 that the Marangoni number is very low compared with the strong Marangoni flows in other solvents, where the Marangoni number can be larger than 800 [161,167,171].

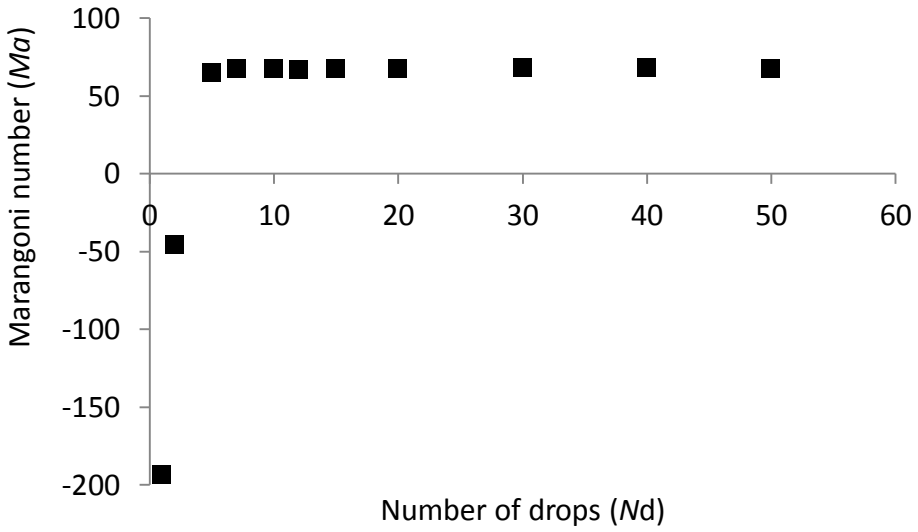

Figure 7-1 The Marangoni number for an isobutanol sessile drop versus the number of drops

As more polymer is transferred to the contact line, the influence of polymer concentration on surface tension starts to take effect as well. The surface tension is known to decrease with increasing polymer concentration [174]. With the polymer concentration becoming inhomogeneous during solvent evaporation, an increasing surface tension gradient exists from the contact line to the centre. This surface tension gradient causes a Marangoni flow from the contact line to the centre. However, this Marangoni flow is greatly weakened again when the dissolved polymer is more evenly distributed across the wetting area as the bump-like structure starts to take shape. According to the more general form of Marangoni number formula [167,174], this Marangoni number can be calculated as:

$$Ma = \frac{\Delta r L}{\mu D} \qquad \textbf{(7-12)}$$

where Δr is the surface tension difference (N/m);

L is the size of the system where Δr exists;

μ is the viscosity (Pa·s);

and D is the diffusion coefficient (m^2/s).

Due to the complex development of the concentration gradient and lack of data, it has not been possible to calculate this Marangoni number. There is no evidence to support which Marangoni effect is stronger than the other. The Marangoni effect considered here in this chapter is only due to thermal gradients rather than concentration gradients.

Based on the discussion above, it is postulated that the bump-like structure observed is the accumulative effect of Marangoni flows due to the prolonged evaporation of the isobutanol drop. The Marangoni flow in the beginning is believed to be outward towards the contact line, which facilitates the hole formation. Therefore, the bump-like feature was not observed for the structures produced by the first several drops. As the contact angle increases, the outward coffee ring flow becomes weaker and the thermal Marangoni flow reverses its direction. It is postulated that the Marangoni effect in the isobutanol drop is weak compared with Marangoni numbers larger than 800 [161,167,171]. The net flow is still outward, resulting in a depression in the centre. However, as greater numbers of isobutanol drops are dispensed into the pre-existing sessile drop, even though the Marangoni number is small (*Ma*=67), the sessile drop dispensed by 40 isobutanol droplets exists for a much longer time. For a sessile drop comprising of 40 isobutanol drops, the time from the moment it reaches its maximum contact angle until complete evaporation is approximately 55s. It is believed that the formation of the bump-like structure is the result of the prolonged Marangoni effect due to an accumulative time effect. This is in agreement with Figure 5-20 that H_d first increases and then decreases with N_d while still maintain a positive value, indicating formation of a hole. However, after 30 drops, H_d finally becomes negative, indicating a protrusion instead of a depression.

7.3 Summary

A mechanism has been proposed for the protrusion drying features in the PVP layer etched by isobutanol. The Marangoni effect caused by inhomogeneous evaporation across the drop was used to explain the bump-like structure. The Marangoni number was calculated and the results showed that the Marangoni effect in the isobutanol drop was weak. However, the drying feature is believed to be caused by the prolonged existence of the sessile drop as the number of drops dispensed increases.

8 Conclusion and Future Work Recommendation

8.1 Conclusion

This thesis investigated the factors which can affect the size of inkjet-etched via holes and the penetration limit of the polymer layer. According to the experimental results and preliminary calculations in this study, the main findings can be concluded as follows:

- Droplet ejection frequency has a significant influence on the size of the via holes created by inkjet etching. Both D_{out} and D_{in} remain independent of the number of droplets (N_d) once the polymer layer is fully penetrated at low frequencies (≤5Hz). At medium frequencies (10Hz and 20Hz), both D_{out} and D_{in} increase with N_d, and secondary holes can be formed within the primary via holes. At high frequencies (50Hz), both D_{out} and D_{in} increase with N_d much more quickly than at medium frequencies, and no secondary hole is visible. The evolution of D_{out} and D_{in} in the etching process is attributed to the interrelationship between the volume of the sessile drop and the extent of its evaporation before the next drop merges in.

- A threshold droplet frequency, f_c, has been shown to exist below which D_{out} and D_{in} are independent of N_d once N_d is sufficient for the polymer layer to be completely etched. f_c has been experimentally found to be 15Hz for a 19pl (33µm) ethanol droplet when ink-jetted onto a 0.77µm thick PVP layer.

- Droplet diameter influences both D_{out} and D_{in}, while the thickness of the polymer has an effect on D_{in} but not D_{out}. The effect of the etching solvent used and substrate temperature have also been observed. For isobutanol, D_{out} was found to be independent of N_d at 1Hz, while D_{in} varied. For ethylene glycol, both D_{out} and D_{in} increased with N_d at 1Hz. At higher temperatures than the ambient condition, the increase of diameter with N_d was less, while the size of the via holes also decreased due to the fact that faster evaporation leads to less time for the sessile drop to wet the PVP surface. It has been shown that it is possible to produce via holes with a higher aspect ratio at elevated temperatures.

- Both polymer thickness and D_{out} can influence the penetration of the polymer layer. It has been shown that D_{in} decreases linearly with D_{out}, and D_{in} will eventually reduce to a point for a given polymer thickness. D_{in} decreases as the polymer thickness increases, but in a nonlinear relationship, and approaches zero as the polymer thickness further increases. The influence of both D_{out} and polymer thickness is attributed to the interrelationship between the volume of the via hole produced and the dissolved polymer in the etching process which needs to be redistributed. A mechanism of diffusion was proposed to explain the penetration limit.

- Protrusion drying features were observed under certain conditions when using isobutanol for etching the PVP layer. The Marangoni number was calculated and the Marangoni effect was proposed as a mechanism to explain these patterns.

8.2 Recommended Future Work

Based upon the findings from this thesis, some recommendations for future work can be made as follows:

- An advanced model is needed for the process of the via hole etching by inkjet, which can also provide a mathematical solution to the penetration

limit for a solvent droplet of a specific volume dissolving a polymer layer of a certain thickness. This can be used for penetration limit estimation for a wide range of polymer thicknesses and solvent types, which can eventually give an estimation of the maximum aspect ratio that can be achieved for its evaluation as a via hole etching technique. This model could also help simulate the Marangoni effect accompanying the coffee ring process and validate the explanation for the bump-like structure when isobutanol is used as the etching solvent. This could help with choosing solvents when etching via holes to avoid the strong Marangoni effect associated with solvents. The main challenge would be linking together the different individual processes, including drop spreading, polymer dissolution and solvent evaporation, and merging into a more complex model taking into consideration all relevant factors such as viscosity, impact velocity, vapour pressure, etc., based on the separate research which has been done in each process.

- The experiments could be extended by using a wider range of polymer/solvent systems with similar characteristics, so that further research results and evidence may be obtained to verify the proposed elaboration of the fundamental aspects in making inkjet via holes. An inkjet printing system with higher resolution for the deposition of droplets of further reduced size, as well as thicker polymer layers, is required to experimentally extend the penetration curves in Figure 6-8 and Figure 6-9.

- An improved mechanism and a dynamic model are needed to explain the fluidic flow in a drop where the substrate is also dissolvable. Factors such as the polymer concentration gradient, viscosity gradient and surface tension gradient should all be considered in this model to give a more convincing explanation of how the pressures and flows within the drop combined with the surface tension force balance create the geometric features observed.

- Experiments need to be conducted to test the effect of polymer concentration gradients as well as the effect of temperature gradients on

the resulting Marangoni flow to determine the stronger Marangoni flow between these two. The surface tension gradient caused by polymer concentration gradients can be tested by pulling a wetted plate from polymer solutions of different concentrations.

- This thesis has focused on the hole making process rather than via fabrication. It is anticipated that such holes may have functional applications and most applications will require them to be filled with conductive material to function as the interconnection between layers. Conductive silver ink or polymer ink may be used to fill the produced via holes together with printed tracks on both layers to make the structure for conductivity tests.

References

[1] Deegan, R. D., *Pattern Formation in Drying Drops*. Physical Review E, 2000. 61(1): pp. 475-485.

[2] Deegan, R. D., Bakajin, O., Dupont, T. F., Huber, G., Nagel, S. R. and Witten, T. A., *Capillary Flow as the Cause of Ring Stains from Dried Liquid Drops.* Nature, 1997. 389(6653): pp. 827-829.

[3] Deegan, R. D., Bakajin, O., Dupont, T. F., Huber, G., Nagel, S. R. and Witten, T. A., *Contact Line Deposits in an Evaporating Drop*. Physical Review E, 2000. 62(1): pp. 756-765.

[4] Kawase, T., Shimoda, T., Newsome, C., Sirringhaus, H. and Friend, R. H., *Inkjet Printing of Polymer Thin Film Transistors*. Thin Solid Films, 2003. 438-439: pp. 279-287.

[5] Kawase, T., Sirringhaus, H., Friend, R. H. and Shimoda, T., *Inkjet Printed Via-Hole Interconnections and Resistors for All-Polymer Transistor Circuits.* Advanced Materials, 2001. 13(21): pp. 1601-1605.

[6] Sirringhaus, H., Kawase, T., Friend, R. H., Shimoda, T., Inbasekaran, M., Wu, W. and Woo, E. P., *High-Resolution Inkjet Printing of All-Polymer Transistor Circuits*. Science, 2000. 290(5499): pp. 2123-2126.

[7] de Gans, B. J., Hoeppener, S. and Schubert, U. S., *Polymer-Relief Microstructures by Inkjet Etching*. Advanced Materials, 2006. 18(7): pp. 910-914.

[8] de Gans, B. J., Hoeppener, S. and Schubert, U. S., *Polymer Relief Microstructures by Inkjet Etching.* Journal of Materials Chemistry, 2007. 17(29): pp. 3045-3050.

[9] Grimaldi, I. A., De Girolamo Del Mauro, A., Nenna, G., Loffredo, F., Minarini, C. and Villani, F., *Inkjet Etching of Polymer Surfaces to Manufacture Microstructures for OLED Applications.* in *AIP Conference Proceedings Vth International Conference on Times of Polymers (TOP) and Composites.* 2010. Ischia, Italy.

[10] Li, G. F., Graf, K., Bonaccurso, E., Golovko, D. S., Best, A. and Butt, H. J., *Evaporation Structures of Solvent Drops Evaporating from Polymer Surfaces:*

Influence of Molar Mass. Macromolecular Chemistry and Physics, 2007. 208(19-20): pp. 2134-2144.

[11] Bonaccurso, E., Butt, H. J., Hankeln, B., Niesenhaus, B. and Graf, K., *Fabrication of Microvessels and Microlenses from Polymers by Solvent Droplets*. Applied Physics Letters, 2005. 86(12): pp. 124101-1-124101-3.

[12] Pericet-Camara, R., Best, A., Nett, S. K., Gutmann, J. S. and Bonaccurso, E., *Arrays of Microlenses with Variable Focal Lengths Fabricated by Restructuring Polymer Surfaces with an Ink-Jet Device*. Optics Express, 2007. 15(15): pp. 9877-9882.

[13] Xia, Y. J. and Friend, R. H., *Nonlithographic Patterning Through Inkjet Printing Via Holes*. Applied Physics Letters, 2007. 90(25): pp. 253513-1-253513-3.

[14] Xia, Y. J. and Friend, R. H., *Polymer Bilayer Structure Via Inkjet Printing*. Applied Physics Letters, 2006. 88(16): pp. 163508-1-163508-3.

[15] Lu, J.-P., Chen, F.-C. and Lee, Y.-Z., *Ring-Edged Bank Array Made by Inkjet Printing for Color Filters*. Journal of Display Technology, 2009. 5(5): pp. 162-165.

[16] Lennon, A. J., Ho-Baillie, A. W. Y. and Wenham, S. R., *Direct Patterned Etching of Silicon Dioxide and Silicon Nitride Dielectric Layers by Inkjet Printing*. Solar Energy Materials and Solar Cells, 2009. 93(10): pp. 1865-1874.

[17] Lennon, A. J., Utama, R. Y., Lenio, M. A. T., Ho-Baillie, A. W. Y., Kuepper, N. B. and Wenham, S. R., *Forming Openings to Semiconductor Layers of Silicon Solar Cells by Inkjet Printing*. Solar Energy Materials and Solar Cells, 2008. 92(11): pp. 1410-1415.

[18] Yang, Y. S., You, I.-K., Koo, J. B., Lee, S. S., Lim, S. C. and Youl, K. S., *Characteristics of Via-Hole Interconnections Fabricated by Using an Inkjet Printing Method*. Journal of the Korean Physical Society, 2010. 57(6): pp. 1699-1701.

[19] Yang, Y. S., Koo, J. B. and You, I.-K., *Organic Nonvolatile Memory Devices Fabricated by Using an Inkjet Printing Method*. Journal of the Korean Physical Society, 2012. 60(10): pp. 1504-1507.

[20] Orton, J. W., *Semiconductors and the Information Revolution*. 2009: Academic Press Title. 350.

[21] Samsung, *Samsung Semiconductor Foundry*. www.samsung.com.

[22] MacDiarmid, A. G., *Nobel Lecture: ''Synthetic metals'': A Novel Role for Organic Polymers*. Reviews of Modern Physics, 2001. 73(3): pp. 701-712.

[23] Shirakawa, H., *Nobel Lecture: The Discovery of Polyacetylene Film - The Dawning of an Era of Conducting Polymers*. Reviews of Modern Physics, 2001. 73(3): pp. 713-718.

[24] Heeger, A. J., *Nobel Lecture: Semiconducting and Metallic Polymers: The Fourth Generation of Polymeric Materials.* Reviews of Modern Physics, 2001. 73(3): pp. 681-700.

[25] Lahey, B., Girouard, A., Burleson, W. and Vertegaal, R., *PaperPhone: Understanding the Use of Bend Gestures in Mobile Devices with FLexible Electronic Paper Displays*. 2011.

[26] Berggren, M., Nilsson, D. and Robinson, N. D., *Organic Materials for Printed Electronics.* Nature Materials, 2007. 6(1): pp. 3-5.

[27] Thinfilm, *Thinfilm Unveils First Scalable Printed CMOS Memory*. http://www.thinfilm.no/news/press-releases/274-thinfilm-unveils-first-scalable-printed-cmos-memory, 2011.

[28] OE-A, *Organic and Printed Electronics 4th Edition*. 2011.

[29] Moore, G. E., *Cramming More Components onto Integrated Circuits Reprinted from Electronics, Volume 38, Number 8, April 19, 1965, pp.114 ff.* Solid-State Circuits Newsletter, 2006. 20(3): pp. 33-35.

[30] Moore, G. E., *Progress in Digital Integrated Electronics*, in *Electron Device Meeting*, 1975, IEEE.

[31] Tummala, R. R., *Fundamentals of Microsystems Packaging*. 2001: McGraw-Hill Professional.

[32] SemiconductorIndustryAssociation, *International Technology Roadmap for Semiconductors 2009 Edition*. 2009.

[33] Boggs, D., Baktha, A., Hawkins, J., Marr, D. T., Miller, J. A., Roussel, P., Singhal, R., Toll, B. and Venkatraman, K. S., *The Microarchitecture of the Intel Pentium 4 Processor on 90nm Technology*. Intel Technology Journal, 2004. 8(1): pp. 1-17.

[34] Gargini, P. A., *The Global Route to Future Semiconductor Technology*. IEEE Circuits and Devices Magazine, 2002. 18(2): pp. 13-17.

[35] Bai, P., Auth, C., Balakrishnan, S., Bost, M., Brain, R., Chikarmane, V., Heussner, R., Hussein, M., Hwang, J., Ingerly, D., James, R., Jeong, J., Kenyon, C., Lee, E., Lee, S.-H., Lindert, N., Liu, M., Ma, Z., Marieb, T., Murthy, A., Nagisetty, R., Natarajan, S., Neirynek, J., Ott, A., Parker, C., Sebastian, J., Shaheed, R., Sivakumar, S., Steigerwald, J., Tyagi, S., Weber, C., Woolery, B., Yeoh, A., Zhang, K. and Bohr, M., *A 65nm Logic Techology Featuring 35nm Gate Lengths, Enhanced Channel Strain, 8 Cu Interconnect Layers, Low-k ILD and 0.57µm^2 SRAM Cell*, in *IEEE International Electron Devices Meeting*, 2004: San Francisco, California, United States.

[36] Intel, *The Evolution of a Revolution*. www.intel.com.

[37] Auth, C., Buehler, M., Cappellani, A., Choi, C.-h., Ding, G., Han, W., Joshi, S., McIntre, B., Prince, M., Ranade, P., Sandford, J. and Thomas, C., *45nm High-k+Metal Gate Strain-Enhanced Transistors*. Intel Technology Journal, 2008. 12(2): pp. 77-85.

[38] Intel, *White Paper Introduction to Intel's 32nm Process Technology*. www.intel.com.

[39] Kuhn, K. J., *Moore's Law Past 32nm: Future Challenges in Device Scaling*, in *13th International Workshop on Computational Electronics*, 2009, IEEE: Beijing, China.

[40] Dennard, R. H., Gaensslen, F. H., Yu, H.-N., Rideout, V. L., Bassous, E. and Leblanc, A. R., *Design of Ion-Implanted MOSFET's with Very Small Physical Dimensions*. IEEE Journal of Solid-State Circuits, 1974. 9(5): pp. 256-268.

[41] Intel, *Presentation: Intel Announces New 22nm 3D Tri-Gate Transistors*. www.intel.com.

[42] Thompson, S., Packan, P. and Bohr, M., *MOS Scaling: Transistor Challenges for the 21st Century*. Intel Technology Journal, 1998. 2(3): pp. 1-19.

[43] Tummala, R. R., *SOP: What Is It and Why? A New Microsyste-Integration Technology Paradigm-Moore's Law for System Integration of Miniaturized Convergent Systems of the Next Decade*. IEEE Transactions on Advanced Packaging, 2004. 27(2): pp. 241-249.

[44] Zheng, L.-R., Shen, M. and Tenhunen, H., *System-on-Chip or System-on-Package: Can We Make an Accurate Decision on System Implementation in an Early Design Phase?*, in *Southwest Symposium on Mixed-Signal Design*, 2003, IEEE: Las Vegas, Nevada, United States.

[45] Shen, M., Zheng, L.-R. and Tenhunen, H., *Cost and Performance Analysis for Mixed-Signal System Implementation: System-on-Chip or System-on-Package?* IEEE Transactions on Electronics Packaging Manufacturing, 2002. 25(4): pp. 262-272.

[46] Tummala, R. R., Swaminathan, M., Tentzeris, M. M., Laskar, J., Chang, G.-K., Sitaraman, S., Keezer, D., Guidotti, D., Huang, Z., Kyutae, L., Wan, L., Bhattacharya, S. K., Sundaram, V., Liu, F. and Raj, P. M., *The SOP for Miniaturized, Mixed-Signal Computing, Communication, and Consumer Systems of the Next Decade*. IEEE Transactions on Advanced Packaging, 2004. 27(2): pp. 250-267.

[47] Tummala, R. R. and Madisetti, V. K., *System on Chip or System on Package?* IEEE Design and Test of Computers, 1999. 16(2): pp. 48-56.

[48] Tummala, R. R., *Moore's Law Meets Its Match*. IEEE Spectrum, 2006. 43(6): pp. 44-49.

[49] Lau, J. H. and Chang, C., *An Overview of Microvia Technology*. Circuit World, 2000. 26(2): pp. 22-32.

[50] Cheong, M. S., Cho, D. W. and Ehmann, K. F., *Identification and Control for Micro-Drilling Productivity Enhancement*. International Journal of Machine Tool and Manufacture, 1999. 39: pp. 1539-1561.

[51] Masuzawa, T., *State of the Art of Micromachining*. CIRP Annals - Manufacturing Technology, 2000. 49(2): pp. 473-488.

[52] Kudla, L., *Influence of Feed Motion Features on Small Holes Drilling*. Journal of Materials Processing Technology, 2001. 109(3): pp. 236-241.

[53] Pande, S. S. and Relekar, H. P., *Investigations on Reducing Burr Formation in Drilling*. International Journal of Machine Tool Design and Research, 1986. 26(3): pp. 339-348.

[54] Min, S., Dornfeld, D. A. and Nakao, Y., *Influence of Exit Surface Angle on Drilling Burr Formation*. Journal of Manufacturing Science and Engineering, 2003. 125(4): pp. 637-644.

[55] Lee, K. and Dornfeld, D. A., *Micro-Burr Formation and Minimization through Process Control*. Precision Engineering, 2005. 29(2): pp. 246-252.

[56] Ko, S.-L., Chang, J.-E. and Kaipakjian, S., *Development of Drill Geometry for Burr Minimization in Drilling*. CIRP Annals - Manufacturing Technology, 2003. 52(1): pp. 45-48.

[57] Ko, S.-L. and Lee, J.-K., *Analysis of Burr Formation in Drilling with a New-Concept Drill*. Journal of Materials Processing Technology, 2001. 113(1-3): pp. 392-398.

[58] Ko, S.-L., Chang, J.-E. and Yang, G.-E., *Burr Minimizing Scheme in Drilling*. Journal of Materials Processing Technology, 2003. 140(1-3): pp. 237-242.

[59] Okasha, M. M., Mativenga, P. T., Driver, N. and Li, L., *Sequential Laser and Mechanical Micro-Drilling of Ni Superalloy for Aerospace Application*. CIRP Annals - Manufacturing Technology, 2010. 59(1): pp. 199-202.

[60] Lau, J. H. and Lee, S. W. R., *Microvias For Low Cost, High Density Interconnects*. 2001: McGraw-Hill.

[61] Dhar, S., Saini, N. and Purohit, R., *A Review on Laser Drilling and Its Techniques*. in *International Conference on Advances in Mechanical Engineering*. 2006. Fatehgarh Sahib, Punjab, India.

[62] Zheng, H., Gan, E. and Lim, G. C., *Investigation of Laser Via Formation Technology for the Manufacturing of High Density Substrates*. Optics and Lasers in Engineering, 2001. 36(4): pp. 355-371.

[63] Yung, K. C., Mei, S. M. and Yue, T. M., *A Study of the Heat-Affected Zone in the UV YAG Laser Drilling of GFRP Materials*. Journal of Materials Processing Technology, 2001. 122(2-3): pp. 278-285.

[64] Piqué, A. and Chrisey, D. B., *Direct-Write Technologies for Rapid Prototyping Applications: Sensors, Electronics, and integrated Power Sources*. 2002, San Diego, US: Academic Press.

[65] Lewis, J. A. and Gratson, G. M., *Direct Writing in Three Dimensions*. Materials Today, 2004. 7(7-8): pp. 32-39.

[66] Robinson, C. J., Stucker, B., Lopes, A. J., Wicker, R. and Palmer, J. A., *Integration of Direct-Write (DW) and Ultrasonic Consolidation (UC) Technologies to Create Advanced Structures with Embedded Electrical Circuitry*, in *17th Solid Freeform Fabrication Symposium*, 2006: Austin, TX, United States.

[67] Chrisey, D. B., *The Power of Direct Writing*. Science, 2000. 289(5481): pp. 879-881.

[68] Gamerith, S., Klug, A., Scheiber, H., Scherf, U., Moderegger, E. and List, E., *Direct Ink-Jet Printing of Ag–Cu Nanoparticle and Ag-Precursor Based Electrodes for OFET Applications*. Advanced Functional Materials, 2007. 17(16): pp. 3111-3118.

[69] Jeong, S., Woo, K., Kim, D., Lim, S., Kim, J. S., Shin, H., Xia, Y. and Moon, J., *Controlling the Thickness of the Surface Oxide Layer on Cu Nanoparticles for the Fabrication of Conductive Structures by Ink-Jet Printing*. Advanced Functional Materials, 2008. 18(5): pp. 679-686.

[70] Williams, E. D., Ayres, R. U. and Heller, M., *The 1.7 Kilogram Microchip: Energy and Material Use in the Production of Semiconductor Devices*. Environmental Science and Technology, 2002. 36(24): pp. 5504-5510.

[71] Mantysalo, M., Mansikkamaki, P., Miettinen, J., Kaija, K., Pienimaa, S., Ronkka, R., Hashizume, K., Kamigori, A., Matsuba, Y., Oyama, K., Terada, N., Saito, H., Kuchiki, M. and Tsubouchi, M., *Evaluation of Inkjet Technology for Electronic Packaging and System Integration*, in *57th Electronic Components and Technology Conference*, 2007: Denver, CO, United States.

[72] Guillot, P., Colin, A. and Ajdari, A., *Stability of a Jet in Confined Pressure-Driven Biphasic Flows at Low Reynolds Number in Various Geometries*. Physical Review E, 2008. 78(1): pp. 016307-1-016307-13.

[73] Wallace, D., Hayes, D., Chen, T., Shah, V., Radulescu, D., Cooley, P., Wachtler, K. and Nallani, A., *Ink-Jet as a MEMS Manufacturing Tool*, in *1st International Conference on Integration and Commercilaization of Micro and Nanosystems*, 2007: Sanya, Hainan, China.

[74] King, B. H., O'Reilly, M. J. and Barnes, S. M., *Characterzing aerosol Jet Multi-Nozzle Process Parameters for Non-Contact Front Side Metallization of Silicon Solar Cells*, in *34th Photovoltaic Specialists Conference*, 2009: Philadelphia, PA, United States.

[75] King, B. and Renn, M., *Aerosol Jet Direct Write Printing for Mil-Aero Electronic Applications*. www.optomec.com.

[76] MicroPenTechnologies. *www.micropen.com*.

[77] Cao, Y., Zhou, L., Wang, X., Li, X. and Zeng, X., *MicroPen Direct-Write Deposition of Polyimide*. Microelectronic Engineering, 2009. 86(10): pp. 1989-1993.

[78] Li, B., Clark, P. A. and Church, K. H., *Robust Direct-Write Dispensing Tool and Solutions for Micro/Meso-Scale Manufacturing and Packaging*, in *International Manufacturing Science and Engineering Conference*, 2007: Atlanta, GA, United States.

[79] nScrypt. *www.nscryptinc.com*.

[80] Piner, R. D., Zhu, J., Xu, F., Hong, S. and Mirkin, C. A., *"Dip-Pen" Nanolithography*. Science, 1999. 283(29): pp. 661-663.

[81] Nanoink. *http://www.nanoink.net/*.

[82] Jang, J., Hong, S., Schatz, G. C. and Ratner, M. A., *Self-Assembly of Ink Molecules in Dip-Pen Nanolithography: A Diffusion Model*. Journal of Chemical Physics, 2001. 115(6): pp. 2721-2729.

[83] Salaita, K., Wang, Y. and Mirkin, C. A., *Applications of Dip-Pen Nanolithography*. Nature Nanotechnology, 2007. (2): pp. 145-155.

[84] Nelson, B. A., King, W. P., Laracuente, A. R., Sheehan, P. E. and Whitman, L. J., *Direct Deposition of Continuous Metal Nanostructures by Thermal Dip-Pen Nanolithography*. Applied Physics Letters, 2006. 88(3): pp. 033104-1-033104-3.

[85] Sheehan, P. E., King, W. P., Laracuente, A. R., Yang, M. and Whitman, L. J., *Thermal Dip Pen Nanolithography*. NRL Review Chemical/Biochemical Research, 2006. pp. 1-2.

[86] Chung, S., Felts, J. R., Wang, D., King, W. P. and De Yoreo, J. J., *Temperature-Dependence of Ink Transport during Thermal Dip-Pen Nanolithography*. Applied Physics Letters, 2011. 99: pp. 193101-1-193101-3.

[87] Moldovan, N., Kim, K.-H. and Espinosa, H. D., *A Multi-Ink Linear Array of Nanofountain Probes*. Journal of Micromechanics and Microengineering, 2006. 16(10): pp. 1935-1942.

[88] Li, Y., Maynor, B. W. and Liu, J., *Electrochemical AFM "Dip-Pen" Nanolithography*. Journal of the American Chemical Society, 2001. 123(9): pp. 2105-2106.

[89] Zheng, Z., Daniel, W. L., Giam, L. R., Huo, F., Senesi, A. J., Zhang, G. and Mirkin, C. A., *Multiplexed Protein Arrays Enabled by Polymer Pen Lithography: Addressing the Inking Challenge*. Angewandte Chemie, 2009. 121(41): pp. 7762-7765.

[90] Huo, F., Zhen, Z., Zheng, G., Gian, L. R., Zhang, H. and Mirkin, C. A., *Polymer Pen Lithography*. Science, 2008. 321: pp. 1658-1660.

[91] Bondi, S. N., Lackey, W. J., Johnson, R. W., Wang, X. and wANG, Z. L., *Laser Assisted Chemical Vapor Deposition Synthesis of Carbon Nanotubes and Their Characterization* Carbon, 2006. 44: pp. 1393-1403.

[92] Foulon, F. and Stuke, M., *Argon-Ion Laser Direct-Write Al Deposition from Trialkylamine Alane Precursors*. Applied Physics A: Materials Science and Processing, 1993. 56(3): pp. 283-289.

[93] Wanke, M. C., Lehmann, O., Müller, k., Wen, Q. and Stuke, M., *Laser Rapid Prototyping of Phetonic Band-Gap Microsctructures*. Science, 1997. 275(5304): pp. 1284-1286.

[94] Williams, K., Maxwell, J., Larsson, K. and Boman, M., *Freeform Fabrication of Functional Microsolenoids, Electromagnets and Helical Springs Using High-Pressure Laser Chemical Vapor Deposition*, in *12th IEEE International Conference on Micro Electro Mechanical Systems*, 1999: Orlando, Florida, United States.

[95] von Gutfeld, R. J., Acosta, R. E. and Romankiw, L. T., *Laser Enhanced Plating and Etching: Mechanisms and Applications*. IBM Journal of Research and Development, 1982. 26(2): pp. 136-144.

[96] Hon, K. K. B., Li, L. and Hutchings, I. M., *Direct Writing Technology - Advances and Developments*. CIRP Annals - Manufacturing Technology, 2008. 57(2): pp. 601-620.

[97] von Gutfeld, R. J., Tynan, E. E., Melcher, R. L. and Blum, S. E., *Laser Enhanced Electroplating and Maskless Pattern Generation*. Applied Physics Letters, 1979. 35(9): pp. 651-653.

[98] Chen, Q. J., K., I. and Allen, S. D., *Laser Enhanced Electroless Plating of Micro-Scale Copper Wires*. Journal of Electrochemical Society, 2000. 147(4): pp. 1418-1422.

[99] Li, L. and Wee, L. M., *Multiple-Layer Laser Direct Writing Metal Deposition in Electrolyte Solution.* Applied Surface Science, 2005. 247(1-4): pp. 285-293.

[100] Bohandy, J., Kim, B. F. and Adrian, F. J., *Metal Deposition from a Supported Metal Deposition from a Supported Metal Film Using an Excimer*. Journal of Applied Physics, 1986. 60: pp. 1538-1539.

[101] Claeyssens, F., Klini, A., Mourka, A. and Fotakis, C., *Laser Patterning of Zn for ZnO Nanostructure growth: Comparison between Laser Induced Forward Transfer in Air and In Vacuum''*. Thin Solid Films, 2007. 515(24): pp. 8529-8533.

[102] Piqué, A., Chrisey, D. B., Auyeung, R. C. Y., Fitz-Gerald, J., Wu, H. D., McGill, R. A., Lakeou, S., Wu, P. K., Nguyen, V. and Duignan, M., *A Novel Laser Transfer Process for Direct Writing of Electronic and Sensor Materials*. Applied Physics A: Materials Science and Processing, 1999. 69(7): pp. S279-S284.

[103] Piqué, A., Weir, D. W., Wu, P. K., Pratap, B., Arnold, C. B., Ringeisen, B. R., McGill, R. A., Auyeung, R. C. Y., Kant, R. A. and Chrisey, D. B., *Direct-Write of Sensor Devices by a Laser Forward Transfer Technique*. in *SPIE LASE*. 2002. San Jose, California, Unisted States.

[104] Machalett, F., Edinger, K., Ye, L., Melngailis, J., Venkatesan, T., Diegel, M. and Steenbeck, K., *Focused-Ion-Beam Writing of Electrical Connections into Platinum Oxide Films*. Applied Physics Letters, 2000. 76(23): pp. 3445-3447.

[105] Reyntjens, S. and Puers, R., *Focused Ion Beam Induced Deposition: Fabrication of Three-Dimensional Microstructures and Young's Modulus of the Deposited Material*. Journal of Micromechanics and Microengineering, 2000. 10(2): pp. 181-188.

[106] Li, W. and Warburton, P. A., *Low-Current Focused-Ion-Beam Induced Deposition of Three-Dimensional Tungsten Nanoscale Conductors*. Nanotechnology, 2007. 18(48): pp. 1-5.

[107] Tao, T., Ro, J., Melngailis, J., Xue, Z. and Kaesz, H. D., *Focused Ion Beam Induced Deposition of Platinum*. Journal of Vacuum Science and Technology B: Microelectronics and Nanometer Structures, 1990. 8(6): pp. 1826-1829.

[108] Tao, T., Wilkinson, W. and Melngailis, J., *Focused Ion Beam Induced Deposition of Platinum for Repair Processes*. Journal of Vacuum Science and Technology B: Microelectronics and Nanometer Structures, 1991. 9(1): pp. 162-164.

[109] Della Ratta, A. D., John, M. and Thompson, C. V., *Focused-Ion Beam Induced Deposition of Copper*. Journal of Vacuum Science and Technology B: Microelectronics and Nanometer Structures, 1993. 11(6): pp. 2195-2200.

[110] Harriott, L. R. and Vasile, M. J., *Focused Ion Beam Induced Deposition of Opaque Carbon Films*. Journal of Vacuum Science and Technology B: Microelectronics and Nanometer Structures, 1998. 6(3): pp. 1035-1038.

[111] Shedd, G. M., Lezec, H., Dubner, A. D. and Melngailis, J., *Focused Ion Beam Induced Deposition of Gold*. Applied Physics Letters, 1986. 49(23): pp. 1584-1586.

[112] Gross, M. E., Harriott, L. R. and Opila, R. L., *Focused Ion Beam Stimulated Deposition of Aluminum from Trialkylamine Alanes*. Journal of Applied Physics, 1990. 68(9): pp. 4820.

[113] Bhatia, T., Ozturk, A., Xie, L., Jordan, E. H., Cetegen, B. M., Gell, M., Ma, X. and Padture, N. P., *Mechanisms of Ceramic Coating Deposition in Solution-Precursor Plasma Spray*. Journal of Materials Research, 2002. 17(9): pp. 2363-2372.

[114] Chen, Q., Tong, T., Longtin, J. P., Tankiewicz, S., Sampath, S. and Gambino, R. J., *Novel Sensor Fabrication Using Direct-Write Thermal Spray and Precision Laser Micromachining*. Journal of Manufacturing Science and Engineering, 2004. 126(4): pp. 830-836.

[115] Herman, H., Sampath, S. and McCune, R., *Thermal Spray Current Status and Future Trends*. Materials Research Society Bulletin, 2000. 25(7): pp. 17-25.

[116] Longtin, J., Sampath, S., Tankiewicz, S., Gambino, R. J. and Greenlaw, R. J., *Sensors for Harsh Environments by Direct-Write Thermal Spray*. IEEE Sensors Journal, 2004. 4(1): pp. 118-121.

[117] Microfab, *Image Analysis Routines for Alignment Inspection and Drop Analysis*. www.microfab.com.

[118] Martin, G. D., Hoath, S. D. and Hutchings, I. M., *Inkjet Printing - The Physics of Manipulating Liquid Jets and Drops*. Journal of Physics: Conference Series, 2008. 105: pp. 012001-1-012001-14.

[119] Fromm, J. E., *Numerical Calculation of the Fluid Dynamics of Drop-on-Demand Jets*. IBM Journal of Research and Development, 1984. 28(3): pp. 322-333.

[120] Reis, N. and Derby, B., *Ink Jet Deposition of Ceramic Suspensions: Modelling and Experiments of Droplet Formation*. MRS Proceedings, 2000. 625: pp. 117-122.

[121] Jang, D., Kim, D. and Moon, J., *Influence of Fluid Physical Properties on Ink-Jet Printability*. Langmuir, 2009. 25(5): pp. 2629-2635.

[122] Derby, B., *Inkjet Printing of Functional and Structural Materials: Fluid Property Requirements, Feature Stability, and Resolution*. Annual Review of Materials Research, 2010. 40: pp. 395-414.

[123] Reis, N., Ainsley, C. and Derby, B., *Ink-Jet Delivery of Particle Suspensions by Piezoelectric Droplet Ejectors*. Journal of Applied Physics, 2005. 97: pp. 094903-1-094903-6.

[124] Dong, H. M., Carr, W. W. and Morris, J. F., *An Experimental Study of Drop-on-Demand Drop Formation*. Physics of Fluids, 2006. 18(7): pp. 072102-1-072012-16.

[125] de Gans, B. J., Kazancioglui, E., Meyer, W. and Schubert, U., *Ink-Jet Printing Polymers and Polymer Libraries Using Micropipettes*. Macromolecular Rapid Communications, 2004. 25(1): pp. 292-296.

[126] Gan, H. Y., Shan, X., Eriksson, T., Lok, B. K. and Lam, Y. C., *Reduction of Droplet Volume by Controlling Actuating Waveforms in Inkjet Printing for Micro-Pattern Formation*. Journal of Micromechanics and Microengineering, 2009. 19(5): pp. 055050-1-055050-8.

[127] Sakai, S., *Dynamics of Piezoelectric Inkjet Printing Systems*, in *NIP16: International Conference on Digital Printing Technologies*, 2000: Vancouver, B.C., Canada.

[128] Dong, H., Carr, W. W. and Morris, J. F., *Visualization of Drop-on-Demand Inkjet: Drop Formation and Deposition*. Review of Scientific Instruments, 2006. 77(8): pp. 085101-1-085101-8.

[129] Duineveld, P. C., de Kok, M. M., Buechel, M., Sempel, A. H., Mutsaers, K. A. H., van de Weijer, P., Camps, I. G. J., Van de Biggelaar, T. J. M., Rubingh, J.-E. J. M. and Haskal, E. I., *Ink-jet Printing of Polymer Light-Emitting Devices.* Proceedings of SPIE: Organic Light-Emitting Materials and Devices V, 2002. 4464: pp. 59-67.

[130] Zwillinger, D., *CRC Standard Mathematical Tables and Formulae*. 2002. 928.

[131] Starov, V. and Sefiane, K., *On Evaporation Rate and Interfacial Temperature of Volatile Sessile Drops.* Colloids and Surfaces A: Physicochemical and Engineering Aspects, 2009. 333(1-3): pp. 170-174.

[132] Semenov, S., Starov, V. M., Velarde, M. G. and Rubio, R. G., *Droplets Evaporation: Problems and Solutions*. The European Physical Journal Special Topics, 2011. 197: pp. 265-278.

[133] Yarin, A. L., *Drop Impact Dynamics: Splashing, Spreading, Receding, Bouncing ...* Annual Review of Fluid Mechanics, 2006. 38: pp. 159-192.

[134] Schiaffino, S. and Sonin, A. A., *Molten Droplet Deposition and Solidification at Low Weber Numbers.* Physics of Fluids, 1997. 9(11): pp. 3172-3187.

[135] Mundo, C., Sommerfeld, M. and Tropea, C., *Droplet-Wall Collisions: Experimental Studies of the Deformation and Breakup Process*. International Journal of Multiphase Flow, 1995. 21(2): pp. 151-173.

[136] Rioboo, R., Tropea, C. and Marengo, M., *Outcomes from a Drop Impact on Solid Surfaces.* Atomization and Sprays, 2001. 11(2): pp. 155-165.

[137] Rioboo, R., Marengo, M. and Tropea, C., *Time Evolution of Liquid Drop Impact onto Solid, Dry Surfaces*. Experiments in Fluids, 2002. 33: pp. 112-124.

[138] Fukai, J., Shiiba, Y., Yamamoto, T., Miyatake, O., Poulikakos, D., Megaridis, C. M. and Zhao, Z., *Wetting Effects on the Spreading of a Liquid Droplet Colliding with a Flat Surface: Experiment and Modeling*. Physics of Fluids, 1995. 7(2): pp. 236-247.

[139] Mao, T., Kuhn, D. C. S. and Tran, H., *Spread and Rebound of Liquid Droplets upon Impact on Flat Surfaces.* AIChE Journal, 1997. 43(9): pp. 2169-2179.

[140] Yarin, A. L. and Weiss, D. A., *Impact of Drops on Solid Surfaces: Self-Similar Capillary Waves, and Splashing as a New Type of Kinematic Discontinuity*. Journal of Fluid Mechanics, 1995. 283: pp. 141-173.

[141] Wang, A.-B. and Chen, C.-C., *Splashing Impact of A Single Drop onto Very Thin Liquid Films.* Physics of Fluids, 2000. 12(9): pp. 2155-2158.

[142] Cossali, G. E., Coghe, A. and Marengo, M., *The Impact of a Single Drop on a Wetted Solid Surface*. Experiments in Fluids, 1997. 22: pp. 463-472.

[143] Worthington, A. M. and Cole, R. S., *Impact with a Liquid Surface Studied by the Aid of Instantaneous Photography. Paper II*. Philosophical Transactions of the Royal Society of London. Series A, Containing Papers of a Mathematical or Physical Character, 1900. 194: pp. 175-199.

[144] Schönfeld, F., Graf, K., Hardt, S. and Butt, H. J., *Evaporation Dynamics of Sessile Liquid Drops in Still Air with Constant Contact Radius.* International Journal of Heat and Mass Transfer, 2008. 51(13-14): pp. 3696-3699.

[145] Reid, R. C., Prausnitz, J. M. and Poling, B. E., *The Properties of Gases and Liquids 4th Edition*. 1987: McGraw-Hill. 741.

[146] Miller-Chou, B. A. and Koenig, J. L., *A Review of Polymer Dissolution*. Progress in Polymer Science, 2003. 28(8): pp. 1223-1270.

[147] Desie, G., Allaman, S., Lievens, O., Anthonidssen, K. and Soucemarianadin, A., *Influence of Substrate Properties in Drop on Demand Printing*, in *International Conference on Digital Printing Technologies*, 2002.

[148] Hu, H. and Larson, R. G., *Evaporation of a Sessile Droplet on a Substrate*. Journal of Physical Chemistry B, 2002. 106: pp. 1334-1344.

[149] Williamson, R. E. and Threadgill, E. D., *A Simulation for the Dynamics of Evaporating Spray Droplets in Agricultural Spraying*. Transactions of the ASAE, 1974. 17: pp. 254-261.

[150] Hansen, C. M., *Hansen Solubility Parameters A User's Handbook*. 2007: CRC Press.

[151] Madec, M.-B., Morrison, J. J., Sanchez-Romaguera, V., Turner, M. L. and Yeates, S. G., *Organic Field Effect Transistors from Ambient Solution Processed Poly(Triarylamine)-Insulator Blends*. Journal of Materials Chemistry, 2009. 19: pp. 6750-6755.

[152] Petrochemicals, *Isobutanol Technical Leaflet*. 2006.

[153] Gatne, K. P., Jog, M. A. and Manglik, R. M., *Surfactant-Induced Modification of Low Weber Number Droplet Impact Dynamics*. Langmuir, 2009. 25(14): pp. 8122-8130.

[154] Gande, S. K., *Characeterization of Low Weber Number post-Impact Drop-Spread Dynamics by a Damped Harmonic System Model*, in *Department of Mechanical Engineering*, 2011, University of Cincinnati.

[155] Lee, J. B. and Lee, S. H., *Dynamic Wetting and Spreading Characteristics of a Liquid Droplet Impinging on Hydrophotic Textured Surfaces*. Langmuir, 2011. 27(11): pp. 6565-6573.

[156] Pasandideh-Fard, M., Qiao, Y. M., Chandra, S. and Mostaghimi, J., *Capillary Effects During Droplet Impact on a Solid Surface*. Physics of Fluids, 1996. 8(3): pp. 650-659.

[157] Carey, V. P., *Liquid-Vapor Phase-Change Phenomena*. Chemical and Mechanical Engineering, Hewitt, G. F. and Tien, C. L. 1992. 645.

[158] Pericet-Camara, R., Bonaccurso, E. and Graf, K., *Microstructuring of Polystyrene Surfaces with Nonsolvent Sessile Droplets*. ChemPhysChem, 2008. 9(12): pp. 1738-1746.

[159] White, L. R., *The Contact Angle on an Elastic Substrate. I. The Role of Disjoining Pressure in the Surface Mechanics*. Journal of Colloid and Interface Science, 2003. 258: pp. 82-96.

[160] Hu, H. and Larson, R. G., *Analysis of the Microfluid Flow in an Evaporating Sessile Droplet*. Langmuir, 2005. 21: pp. 3963-3971.

[161] Hu, H. and Larson, R. G., *Marangoni Effect Reverses Coffee-Ring Depositions*. Journal of Physical Chemistry B, 2006. 110(14): pp. 7090-7094.

[162] Grimaldi, I. A., de Girolamo Del Mauro, A., Loffredo, F., Nenna, G., Villani, F. and Minarini, C., *Microlens Array Manufactured by Inkjet Printing: Study of the Effects of the Solvent and the Polymer Concentration on the Microstructure Shape*. in *Optical Measurement Systems for Industrial Inspecion VII*. 2011. Munich, Germany: SPIE Digital Library.

[163] Grimaldi, I. A., De Girolamo Del Mauro, A., Nenna, G., Loffredo, F., Minarini, C. and Villani, F., *Inkjet Etching of Polymer Surfaces to Manufacture Microstructures for OLED Applications*. in *5th International Conference on Times of Polymers and Composites*. 2010. Ischia, Italy.

[164] Karabasheva, S., Baluschev, S. and Graf, K., *Microstructures on Soluble Polymer Surfaces via Drop Deposition of Solvent Mixtures*. Applied Physics Letters, 2006. 89(3): pp. 031110-1-031110-3.

[165] Lim, J. A., Lee, W. H., Lee, H. S., Lee, J. H., Park, Y. D. and Kilwon, C., *Self-Organization of Ink-Jet-Printed Triisopropylsilylethynyl Pentacene via Evaporation-Induced Flows in a Drying Droplet*. Advanced Functional Materials, 2008. 18(2): pp. 229-234.

[166] Singh, M., Haverinen, H. M., Dhagat, P. and Jabbour, G. E., *Inkjet Printing - Process and Its Applications*. Advanced Materials, 2010. 22(6): pp. 673-685.

[167] Zhang, Y., Yang, S., Chen, L. and Evans, J. R. G., *Shape Changes during the Drying of Droplets of Suspensions*. Langmuir, 2008. 24: pp. 3752-3758.

[168] Park, J. and Moon, J., *Control of Colloidal Particle Deposit Patterns within Picoliter Droplets Ejected by Ink-Jet Printing*. Langmuir, 2006. 22: pp. 3506-3513.

[169] Jun, F., Hirotaka, I., Yosuke, S., Masayuki, K., Masamichi, M. and Atsushi, T., *Effects of Droplet Size and Solute Concentration on Drying Process of Polymer Solution Droplets Deposited on Homogeneous Surfaces*. International Journal of Heat and Mass Transfer, 2006. 49: pp. 3561-3567.

[170] Ristenpart, W. D., Kim, P. G., Domingues, C., Wan, J. and Stone, H. A., *Influence of Substrate Conductivity on Circulation Reversal in Evaporating Drops*. Physical Review Letters, 2007. 99(23): pp. 234502-1-234502-4.

[171] Hu, H. and Larson, R. G., *Analysis of the Effects of Marangoni Stresses on the Microflow in an Evaporating Sessile Droplet*. Langmuir, 2005. 21: pp. 3972-3980.

[172] Perry, R. H. and Green, D. W., *Perry's Chemical Engineers' Handbook Seventh Edition*. Perry, R. H., Green, D. W. and Maloney, J. O. 1997: McGraw-Hill.

[173] Mark, J. E., *Physical Properties of Polymers Handbook*. 2007. 1096.

[174] Kajiya, T., Monteux, C., Narita, T., Lequeux, F. and Doi, M., *Contact-Line Recession Leaving a Macroscopic Polymer Film in the Drying Droplets of Water-Poly(N,N-Dimethylacrylamide) (PDMA) Solution*. Langmuir, 2009. 25(12): pp. 6934-6939.